A Preliminary Field Study to Examine the Potential of Hydrogeophysical Methods to Monitor Soil Moisture Dynamics in Quaternary Outwash Materials

by

Alicia Lynn Kimberley

A thesis
presented to the University of Waterloo
in fulfillment to the
thesis requirement for the degree of
Master of Science
in
Earth Sciences

Waterloo, Ontario, Canada, 2015

Author's Declaration

I hereby declare that I am the sole author of this thesis. I authorize the University of Waterloo to make this thesis available to other institutions and students for the use of scholarly research. I also understand that this thesis may be made available electronically for the public.

Alicia L. Kimberley

Abstract

This thesis examines the capacity of a suite of near-surface geophysical techniques (i.e., ground-penetrating radar (GPR), electromagnetic induction (EMI) and electrical resistivity tomography (ERT)) to monitor soil moisture dynamics over a complete annual cycle at the Arkell Research Station (ARS). The ARS is located at the terminal edge of the Paris moraine within the outwash plain and consists of highly heterogeneous coarse grained deposits. The characterization of the soil moisture conditions at this site would represent an important component in furthering our understanding of the capabilities of geophysical methods in coarse grained materials.

Soil water contents can be monitored through measurements of dielectric permittivity from GPR surveys and electrical conductivity from EMI and ERT surveys. The geophysical measurements made during this study qualitatively agree with the soil moisture conditions determined through gravimetric sampling and inferred from weather data. However, the quantitative correlation between the geophysical and gravimetric data was found to be low. Hence, while it is apparent from this work that the responses of these geophysical methods are sensitive to soil moisture conditions in coarse grained soils, more work is required to extract quantitative soil moisture information from geophysical data for these soils.

Acknowledgements

I would like to first give special thanks to my committee supervisor Dr. Tony Endres, Dr. Jon Paul Jones, Dr. Pete Pehme and Dr. Colby Steelman for their guidance, support and assistance throughout my project. Their help through this project has been much appreciated. I would also like to thank Cameron Toy and Phil Van-Lane for their support and assistance with my project both in the field and in the lab. I would also like to give many thanks to Drs. Beth Parker and Tony Endres for funding this project, and the University of Guelph, especially Pete Milton, for allowing me to conduct my research at the Arkell Research Station.

Table of Contents

List of Figures

List of Tables

List of Appendices

Appendix A

Appendix B

Appendix C

Appendix D

The material contained on this CD includes all field data (original and processed) and is available from the Department of Earth and Environmental Sciences, upon request.

- Raw GPR CMP and Reflection data
- Raw and corrected EM38 and EM31 data
- Raw ERT data
- Grain size distribution data
- Elevation data
- Water levels
- Gravimetric water contents data
- Weather data
- Site photos

1.0 Introduction

Soil moisture plays an important role in many hydrogeological processes and problems (e.g., contaminant transport and infiltration, groundwater recharge and precision agriculture), which is why the characterization of subsurface hydraulic properties is important for understanding how water and contaminants move through the system. Advancing our conceptual understanding of the hydrogeological system through such characterizations will undoubtedly improve current groundwater management strategies. Water resources are of great importance especially with an ever-increasing demand on fresh water resources. The vadose zone plays an important role in the protection of our water stores by providing a buffer zone between the surface and the groundwater, as well as regulating the water availability for crops and drinking water.

Glacial outwash deposits act as large water reservoirs, but these quaternary deposits exhibit significant variability in terms of their permeability (Johnson and Gillam, 1995). In Guelph, recharge to the underlying bedrock aquifer occurs through diffusive movement of water through the glacial overburden material (Cole et al., 2009). The heterogeneous nature of the glacial material causes a non-uniform distribution of permeability and recharge. Understanding the role soil moisture dynamics in the Paris moraine system is important for the preservation of these large underlying aquifers. The outwash channel deposits of the Paris moraine are extremely heterogeneous and contain stony coarse grained soils.

Traditional hydrogeological methods have been employed to measure soil moisture, such as time-domain reflectometry (TDR), neutron probes and gravimetric samples; however, these methods yield localized information that are biased to the measurement point. These methods can provide less accurate results since they disturb the soil. For instance, Coppolla et al. (2013)

showed how difficult it can be to accurately estimate soil moisture with traditional methods such as TDR probes and gravimetric sampling techniques in stony coarse grained materials. The sampling difficulties result from practical issues related to inserting probes into the subsurface without disturbing the soil structure and the high degree of sampling that is required in order to capture the immense spatial heterogeneity.

The use of multiple, non-invasive geophysical techniques (e.g., ground penetrating radar (GPR), electrical resistivity tomography (ERT) and electromagnetic induction (EMI)) have the capacity to provide extensive spatial and temporal information about soil moisture in the near surface. Additionally, near-surface geophysical methods provide information about the subsurface structure of aquifers and potential permeable pathways (Celano et al., 2011; McArthur et al., 2011; Revil et al., 2012). McArthur et al. (2011) performed GPR and borehole geophysics studies to resolve the heterogeneity seen in a glacial outwash aquifer and showed that GPR could provide information about the complex subsurface heterogeneity including potential permeable pathways that correlated quite well with the borehole geophysics.

Two and three dimensional models of subsurface geophysical properties (e.g., dielectric permittivity, electrical conductivity) can be created in a non-invasive and efficient manner using GPR, EMI or ERT which can be used to estimate physical properties such as soil moisture (Luck et al., 2011; Pellicer et al., 2012; Smiarowski et al., 2011; Steelman and Endres, 2010). Steelman and Endres (2010) used the velocity estimates from common-midpoint (CMP) and direct ground wave (DGW) surveys to estimate soil moisture in the subsurface throughout the year.

Although many geophysical studies have been conducted in order to characterize the hydrogeological systems within homogeneous fine grained deposits (Luck et al., 2011; Mouhri et al., 2013; Pellicer et al., 2012; Smiarowski et al., 2011; Steelman, 2010; Steelman and Endres,

2012), few have been carried out in heterogeneous stony coarse grained deposits. The aim of this thesis is to examine the potential of GPR, EMI and ERT to provide information about the soil moisture dynamics in stony coarse grained soils such as those seen in the outwash deposits at the Arkell Research Station (ARS). To investigate the potential of these three hydrogeophysical methods, the nature of the observed variations in the measured responses both spatially and temporally will be assessed. Additionally, the correlation between hydrogeophysical responses and the available hydrological data (i.e. gravimetric sampling, weather data and water level measurements) will be examined. The non-invasive nature and larger sampling volume of the hydrogeophysical methods (GPR, EMI and ERT) allow for more accurate characterization of hydrogeological systems in a stony coarse grained deposit compared to traditional hydrogeological methods (i.e. TDR probes and gravimetric sampling). The results from this research illustrate that these three hydrogeophysical methods have the potential to monitor soil moisture conditions in a heterogeneous coarse grained material.

2.0 Background on Geoelectrical Methods

Geoelectrical methods can be divided into two broad categories: 1) galvanic methods (e.g. ERT) which require direct contact via electrodes to inject an electrical current into the Earth; and 2) electromagnetic methods (e.g. GPR and EMI) which involve the propagation of an electromagnetic (EM) field into the subsurface through transmitter and receiver coils that may not be in direct contact with the Earth. The time-varying EM fields are governed by Maxwell's equation:

$$\nabla^2 B = \mu\sigma\frac{\partial B}{\partial t} + \mu\varepsilon\frac{\partial^2 B}{\partial t^2} \; and \; \nabla^2 E = \mu\sigma\frac{\delta E}{\delta t} + \mu\varepsilon\frac{\delta^2 E}{\delta t^2} \quad [1]$$

where B is the magnetic flux density and E is the electric field intensity. The EM wave propagation is dependent on the Earth's electrical properties: dielectric permittivity (ε), magnetic permeability (μ) and electric conductivity (σ).

The EM methods can be further divided with respect to whether the conduction or displacement currents are dominate where the $\frac{\partial}{\partial t}$ term is related to conduction currents and the $\frac{\partial^2}{\partial t^2}$ corresponds to the displacement currents. The displacement current term usually dominates at frequencies above 10 MHz where wave propagation occurs. These are the conditions necessary for the use of GPR. Conversely, conduction currents dominate at frequencies below 10 MHz where diffusive behavior occurs. The applications of EMI techniques require these conditions.

2.1 Ground Penetrating Radar

GPR uses high-frequency (1-1000 MHz) EM waves to probe the subsurface. An extensive coverage of the theories and applications of GPR can be found in Annan (2005). In

general, this method involves the propagation of EM waves between a transmitter and a receiver along a variety of possible ray paths (Figure 2.1); the reflected and direct groundwave ray paths are the focus of this thesis. In a low loss, non-magnetic geological material, the velocity of the propagating EM wave can be determined using:

$$v = \frac{c}{\sqrt{\kappa}}, \quad [2]$$

where κ is the relative dielectric permittivity (i.e., $\kappa = \varepsilon / \varepsilon_0$ where ε_0 is the permittivity of a vacuum) and c is the velocity of light in free space (0.29979 m/ns). Therefore, the velocity of the EM wave is essentially a function of the relative permittivity in most cases.

2.1.1 Determining Soil Water Content from Dielectric Permittivity

Dielectric permittivity is a measure of the electric charge polarization in response to an applied electrical field. The dielectric response of a material is strongly dependent on the presence of liquid water. Different petrophysical relationships such as empirical relationships, volumetric mixing formulae and effective medium approximations, can be used to estimate volumetric water content (θ) from κ values. The choice of relationship depends on the amount of auxiliary knowledge about the soil, such as porosity, mineral type and temperature (Steelman and Endres, 2011). The method used throughout this thesis is the empirical relationship developed by Topp et al. (1980):

$$\theta = -5.3x10^{-2} + 2.92x10^{-2}\kappa - 5.5x10^{-4}\kappa^2 + 4.3x10^{-6}\kappa^3 \quad [3]$$

where κ is equal to the measured dielectric permittivity of the bulk material. This relationship is simple and does not require additional information about the porosity or the dielectric

permittivity of the various soil constituents.

2.1.2 Ground Penetrating Radar Techniques

There are two GPR surface techniques that are used throughout this thesis for measuring soil moisture content and characterizing the subsurface: reflection profiling and common-midpoint (CMP) soundings.

Reflection profiling is done by moving the transmitter (Tx) and the receiver (Rx) sequentially along the survey line with a constant separation (i.e. offset) between the antennae (Figure 2.2a). As the antenna array is moved along the survey line, they image the ground, resulting in the collection of traces that show variations in reflection traveltime. This technique can be used to map out the subsurface geology. In addition, volumetric water content can be monitored using variations in two-way traveltimes of reflections from stratigraphic interfaces. A quantitative estimate of water content using reflection profiling requires determination of the depth to the reflecting stratigraphic interface.

CMP soundings involved the incremental separation of the Tx and Rx about a central point (Figure 2.2b). Volumetric water content information can be obtained from velocity analysis of the shallow DGW and deeper reflection events. Application of NMO velocity analysis to CMP data yield information about the subsurface EM velocity structure and depth to reflecting interfaces. In addition, CMP data can be used to measure DGW velocity which yields information about the dielectric permittivity along the surface.

2.2 Electromagnetic Induction

An extensive coverage of the EMI theories and applications of ground conductivity meters (GCM) can be found in Fitterman and Labson (2005) and McNeil (1980). GCM instruments are used for mapping the electrical conductivity of the subsurface for a wide range of applications,

including monitoring soil moisture content (e.g. Akbar et al., 2005; Reedy and Scanlon, 2003; Sheets and Hendrickx, 1995). The response of a GCM device to the Earth is expressed in terms of an apparent conductivity (σ_a) which represents an identical instrument response over a homogeneous halfspace.

For an Earth with a vertically varying conductivity profile (σ_z), the apparent conductivity is given by:

$$\sigma_a = \int_0^\infty \sigma(z')\,\phi(z')dz' \qquad [4]$$

where $\phi(z')$ is the response function of the GCM device and $z' = z/s$ is the normalized depth with s being the Rx-Tx coil spacing.

The form of $\phi(z')$ depends on the coil orientation. The two orientations used in this study were the vertical (horizontal co-planar) and horizontal (vertical co-planar) dipole configurations where

$$\phi_v(z') = \frac{4z'}{[4(z')^2 + 1]^{3/2}} \qquad [5]$$

and,

$$\phi_H(z') = 2 - \frac{4z'}{[4(z')^2 + 1]^{1/2}} \qquad [6]$$

are the vertical or horizontal response function of the GCM, respectively. Figure 2.3 shows that the horizontal dipole is most sensitive to surface conditions with the sensitivity decreasing

significantly with depth. The vertical dipole is highly sensitive at a depth of 40% of the coil separation and is minimally sensitive to surface conditions.

2.3 Electrical Resistivity Tomography

ERT measures the ability of the subsurface to resist the flow of a current when it is applied to the ground. Zonge and Urquhart (2005) and Revil et al. (2012) provide a comprehensive review of the theories and applications of ERT. The resistivity measured by the ERT is dependent on the porosity, saturation and resistivity of the pore fluids as well as the soil texture. ERT can provide high-resolution images of the shallow subsurface in a wide range of field conditions; it works well in resistive and conductive environments (Amidu and Dunbar, 2007; Frohlich and Parke, 1989; Zhou et al., 2001). The IRIS Instruments Syscal Jr. 48 channel resistivity instrument was used to measure the resistivity variations in the subsurface. The instrument is designed to cycle through the 48 electrodes using 4 electrodes at a time; there are two source current electrodes (A and B) and two sink potential electrodes (M and N).

The electrical current moves radially away from the source current electrodes and then the potential difference between the sink potential electrodes can be measured to determine apparent resistivity (ρ_a):

$$\Delta V_{MN} = V_M - V_N = \frac{\rho_a I}{2\pi}\left(\frac{1}{r_{AM}} - \frac{1}{r_{BM}} - \frac{1}{r_{AN}} + \frac{1}{r_{BN}}\right) \quad [11]$$

$$\rho = \frac{\Delta V_{MN}}{I}\left[2\pi\left(\frac{1}{r_{AM}} - \frac{1}{r_{BM}} - \frac{1}{r_{AN}} + \frac{1}{r_{BN}}\right)^{-1}\right] \quad [12]$$

where ΔV_{MN} is the difference in electrical potential, ρ_a is the apparent electrical resistivity, I is

the electrical current used for injection of the current and r is the distance between electrode pairs. The separation of the electrodes and the array chosen affects the depth of penetration of the survey and the sensitivity to noise. The further the electrodes are separated the deeper penetration you will get.

The type of array used depends on the target and the location where the survey is being conducted. In this thesis, Wenner arrays are used. The Wenner array is robust in the presence of noise and is most sensitive to changes in the vertical direction, i.e., horizontal layers (Loke, 1997, 1999, 2000; Pellicer et al., 2012; Smith, 2006).

The electrical resistivity data that is collected can also be used to infer soil moisture content using Archie's law:

$$\rho = a\phi^{-m} S_w^{-n} \rho_w . \qquad [13]$$

where S_w is the water saturation which is the volume fraction of pore space containing water, n is the saturation exponent which can be assumed to be equal to 2, a is the empirical constant $0.5 \le a \le 2.5$ and ρ_w is the resistivity of the pore water.

The ERT data in this thesis was inverted using the software package (RES2DINV) which is based on a standard Gauss-Newton optimization routine. The tutorial by Loke (2011) explains the inversion process fully. There is a non-uniqueness issue with the forward modeling and inversion of the resistivity data; coupling other geophysical techniques with the ERT method can help reduce non-uniqueness issues.

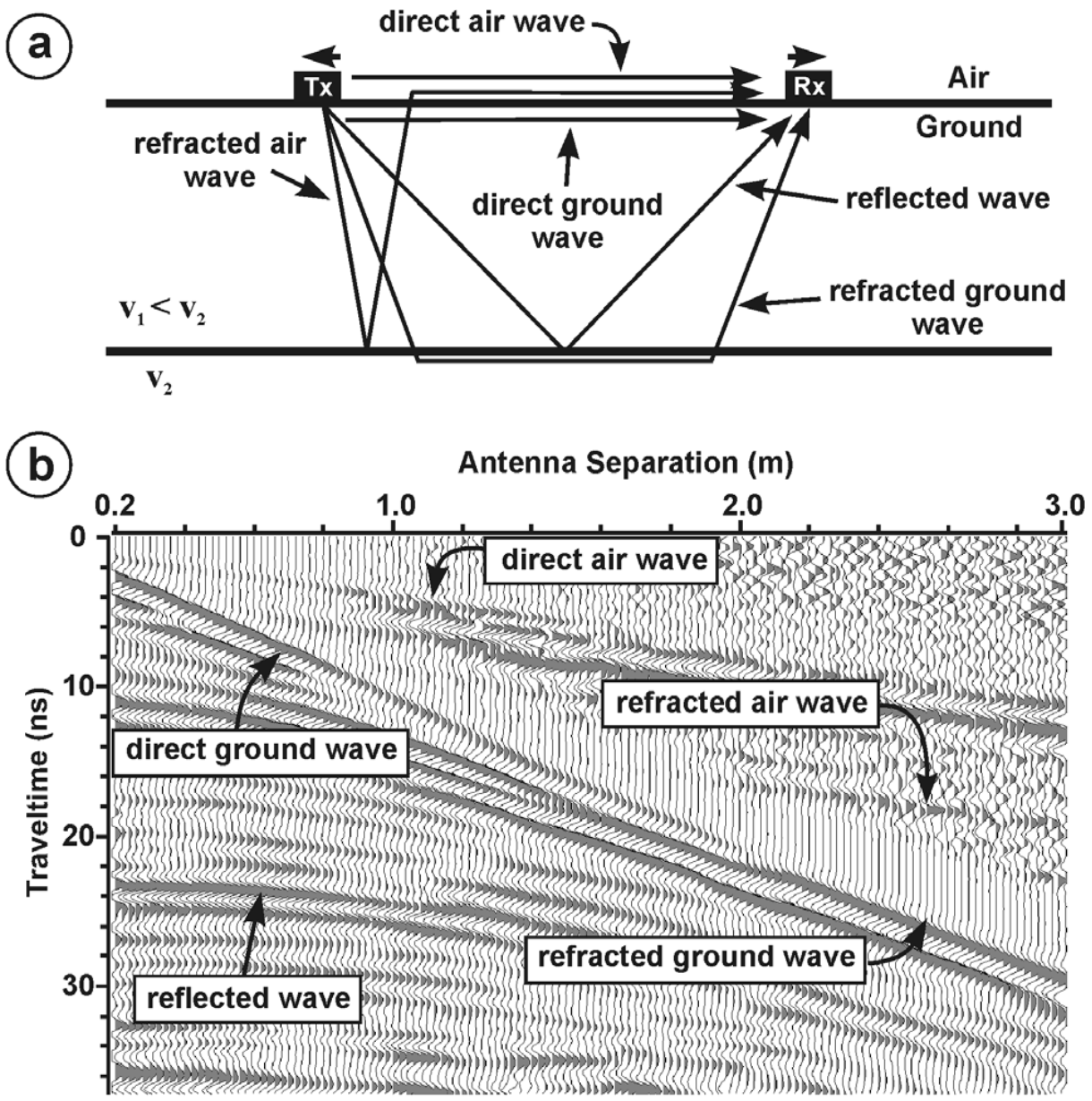

Figure 2.1: Diagram illustrating electromagnetic wave raypaths in the near surface and an example GPR data set (common-midpoint sounding) showing these events (taken from Steelman and Endres [2010]).

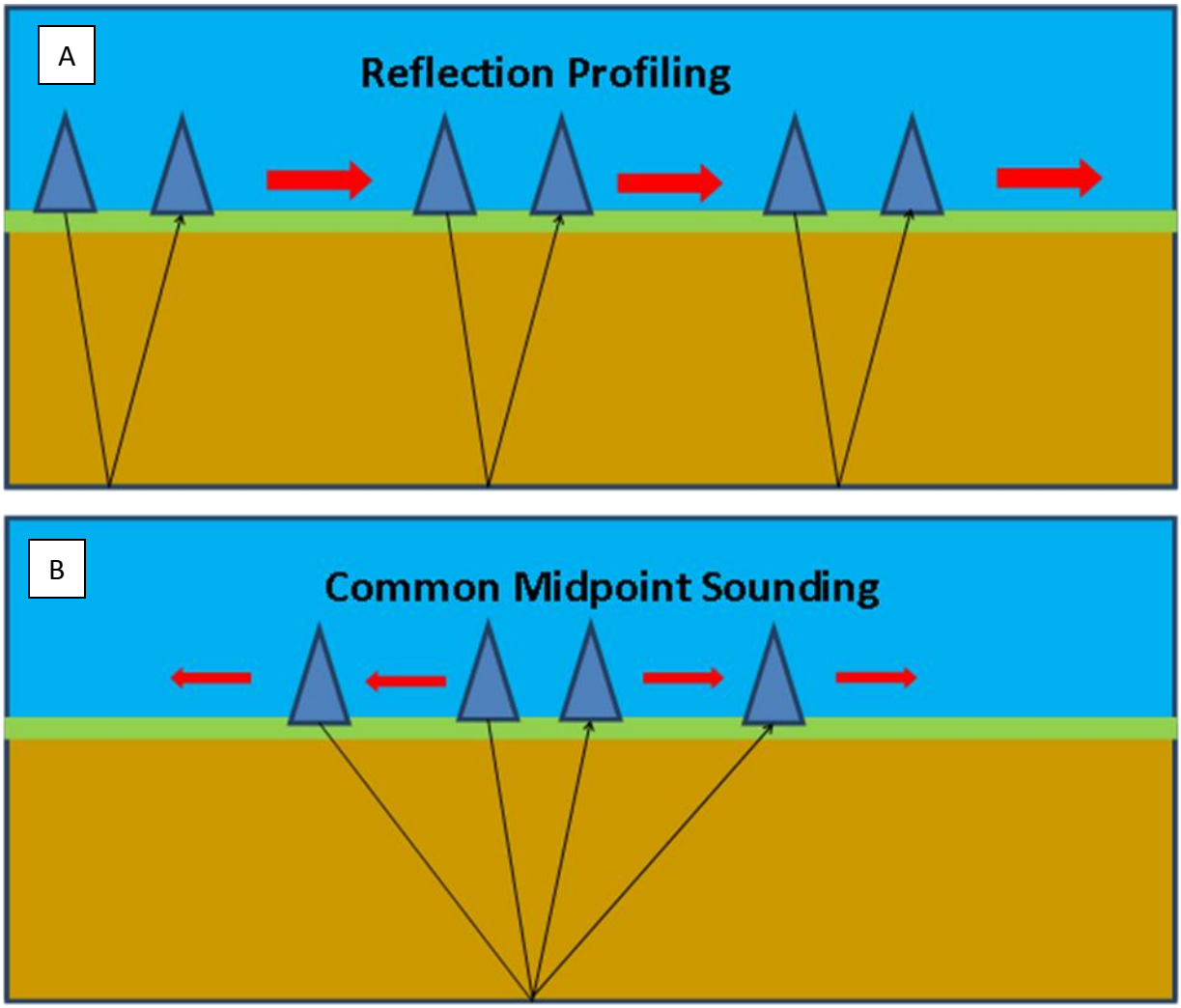

Figure 2.2: Schematic of GPR reflection profiling and common-midpoint sounding techniques.

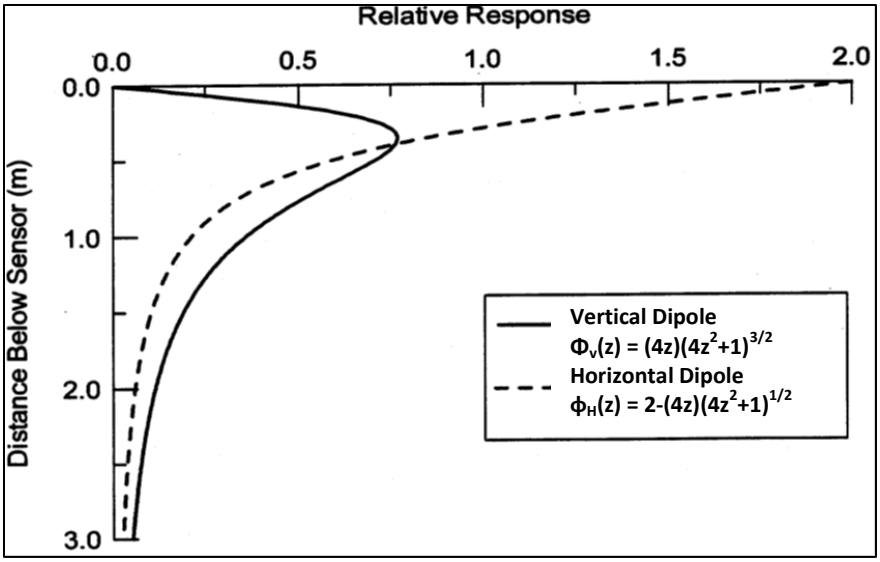

Figure 2.3: The vertical and horizontal dipole response functions for a ground conductivity meter with a 1 m coil separation (Taken from, Sudduth et al., 2001).

3.0 Methodology and Approaches

3.1 Site Characterization

The test site (43.525153,-80.178223) is located within the ARS (Figure 3.1), within the city of Guelph. This area was extensively glaciated during the Pleistocene era, most recently during the Wisconsin glacial episode (115-10 ka), resulting in thick quaternary deposits covering the Silurian-aged dolostone bedrock (Cole et al., 2009; Kunert et al., 2002). This site is being actively studied by researchers at the University of Guelph, with many of these studies focused on nitrate contamination and transport.

The ARS is situated within the outwash plain adjacent to the terminal edge of the Paris Moraine and is host to various agricultural activities. The terminal edge of the Paris Moraine runs in the SW-NE direction, and the topography in the area consists of a relatively flat outwash plain with a few small streamlined drumlins and kettle depressions which eventually evolve into a relatively high ridge with a hummocky surface to the southwest (Sadura et al., 2006). The Paris Moraine was created by ice bulldozing rock material in front of the glacier during small advance-retreat cycles of the ice sheet, which caused sands, gravels and clays to be washed out over the previously deposited glacial tills. The deposited material formed a broad outwash plain in front of the ice sheet. The permeable surface and hummocky topography leads to high rates of recharge and large aquifers are found within the till units (Cole et al., 2009). The large aquifer system in this area supplies drinking water for the city of Guelph and the nearby townships.

For this study, investigations were focused on a 100 meter survey line located in the vicinity of borehole P16 (Figure 3.1). The survey line is located on the 5 m wide grass shoulder between the gravel access road and a cultivated field. The profile is oriented with 0 meters to the south and 100 m to the north. The elevation decreases northward along the survey line into a

depression located between 80 to 90 m. The monitoring well P16 is located at approximately 20 m and is about 2 m west of the line. The borehole log for this well shows a till unit at about 7 m depth overlain by sand and gravels. The water table depth at well P16 ranged between 7.9-8.5 m below the ground surface throughout this study.

3.1.1 Geophysical Characterization

A previous geophysical study by Sadura et al. (2006) characterized the geometry of shallow stratigraphic units within the moraine-outwash system. Based on the GPR reflection profiling they concluded that the outwash area in front of the moraine primarily consisted of braided stream deposits. Unlike the study completed by Sadura et al. (2006) which was situated within the moraine, this study was completed within the proximal outwash moraine.

3.2 Ground-Penetrating Radar

CMP soundings and reflection profiles were conducted along the 100 m survey line every 2 to 6 weeks from August 2011 to June 2012 using Sensors and Software pulse EKKO 1000 and 100 GPR systems (Table 3.1). Table 3.2 gives the CMP sounding and reflection profiling survey design details.

The CMP soundings were acquired with 200 MHz and 450 MHz antennae; however, the data quality and depth of penetration seen with the 450 MHz antennae was less than that of the 200 MHz data. The Direct Ground Wave (DGW) velocities obtained from the CMP soundings were compared with the gravimetric and precipitation data to examine the ability of the CMP soundings to characterize the hydrogeological systems in coarse grained materials. The reflection profiles were acquired with the 200 MHz antennae since the low frequency antennae were found to perform better in the coarse grained materials. The reflection profiles were conducted to image continuous stratigraphic boundaries under the survey line. Since the depth

of a stratigraphic boundary does not change throughout the year, the changes in arrival times for a particular boundary can be used to characterize the hydrogeological systems above that boundary.

3.3 Electromagnetic Induction

Electrical conductivity measurements were collected along the 100 meter survey line every 2 to 3 weeks using the EM38 and EM31 instruments from July 2011 to June 2012 (Table 3.1). Calibration of the EM38 instrument was done in accordance to the manufacturer's manual (Geonics Ltd. EM38 Operating Manual). The EM31 was calibrated by the manufacturer and did not require further calibration in the field.

During the EM surveys, the apparent conductivity value of each survey position was obtained from the average of 25 readings. The EM38 measurements were taken every 0.25 m along the survey line in both the horizontal and vertical dipole orientations. The instrument was placed on the ground and kept stationary for each measurement. EM31 measurements were taken every 1 m on the ground along the survey line in both the horizontal and vertical dipole orientations' as well. A 12% reduction was applied to the EM31 readings since the manufacturers calibration assumes that the instrument is held at a height of 1 meter during data acquisition.

As part of the EM38 survey procedure, a drift line was completed before the survey. The drift line was positioned on the survey line between 82.5 to 87.5 m, both dipole orientations of the EM38 were collected prior to the survey. This drift line was then compared to the actual EM38 readings collected between 82.5 and 87.5 m during the survey and the difference between the readings represented the EM38 instrument drift.

The EM data provided insight to the variations seen in the average apparent conductivities

across the survey line and throughout the year. By utilizing multiple coil separations and instrument dipole orientations, the variations in average apparent conductivities with depth were could be inferred. The average apparent conductivity data were qualitatively compared with the gravimetric and weather data collected at the site.

3.4 Electrical Resistivity Tomography

ERT surveys were conducted along the 100 m survey line using an IRIS Instruments Syscal Junior unit with 48 electrodes every 2 to 6 weeks from July 2011 to June 2012 (Table 3.1). Table 3.3 gives the survey details for the ERT data acquisition. Larger-scale (i.e. field scale) ERT surveys were conducted to capture the long-period seasonal changes along the entire survey line. The higher resolution ERT surveys were acquired to capture short-period dynamic processes in the shallow subsurface.

3.5 Auxiliary Measurements

During the 2-3 week interval surveys, soil moisture variations were monitored using gravimetric soil samples collected at four equally spaced locations along the survey line: 20 m, 40 m, 60 m and 80 m (Table 3.1). These sampling locations coincide with four of the CMP survey locations, and are in the vicinity of where the high resolution ERT surveys were completed. Gravimetric samples were collected in 10 cm depth increments using a ¾-inch soil science probe to a maximum depth of 1 m; this depth coincided with a layer of gravel or boulders. Gravimetric water contents were determined from oven dried samples using the following equation:

$$\theta_G = \frac{(Weight\ of\ the\ wet\ soil - Weight\ of\ pan) - (Weight\ of\ the\ dry\ soil - Weight\ of\ the\ pan)}{Weight\ of\ the\ dry\ soil - Weight\ of\ the\ pan}$$

[14]

At the end of the study, three trenches were dug to a depth of one meter at the 10 m, 50 m and 85m locations (Appendix A). Bulk density samples were collected at three depth intervals (0-25 cm; 25-50 cm; 50-1 m) which represented three soil horizons seen within the 10 m and 50 m trenches. However, due to the presence of cobbles and boulders at the site, accurate bulk densities could not be determined. At stations 10 m and 50 m, the cobbles and boulders were observed throughout all three of the identified soil horizons and the abundance of these coarse grained materials increased with depth. At station 85 m, the cobble and boulder sized material was not seen until around 75 cm depth.

Water table depth measurements were collected with a Solinst water level probe at the well P16 throughout the geophysical monitoring periods (Figure 3.2). Atmospheric temperature, precipitation, soil temperature, and wind speed/direction was monitored at the Turf Grass Institute in Guelph located approximately 4.5 km from the ARS. The precipitation and temperature data are plotted on Figure 3.2.

3.6 Data Analysis

3.6.1 GPR Data Analysis

The GPR data analysis was performed using Sensors and Software's EKKO View Deluxe™ and Sandmeier Software's REFLEXW™. The EKKO View Deluxe™ software was used for preliminary data preparation such as merging line files and zero time adjustments. Subsequent processing and analysis was completed with REFLEXW™. Table 3.4 summarizes the processing steps for the 200 MHz and 450 MHz data.

The DGW velocities were determined from the CMP data by picking both the leading

and lagging crossover of the first positive peak of the DGW event. It was determined that the average of both of the picked events yielded the most representative DGW velocities. The averaged DGW velocities were then compared to the gravimetric water contents and precipitation data.

The EM velocities to three reflection events were determined using NMO analysis of CMP data collected with the 200 MHz antennas. These velocity profiles were used to monitor temporal changes in the soil water content in the reflection profiling data by utilizing the two-way traveltime measurements to a fixed stratigraphic reflection event.

3.6.2 ERT Data Analysis

Analysis of ERT data was done with IRIS Instrument's Prosys II™ and Geotomo Software's RES2DINV™. A least squares inversion using the Gauss-Newton optimization method was completed with a half width unit spacing in order to increase the resolution of the near surface. The ratio of the thickness of the first layer to that unit electrode spacing was 0.125 with a factor of 1.1 to increase the layer thickness with depth. Additionally, a least squares time-lapse inversion was completed with the first data set as the reference model and a constraint weight of 0.2.

3.6.3 EMI Data Analysis

A drift correction was applied by subtracting the drift effect from the EM38 measurements (refer to section 3.3) followed by a moving average spatial filter to reduce noise; the mean was taken across a 4 m window. The EM31 data did not require be drift correction or a moving average filter.

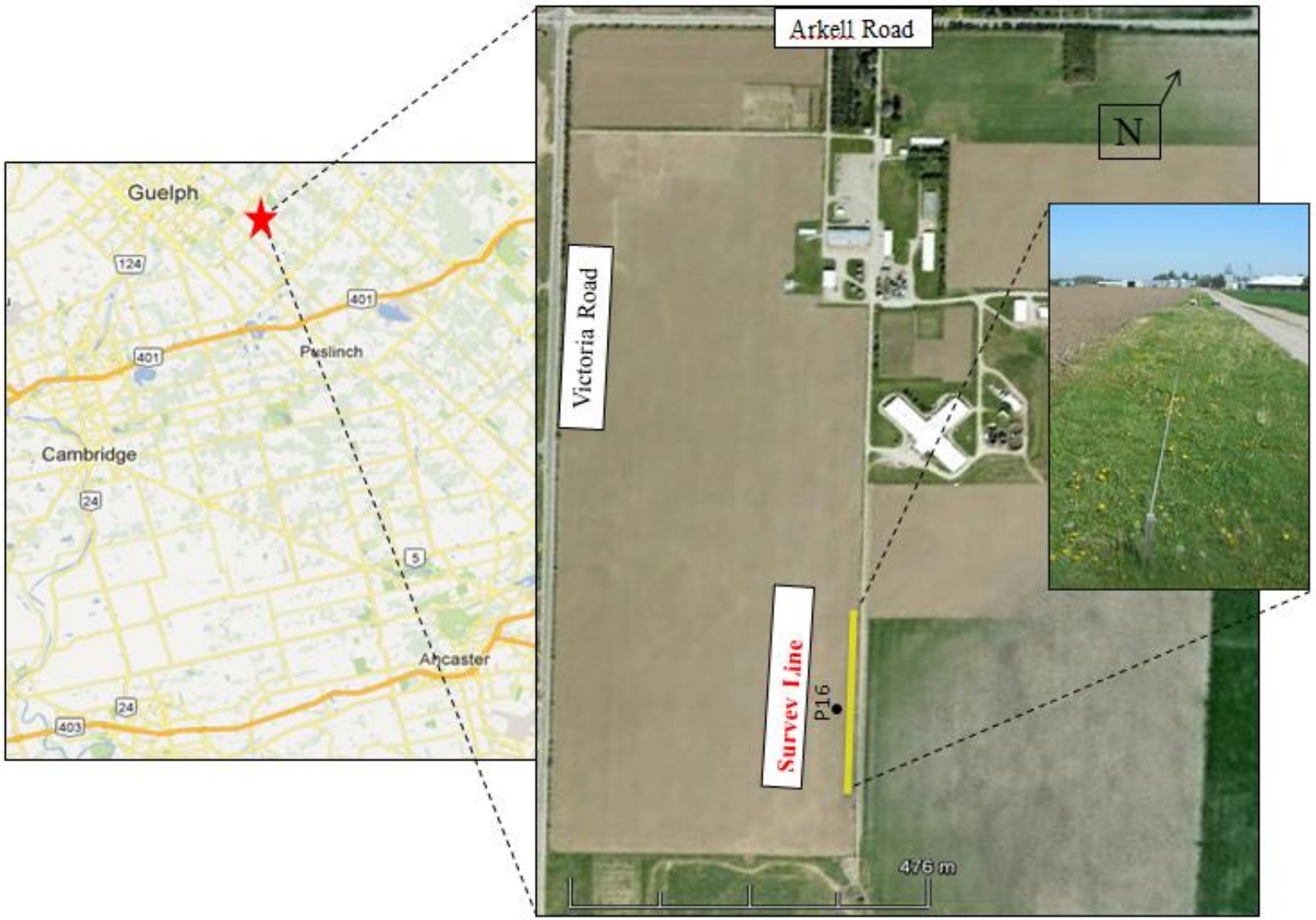

Figure 3.1: Map (Google Maps) and satellite image (Google Earth, May 2014) showing location of survey line at the Arkell Research Station.

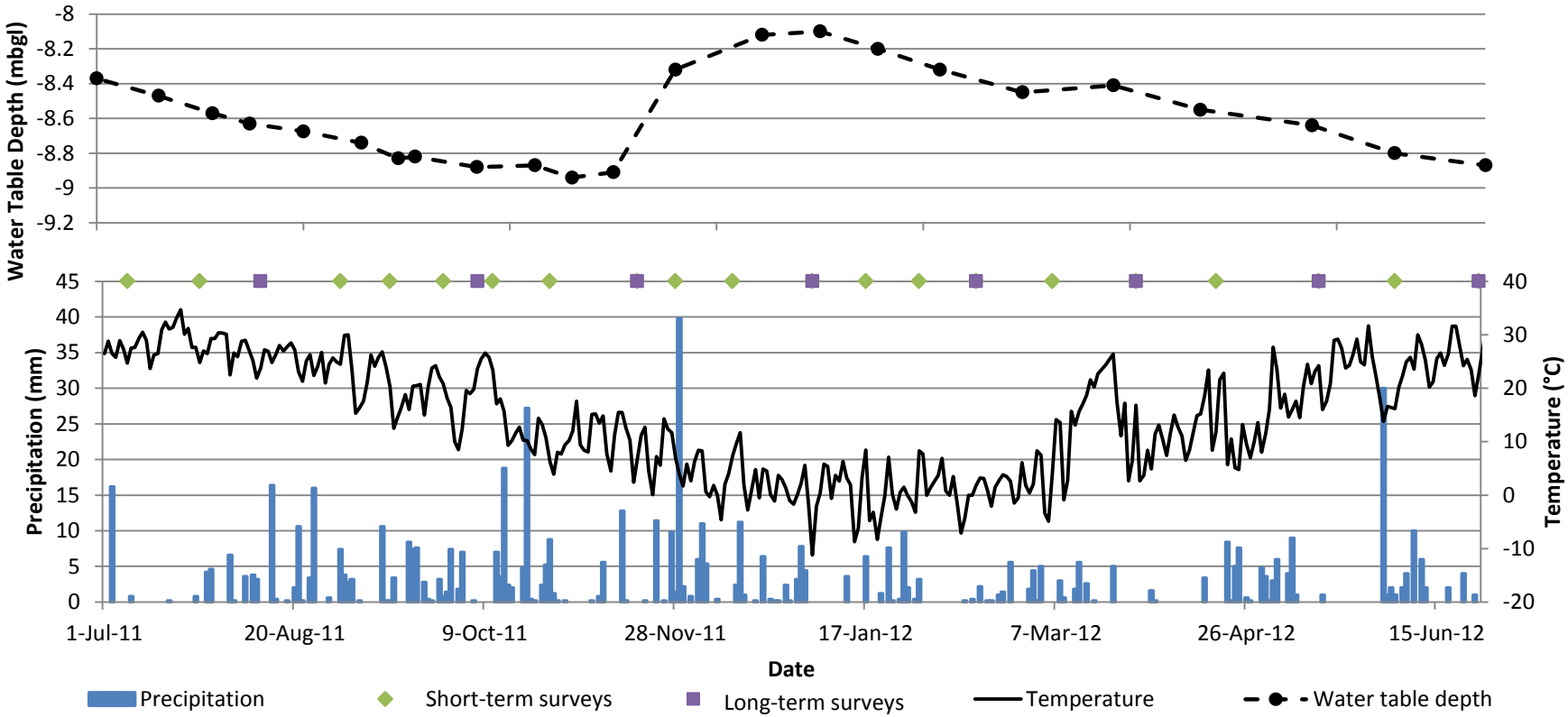

Figure 3.2: Weather data collected from the Turf Grass Institute as well as water level measurements from well P16. Short and long term survey acquisition dates are also indicated.

Table 3.1: Summary of geophysical field data collection

	ERT 0.25 WennerSch @10m	ERT 0.25 WennerSch @ 50 m	ERT 0.25 WennerSch@ 85m	1m Roll Along	EM31 H	EM31 V	EM38 V&H	200 Mhz CMP	200Mhz Reflection	Water table height	Gravi
24-May-11										X	
07-Jul-11		X					X				X
12-Jul-11									X	X	
19-Jul-11							X	X	X	X	X
26-Jul-11	X		X				X			X	X
10-Aug-11				X	X	X	X			X	X
23-Aug-11										X	X
01-Sep-11	X	X	X			X	X			X	X
12-Sep-11											
14-Sep-11	X	X	X		X	X	X			X	X
28-Sep-11	X	X	X		X	X	X			X	X
07-Oct-11				X				X	X	X	X
11-Oct-11	X	X	X		X	X	X			X	X
26-Oct-11	X	X	X		X	X	X	X		X	X
09-Nov-11								X		X	X
18-Nov-11	X	X	X	X	X	X	X	X	X	X	X
28-Nov-11	X	X	X		X	X	X	X		X	X
13-Dec-11	X	X	X		X	X	X	X		X	X
03-Jan-12	X	X	X	X	X	X	X	X	X	X	Frozen
17-Jan-12	X	X	X		X	X	X	X		X	Frozen
31-Jan-12	X	X	X		X	X	X	X		X	Frozen
15-Feb-12	X	X	X	X	X	X		X	X	X	Frozen
06-Mar-12	X	X	X		X	X	X	X		X	Frozen
28-Mar-12	X	X	X	X	X	X	X	X	X	X	X
18-Apr-12	X	X	X		X	X	X	X		X	X
15-May-12	X	X	X	X	X	X	X	X	X	X	X
04-Jun-12	X	X	X		X	X	X	X		X	X
26-Jun-12	X	X	X	X	X	X	X	X	X	X	X

Table 3.2: Survey design parameters for the GPR data (CMP soundings and reflection profiling)

	200 MHz CMP	**450 MHz CMP**	**200 MHz Reflection**
Sampling Location	Every 10 m along the 100 m survey line	Every 10 m along the 100 m survey line	Entire 100 m survey line
Frequency	2-3 weeks	2-3 weeks	6 weeks
Step Size	0.1 m	0.05 m	0.1 m
Offset Range*	0.5 m to 6 m	0.25 m to 3 m	0.5 m
Time Window	200 ns	80 ns	200 ns
Sampling Interval	800 ps	100 ps	800 ps
Stack	64	64	64

*the maximum offset allowed for the separation of the direct air and direct ground wave fields

Table 3.3: Survey design for the field scale and high resolution ERT surveys

	High Resolution ERT	**Field Scale ERT**
Frequency	2-3 weeks	6 weeks
Location	10 m, 50 m and 85 m along survey line	Entire 100 m survey line
Array	Wenner	Wenner
Electrode Spacing	0.25 m	1 m
Signal Duration	1000 ms	1000 ms
Stack	4-6	4-6

Table 3.4: Processing parameters for the 200 MHz and 450 MHz data.

	Dewow Filter	**Gain Function**	**Bandpass Frequency**	**Mean**
200 MHz CMP	Time Window: 11.46618 ns	Start time: 0 ns Linear gain: 6.058288 Exponent: 0.601158 Max. gain: 500	Low cutoff: 0 Lower plateau: 50 Upper plateau: 100 Upper cutoff: 200	n/a
450 MHz CMP	Time Window: 3.978022 ns	Start time: 0 ns Linear gain: 2 Exponent: 10 Max. gain: 5000	Low cutoff: 0 Lower plateau: 200 Upper plateau: 600 Upper cutoff: 800	n/a
Reflection	Time Window: 13 ns	Start time: 0 ns Linear gain: 3 Exponent: 3 Max. gain: 1000	Low cutoff: 0 Lower plateau: 50 Upper plateau: 100 Upper cutoff: 150	Mean range: 3

4.0 Hydrogeophysical Data Analysis

The three hydrogeophysical methods (GPR, EMI and ERT) that were examined have been evaluated separately in terms of their potential to provide information about the subsurface dynamics in a stony coarse grained material. The variations in the measured responses were assessed with respect to both the spatial and temporal changes, and compared to available hydrological data. The qualitative relationship between the hydrogeophysical responses and the hydrogeological information (i.e., precipitation data, grain size information and gravimetric water contents) were examined. Additionally, the relationship between the GPR and EMI responses were quantitatively compared to the gravimetric data that was collected throughout the study.

4.1 Ground Penetrating Radar- Common Midpoint Surveys

The CMP surveys conducted with the 200 MHz and 450 MHz antennas at stations 20 m, 40 m, 60 m and 80 m along the survey line were analyzed to obtain DGW and NMO velocity information. The CMP data can be found in Appendix B. As discussed in Chapter 2, the NMO and DGW velocities have an inverse relationship with water content.

The DGW velocities obtained from the CMP data and the corresponding water content values derived from gravimetric sampling are shown in Figure 4.1. Significant variations in DGW velocity are observed over the duration of the study that qualitatively reflect the soil moisture conditions. During the summer of 2011, the DGW velocities are relatively high during dry conditions (August 10, 2011). The DGWs begin to decrease (September 28, 2011 to November 9, 2011) as conditions become wetter. During the winter months (November 9, 2011 to January 3, 2012), the DGW velocities remain relatively low during a period of unfrozen wet conditions. The DGW velocities start to increase again around March 28, 2011 in response to

observed drier soil conditions.

Figure 4.2 shows the overall spatial trends in the DGW velocities and soil moisture along the profile line. Considering the average values at each station for the monitoring period, it can be seen that DGW velocities progressively decreased approximately 15% (0.086 m/ns to 0.0728 m/ns) from 20 m to 80 m (i.e., from the crest of the profile to the depression). This trend is consistent with the gravimetric data where there is roughly a 43% (0.23 to 0.33) increase in the average gravimetric water contents as you move from 20 m to 80 m on the survey line. Hence, both Figures 4.1 and 4.2 suggest that there is a qualitative relationship between DGW velocities and soil moisture.

Figure 4.3 examines the quantitative relationship between DGW velocities and soil moisture conditions; this analysis was performed in terms of the inverse of the DGW velocity (i.e., $1/V_{DGW}$). While there appears to be a qualitative relationship between the DGW velocities and soil moisture conditions in Figure 4.3, there is significant scatter in these data, particularly at 60 m and 80 m. Hence, the correlation between the DGW velocities and the gravimetric water contents at all four stations as quantified by the R^2 values were not as strong as might be expected.

NMO analysis was performed on the CMP data to examine spatial variations in subsurface EM wave velocities along the survey line. Steelman and Endres (2012) provide an overview of the concepts behind the use of NMO analysis for vertical soil moisture characterization. The data quality and depth of penetration deteriorated at the northern end of the survey line (i.e., from approximately 70 m to the end of the line). This signal degradation is thought to be the result of increased electrical conductivities in the near surface materials which is illustrated in the ERT results below (see Section 4.4 and 4.5 below). Hence, the CMP data

collected at 80 m and 90 m were excluded from the NMO analysis due to the data quality issues.

Three reflections events that were consistently identified on the CMP data throughout the monitoring period were used in the NMO analysis. An example CMP data set from October 7, 2011 showing these three events is given in Figure 4.4. The NMO analysis of each event yielded an average velocity (called the NMO velocity) of the material between the surface and reflecting interface, as well as zero offset traveltime which indicates the relative depth of the corresponding interface.

Figure 4.5 shows the cross-sectional profile of the NMO analysis results along the survey line for different seasonal conditions. It can be seen that overall higher NMO velocities occur during the drier summer conditions while lower NMO velocities were found during the wetter fall through spring period. In addition, there appears to be a significant increase in NMO velocity with traveltime during the wetter conditions. These trends are also apparent when the NMO analysis results are examined as time series covering the monitoring period at selected stations (Figure 4.6). Further, the time series reveals more velocity variability in the results for the DGW and shallowest reflection event in comparison to the two deeper reflection events. This behavior is consistent with greater variation in soil moisture in the vicinity of the surface with the degree of soil moisture changes decreasing with depth.

4.2 Ground Penetrating Radar- Reflection Profiling

The 200 MHz antennas were used for the reflection profiling along the entire length of the survey line (1 m to 100 m). Due to increased deterioration of the data quality and depth of penetration at the northern end of the survey line, only the data between 1 m to 70 m of the reflection profile line was analyzed. An example of the reflection profiling acquired during this study is shown in Figure 4.7; images of the reflection profiles collected throughout the survey

can be found in Appendix B. On the reflection profiling data, the continuous reflection event around 90 ns could be consistently imaged and identified throughout the monitoring period (Figure 4.7); this reflection event corresponds to the deepest reflection event used in the CMP data analysis.

The depth of the reflection event was estimated for the locations where CMP surveys were conducted; the results of this analysis averaged over the monitoring period are shown in Figure 4.8. The estimated depth of the reflection event ranges from 4 m to almost 6 m across the survey line. The continuous nature and amplitude of this reflector event suggests it corresponds to a continuous geological boundary such as a stratigraphic interface or the water table. The water table depth was observed at approximately 8 mbgl at the monitoring well P16 along the profile line. Hence, it is likely that this reflection event corresponds to an overlying stratigraphic boundary. The borehole log of P16 (Figure 4.8), which is located at 20 m on the survey line, shows that there is a boundary between the upper silty sand gravel unit and the underlying unit comprised of sand and minor gravel fraction around 5 m. This lithologic boundary is at a similar depth as the continuous reflection boundary seen in the reflection data.

The two-way traveltime of this reflection event was determined for 1 m to 70 m and is plotted as a function of position in Figure 4.9; these data are shown in Figure 4.10 as the change relative to the first survey date on July 19, 2011. Since the depth of the stratigraphic boundary corresponding to this reflection event does not change, fluctuations in the soil moisture above this boundary will change its two-way traveltime throughout the year.

Looking at the arrival times qualitatively you can associate the earliest arrival times to wetter conditions and the latest times to drier conditions (Figure 4.9). According to the GPR reflection data, the earliest arrival time was on November 18, 2011 when the conditions were

very wet and the latest arrival times was on February 15, 2012 when the ground was frozen. The temporal changes in two-way traveltimes appear to correlate with the general trends seen in the precipitation data throughout the year (Figure 3.2); however, this is not what one would expect. This behavior is consistent with delayed recharge into the subsurface and a bias towards the higher conductivity upper near surface.

4.3 Electromagnetic Induction Results

Apparent conductivity readings were obtained using the EM38 and EM31 along the entire length of the 100 m survey line at 0.25 m and 1 m intervals, respectively. The EMI data can be found in Appendix D. As discussed in Chapter 2, the EM instruments are very sensitive to changes in the subsurface conductivity. The EM38 and EM31 data collected along the survey line has been plotted for select dates to illustrate the effects of varying seasonal conditions (Figures 4.11 and 4.12, respectively).

It can be seen in Figure 4.11 that the apparent conductivities measured with the EM38 using the horizontal dipole orientation are greater than those measured with the EM38 vertical dipole orientation during wetter fall to spring period (i.e., October 26, January 3 and March 28). During the relatively drier summer months (i.e. July 19, 2011 and June 26, 2012), the apparent conductivities measured in both the horizontal and vertical dipole are similar. This behavior is consistent with the development of a higher conductivity surface layer during the fall-spring due to increasing water content that dissipates during drier summer period.

It can also be seen in Figure 4.11 that there is lateral area of elevated apparent conductivity values in the vicinity of the depression at the north end of the survey line (i.e., positions 70 to 100 m). This lateral change in apparent conductivity correlates with the pattern of increasing gravimetric water contents measured along the survey line. Further, this lateral variation is more

pronounced during the wetter fall to spring period and can be observed in both dipole orientations. This behavior suggests that there is a larger seasonal variation in soil moisture in the depression area and that these variations extend to greater depths than other portions of the survey line, potentially indicating the occurance depression focused infiltration.

The apparent conductivity data measured with the EM31 shown in Figure 4.12 displays much less temporal and lateral variations than the EM 38 data in Figure 4.11. In addition, similar values of apparent conductivity were obtained with both the vertical and horizontal dipole orientations over position range from 0 to 70 m. This response supports the interpretation that the dipole orientation differences seen in the EM38 profiles are due to seasonal conductivity changes in a relatively thin surface layer. While there are elevated apparent conductivity values in the vicinity of the depression at the north end of the survey line (i.e., positions 70 to 100 m) for the horizontal dipole data for the EM31, the vertical dipole data shows very little, if any, lateral changes through the depression. Hence, if depression focused infiltration is affecting the subsurface conductivities, the EM31 vertical dipole data indicates that its effects attenuate significant beyond a critical depth.

To examine the relationship between shallow soil moisture and the apparent conductivity obtained with the EM38, the time series of gravimetric water content measurements and the corresponding EM38 apparent conductivity data are given in Figure 4.13 for positions 20, 40 60 and 80 m along the survey line. The gravimetric water contents represent the average value over the upper 0.4 m while the EM-38 values are an average across a 6 m section of the survey line centered at positions 20, 40, 60 and 80 m. Similar to the GPR data shown in Figure 4.1, there appears to be a qualitative relationship between the EM38 apparent conductivities measured in the horizontal dipole orientation and soil moisture conditions. This potential relationship is

further examined in Figure 4.14 where the correlation between apparent conductivity and water content were determined for four gravimetric sampling positions. During two of the site visits, conditions were very wet from a previous large rain fall event (November 28, 2011) and a mid-season thaw event (January 31, 2012), these conditions caused water to pool at the surface. To assess whether or not these data effect the correlation between the apparent conductivities and the water contents two scenarios were assessed. The first scenario included all of the survey visits and the second scenario excluded the November 28, 2011 event at all four locations as well as the January 31, 2012 event at the 80 m location. These results indicate a relatively moderate level of quantitative dependence of the EM38 apparent conductivity measurements on the observed moisture contents with a significant component of scattering in these data.

4.4 Field-Scale Electrical Resistivity Tomography

The field-scale ERT surveys were acquired along the entire 100 m survey line; these profiles imaged to a depth of approximately 10 m over most of the survey line. These surveys were conducted at approximately 6 week intervals. These ERT data were inverted and the resulting tomograms are plotted in terms of conductivity (i.e. reciprocal of resistivity).

Figure 4.15 shows tomograms obtained from the field scale ERT surveys were able to detect seasonal variations as well as vertical changes in the conductivity. These tomograms show that the subsurface is vertically divided into two distinct regions: a surface layer and underlying zone. The underlying zone has comparatively lower conductivity and displays little temporal variation in electrical properties.

In contrast, the upper near-surface zone has relatively higher conductivity that exhibits significant temporal variations in the conductivity. In addition, it laterally varies, being relatively thin at the higher south end of the profile and increasing in depth with decreasing

elevation to its greatest thickness in the vicinity of the depression at the north end of the profile. This upper layer exhibits lower conductivity in the mid to late summer (August 11, 2011) which subsequently increases during the fall (November 18, 2011). The upper layer conductivity remain relatively high until early spring (March 28, 2012) at which correlates with the seasonally drier conditions that occur in late summer-early fall followed by the normally wetter conditions encountered during the fall-spring period. Further, there is a significant downward expansion of this zone below the depression imaged on March 28 which persists until the May 15, 2012 tomogram; this behavior is consistent with the recharge following the seasonal thaw event. The onset of drier conditions in early-mid spring and the occurrence a major precipitation event in (June 1, 2012) by the weather observations correspond with the decreasing conductivity conditions and the return of higher conductivities observed in the May 15 and June 26 tomograms, respectively.

4.5 High Resolution Electrical Resistivity Tomography

To obtain improved imaging of the response of the near-surface layer changing soil moisture conditions, high resolution ERT surveys were acquired at three sites along the profile line (i.e., positions 10 , 50 and 85 meters) at a temporal interval of approximately 3-4 weeks. These survey locations are located at the knoll top, mid-slope and depression, respectively, along the profile line. These ERTs cover a length of approximately 16 m with an investigation depth of approximately 2 m. These ERT data were inverted and the resulting tomograms are plotted in terms of conductivity. The complete set of tomograms generated from the high resolution ERT data can be found in Appendix C.

Figures 4.16-4.18 show representative tomograms illustrating spatial and temporal variations observed at 10, 50 and 85 meters, respectively. The improved vertical resolution

obtained from using the smaller electrode spacing permits better imaging of the more dynamic, higher conductivity near surface layer previously observed in the field-scale tomograms. At 10 and 50 m stations, this upper layer is approximately 0.25-0.5 meters thick on the tomograms, this depth roughly coincides with boundary between the upper, finer grained soil layer and underlying very coarse gravel outwash deposits found in the trenches at these locations.

The high resolution tomograms at the 85 m position indicate that the higher conductivity near-surface zone extends to almost 1.5 meters. This depth is consistent with the trenching results which only encountered finer-grained material to its 0.80 meter completion depth. In addition, this upper zone appears to develop a thinner, lower conductivity surface sublayer during the late spring-summer (i.e., July 26, 2011 and June 26, 2012) and winter (i.e., January 31, 2012) period.

To better visualize the temporal variations in conductivity observed in the high-resolution ERT tomograms, one-dimensional mean conductivity depth profiles were generated from the inversion results by laterally averaging the model elements between the 4 and 8 meters positions for each depth level. The resulting mean conductivity profiles for 10, 50 and 85 m stations are given in Figures 4.19-4.21, respectively. Similar seasonal patterns are observed at both the 10 and 50 m stations. The dynamic near surface layer has relatively lower conductivity values during the summer period and higher conductivity conditions in the fall and spring. This pattern correlates with the expected drier summer and wetter fall and spring soil moisture conditions. Further, there is evidence of a seasonal conductivity reduction during the winter, particularly at the 10 m station. This behavior is consistent with the effects of decreasing temperature and freezing on the conductivity of soils. As previously noted from the field scale ERT results, the underlying resistive material show little temporal conductivity variations.

At the 80 m station, the thin surface sublayer exhibits a seasonal pattern similar to that observed for the surface layer at the 10 and 50 m stations. The lower portion of the near-surface higher conductivity zone displays more subdued temporal conductivity variations. This vertical difference in temporal response indicates that the impact of seasonal weather conditions on soil moisture conditions attenuate significant below the surface sublayer at this location.

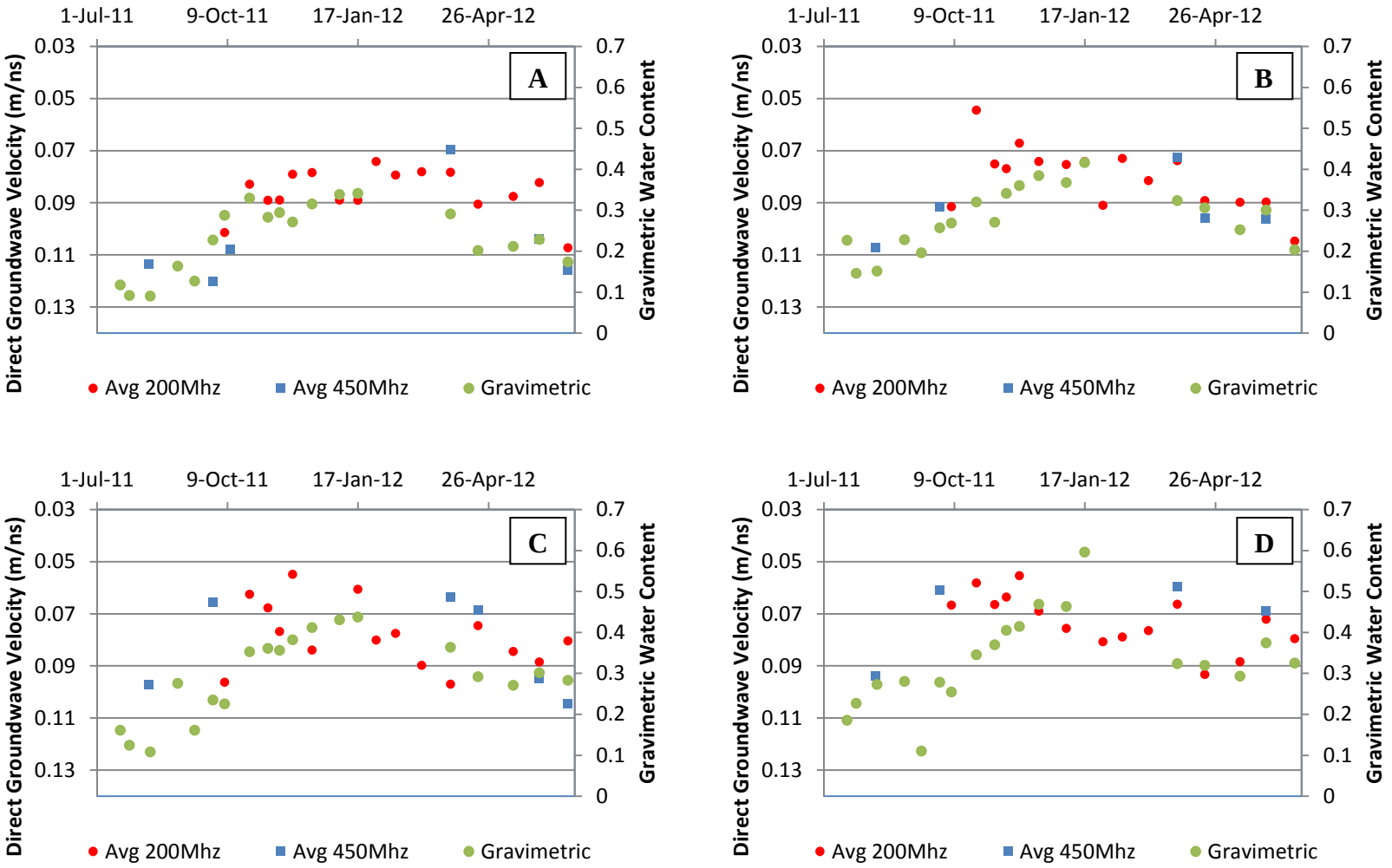

Figure 4.1: Time series of 200 MHz and 450 MHz DGW velocities obtained from analysis of the GPR CMP data and the corresponding gravimetric water contents derived from the gravimetric samples for stations (a) 20 m, (b) 40 m, (c) 60 m and (d) 80 m. The gravimetric water contents are an average value over the upper 1 m of the vadose zone.

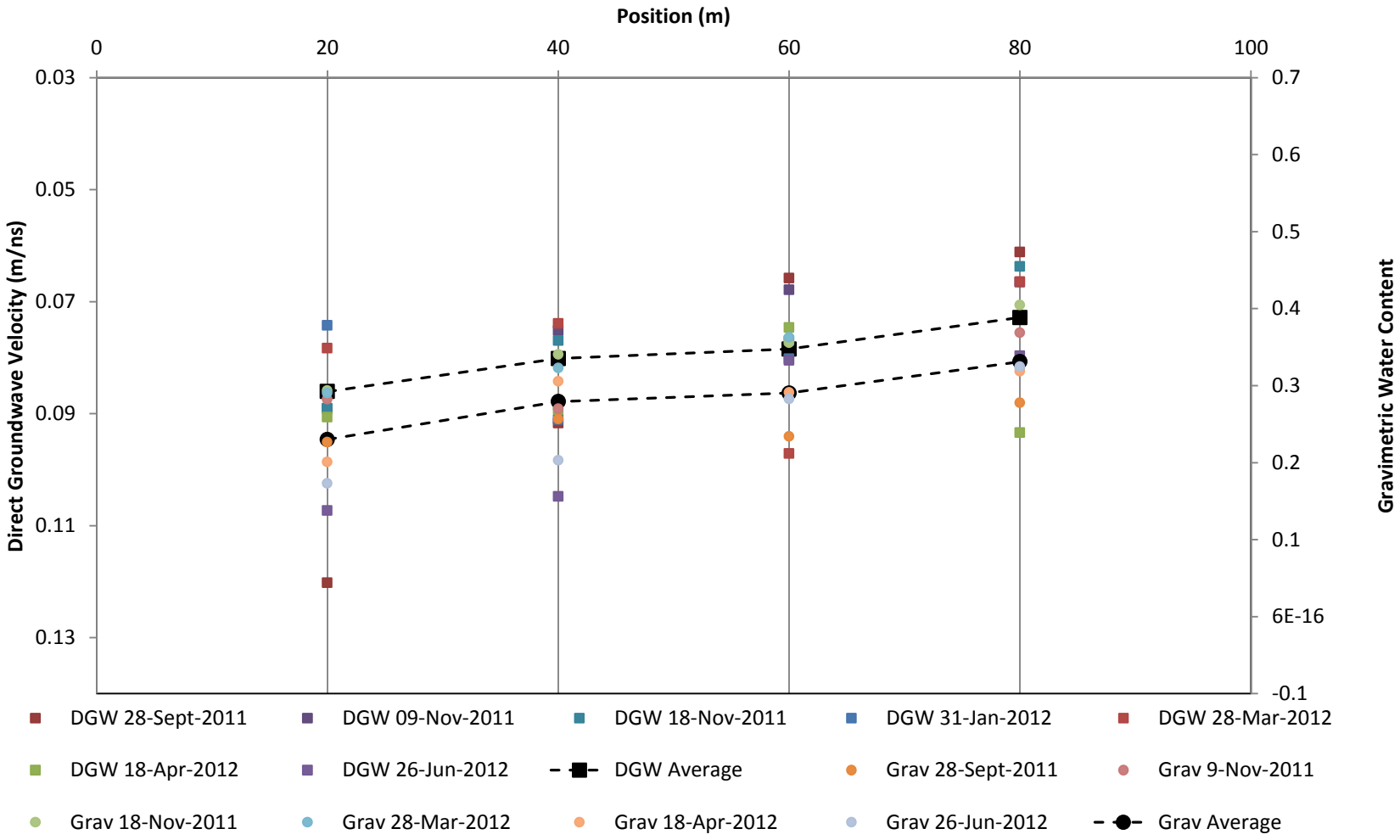

Figure 4.2: DGW velocities and gravimetric water contents plotted with respect to the station position. The average values over the monitoring period of these two parameters are also given. The DGW velocities are marked with squares and the gravimetric water contents are represented with circles with dates given in the legend.

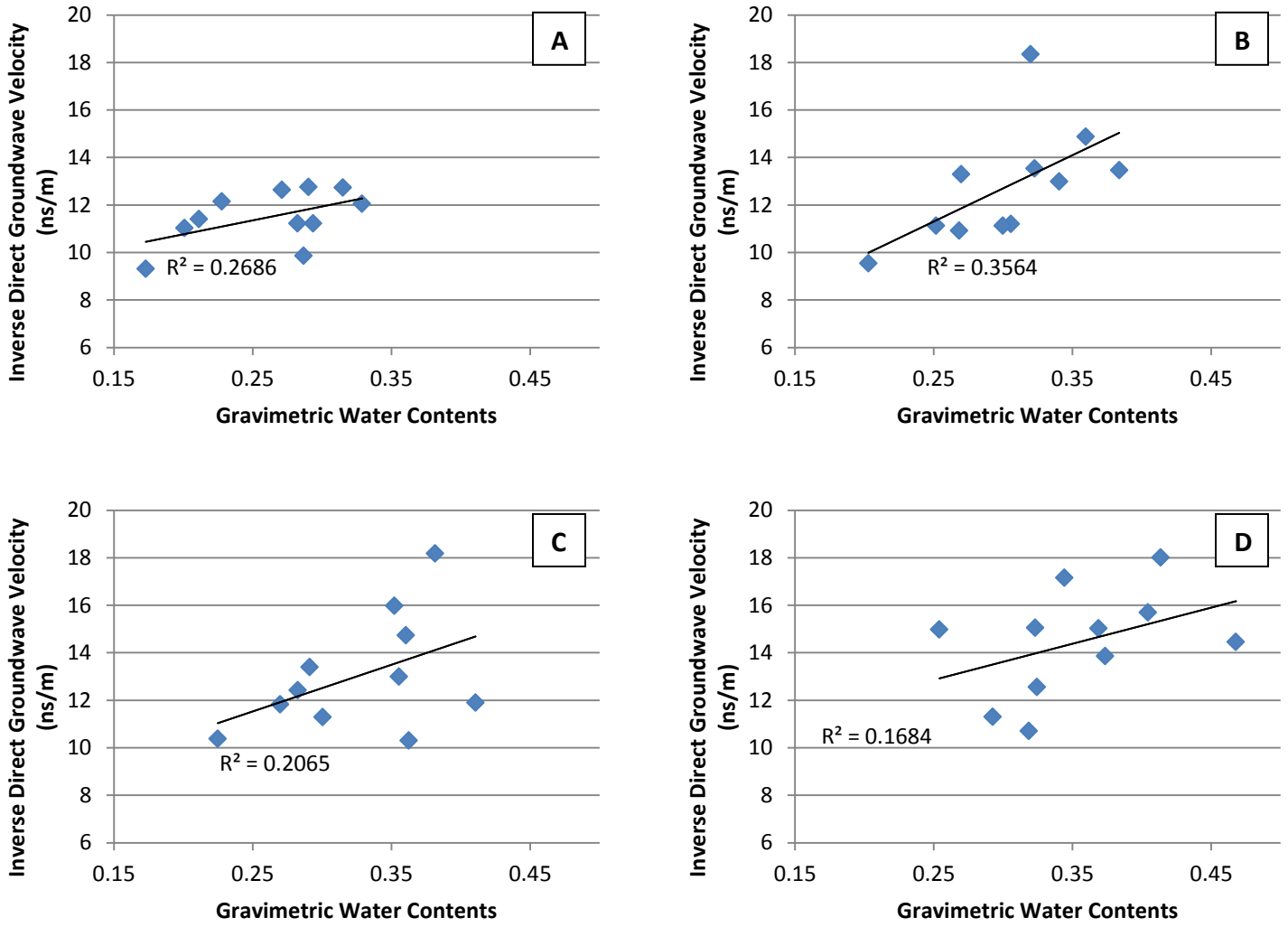

Figure 4.3: Analysis of the relationship between the inverse of the 200 MHz DGW velocity measurements (i.e., $1/V_{DGW}$) and the gravimetric water contents for stations (a) 20 m, (b) 40 m, (c) 60m and (d) 80m.

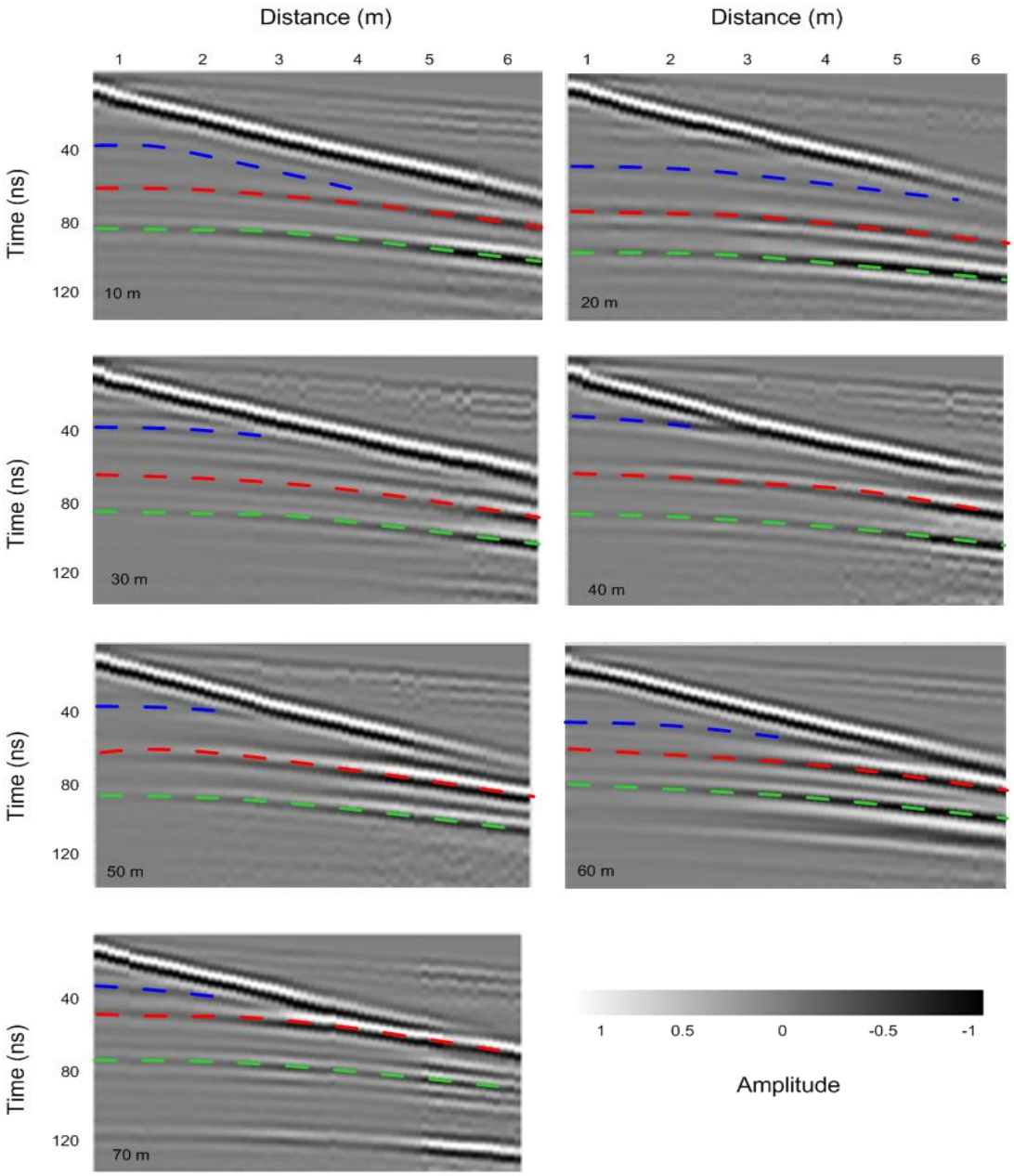

Figure 4.4: An example of 200 MHz CMP surveys collected on October 7, 2011. The three reflection events used in the NMO analysis are marked in blue, red and green.

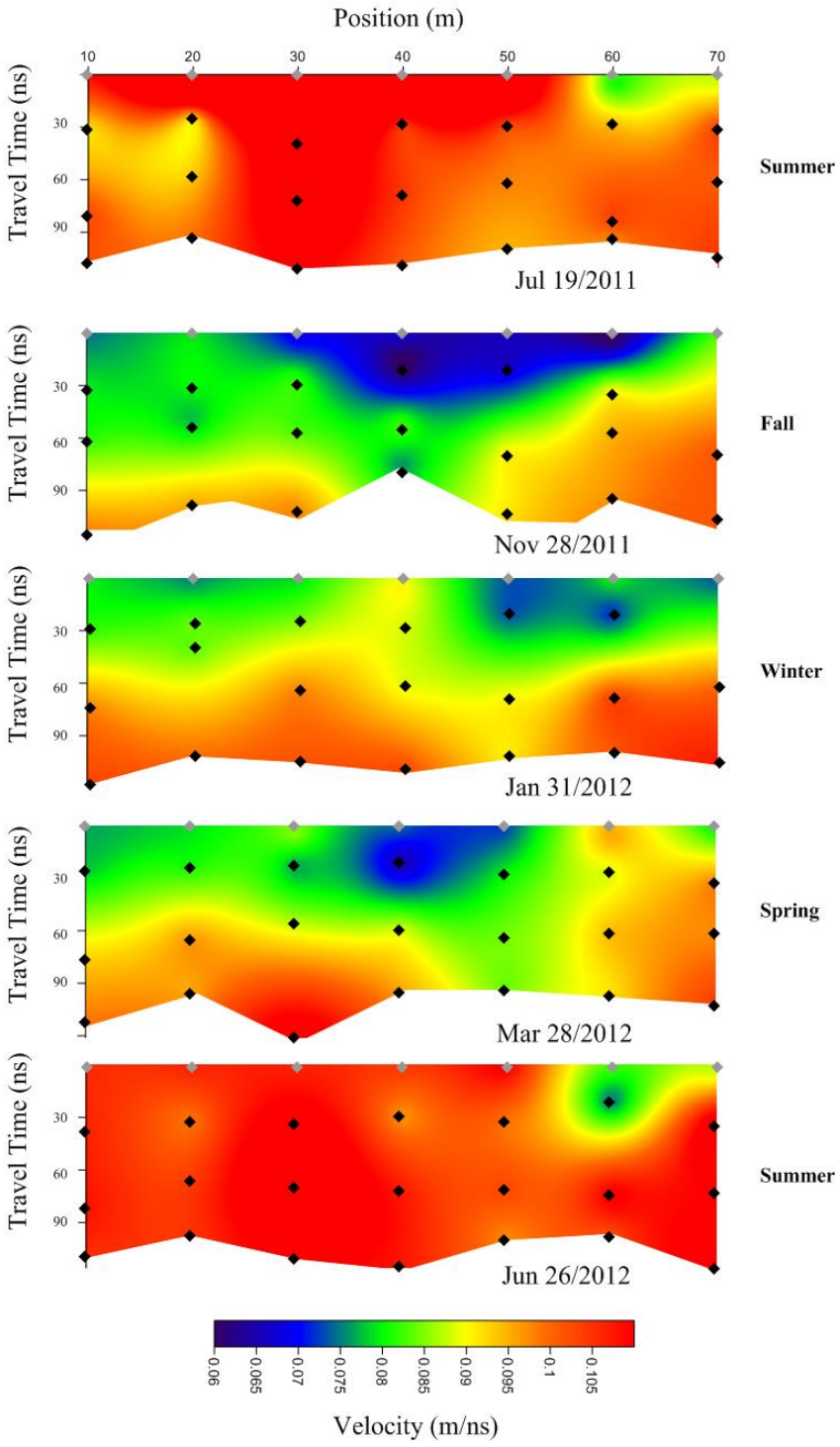

Figure 4.5: Cross sectional profile of the NMO velocities as a function of zero offset time obtained from NMO analysis of CMP sounding data for different seasonal conditions. The DGW velocities are used as an estimate of the velocity along the surface.

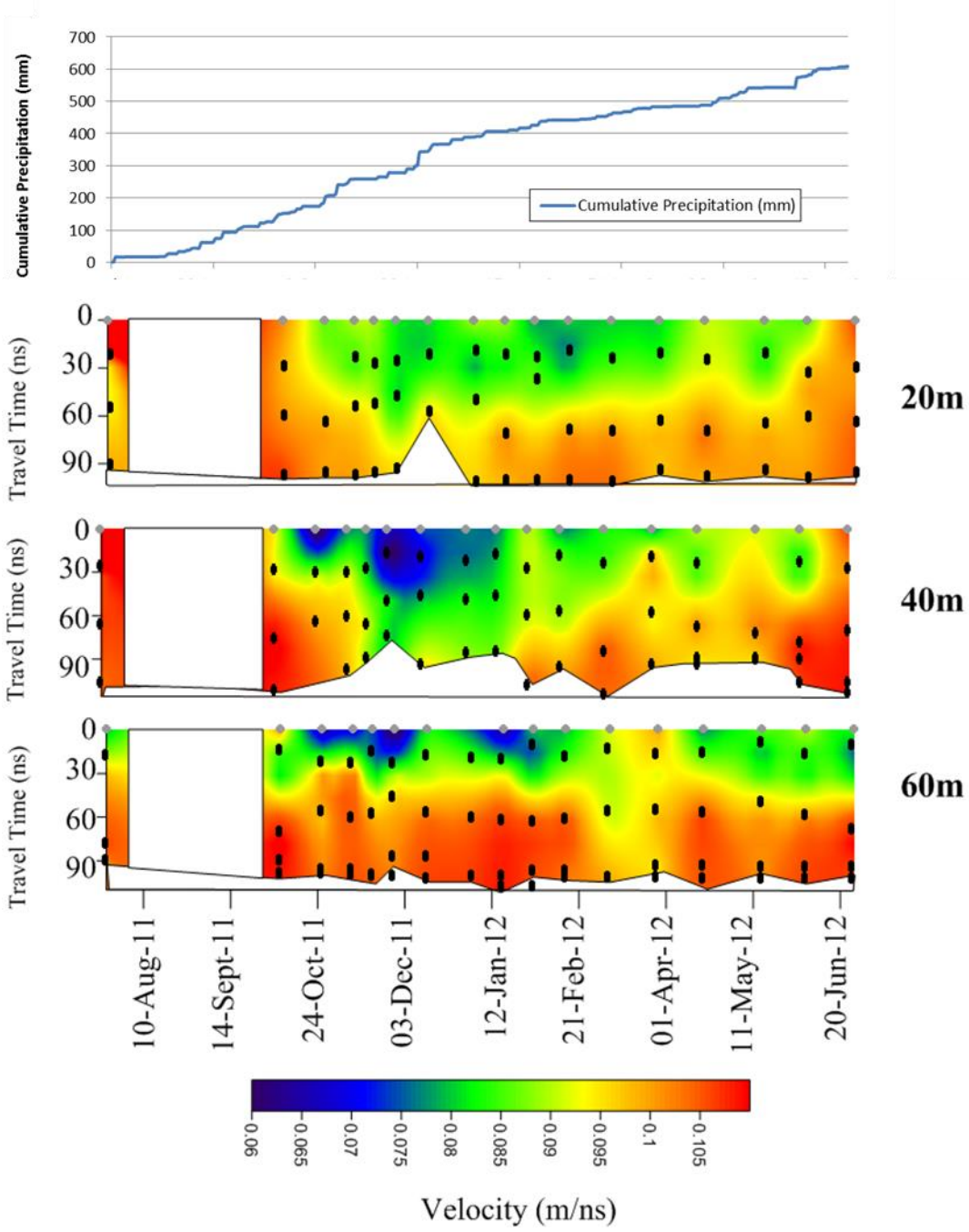

Figure 4.6: Temporal variations of the NMO velocities obtained from the NMO analysis of the CMP data at stations 20 m, 40 m and 60 m.

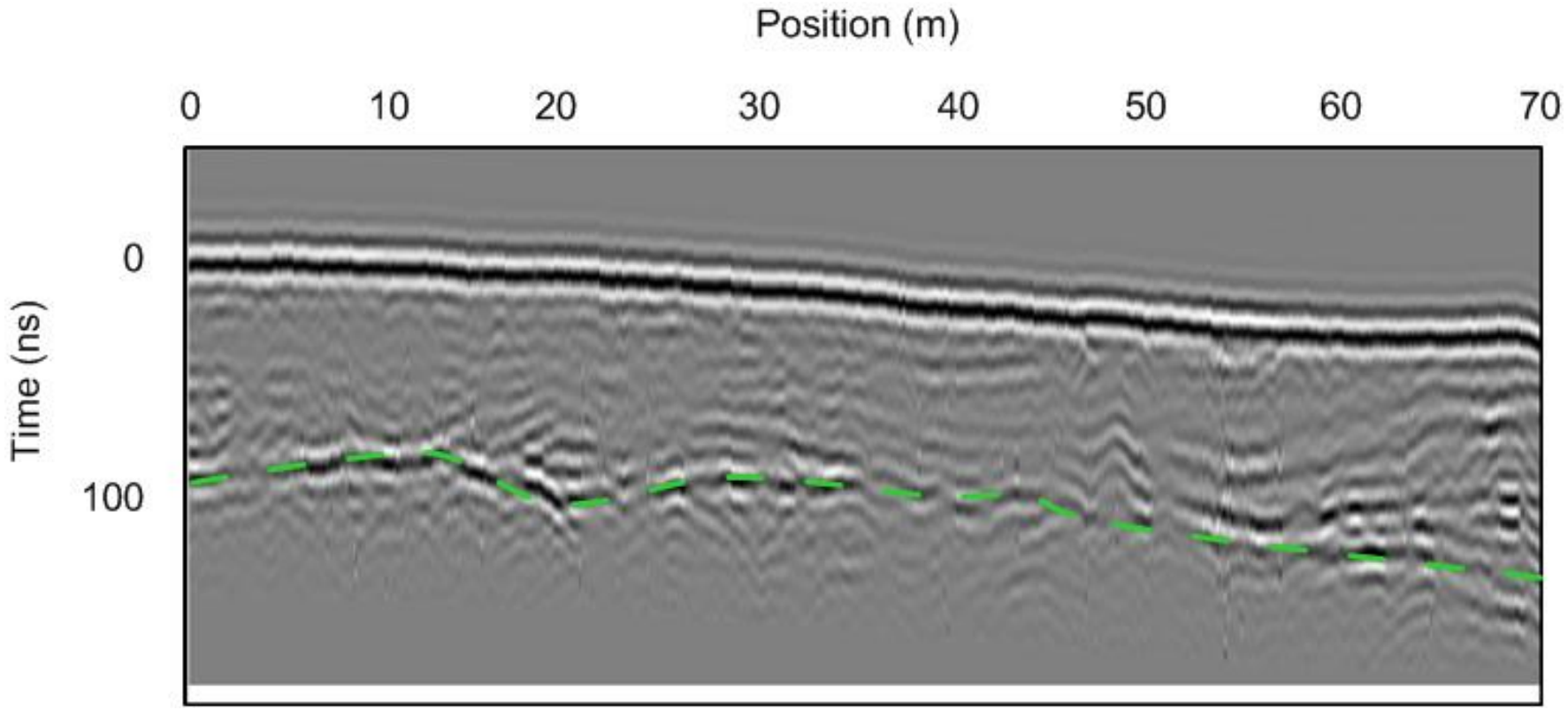

Figure 4.7: An example of the 200 MHz reflection profiling data along the survey line from October 7, 2012. The continuous reflection event consistently identified throughout the monitoring is marked in green. This event correlates with the deepest third reflection event (also denoted by green) seen in the 200 MHz CMP data.

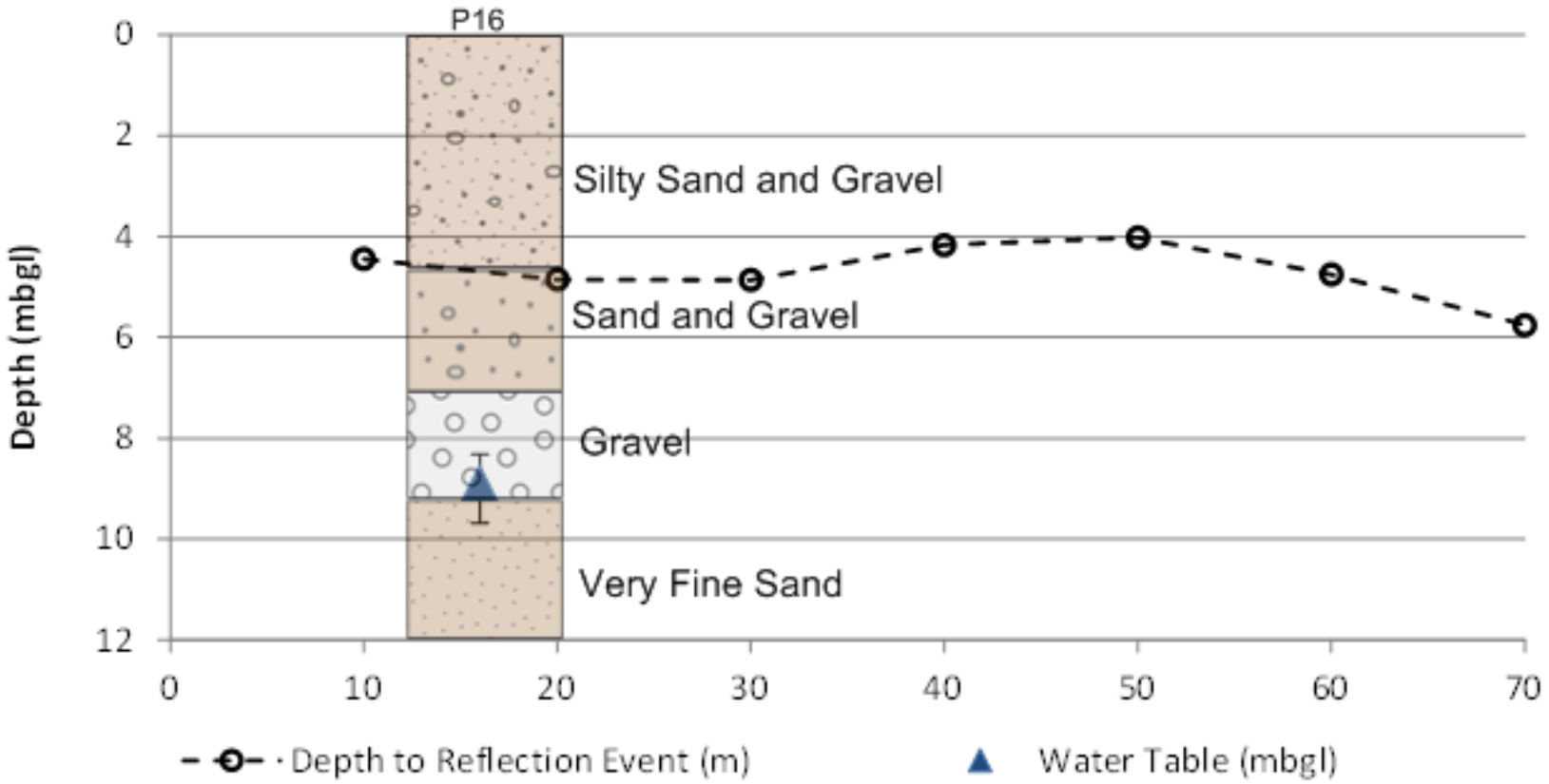

Figure 4.8: Estimated depth to reflection event along the survey line with the driller's log of well P16. The range in water level measurements observed throughout the monitoring period is also indicated.

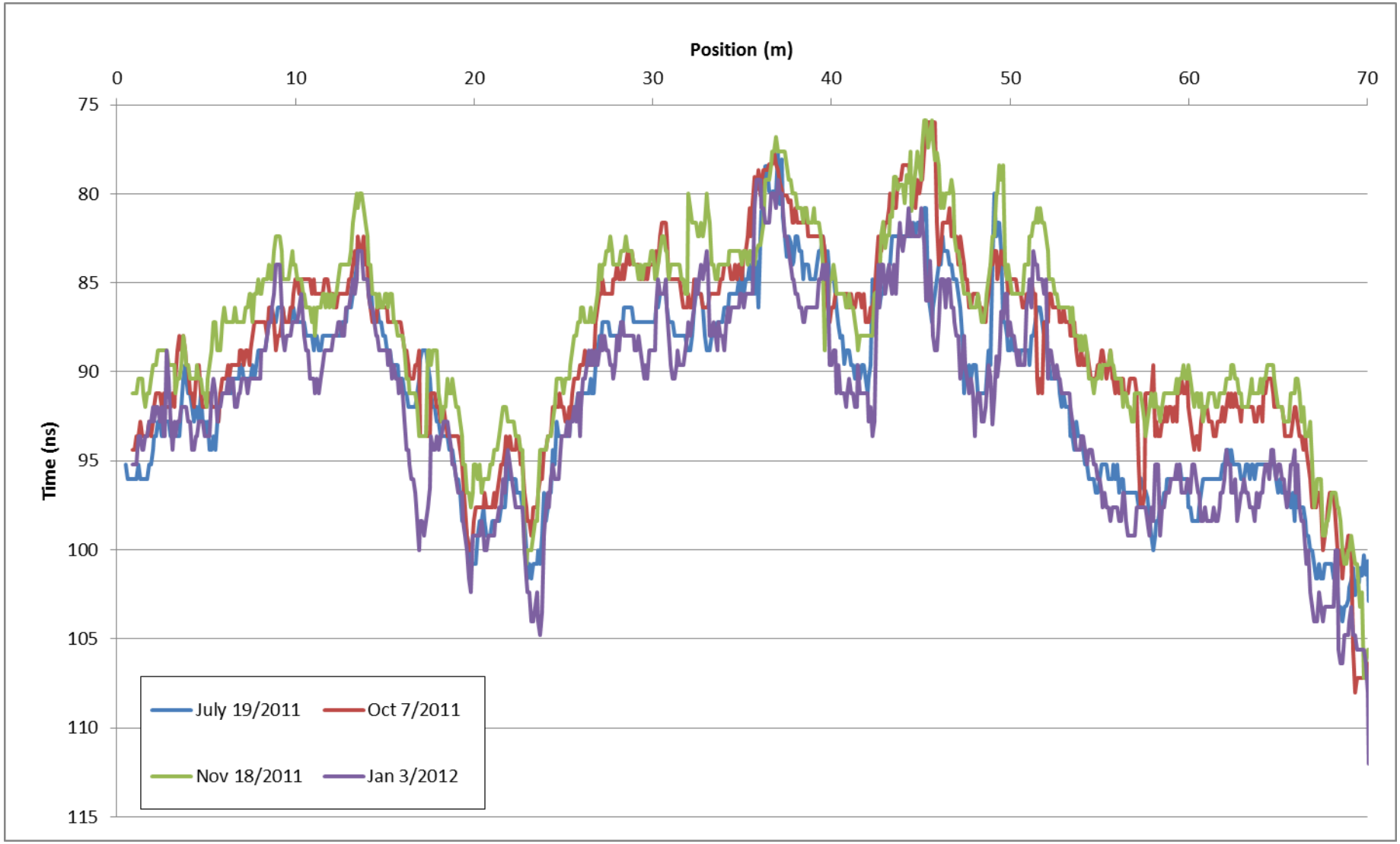

Figure 4.9 *part one*: The absolute two way travel time for the 200 MHz reflection profile data plotted with respect to position for July 19, 2011 through January 3, 2012. Referring to both Figures 4.9 part one and part two the earliest arrival time was seen on November 18, 2011 and the latest arrival time was seen on February 15, 2012.

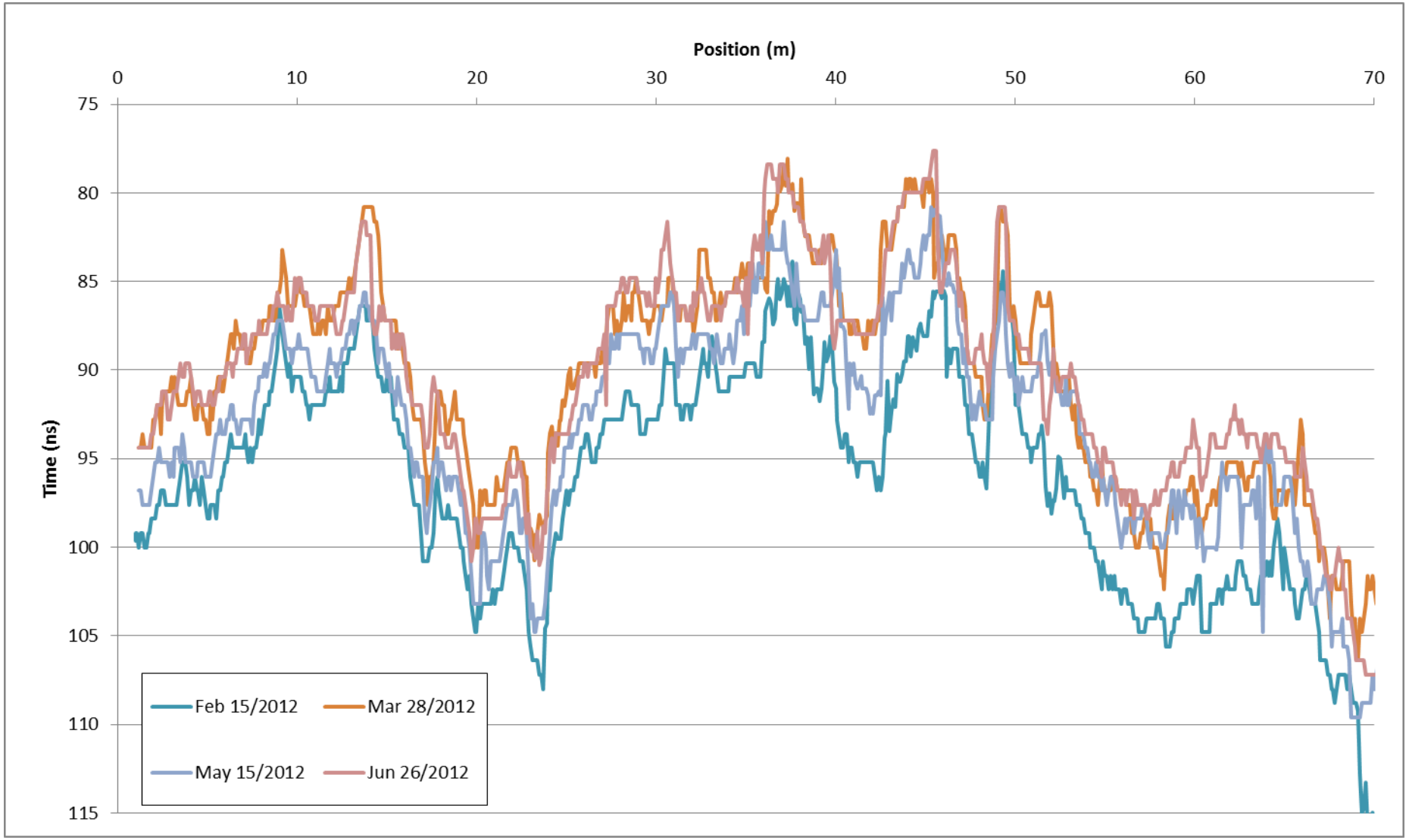

Figure 4.9 *part two*: The absolute two way travel time for the 200 MHz reflection profile data plotted with respect to position for February 15, 2012 through June 26, 2012. Referring to both Figures 4.9 part one and part two the earliest arrival time was seen on November 18, 2011 and the latest arrival time was seen on February 15, 2012.

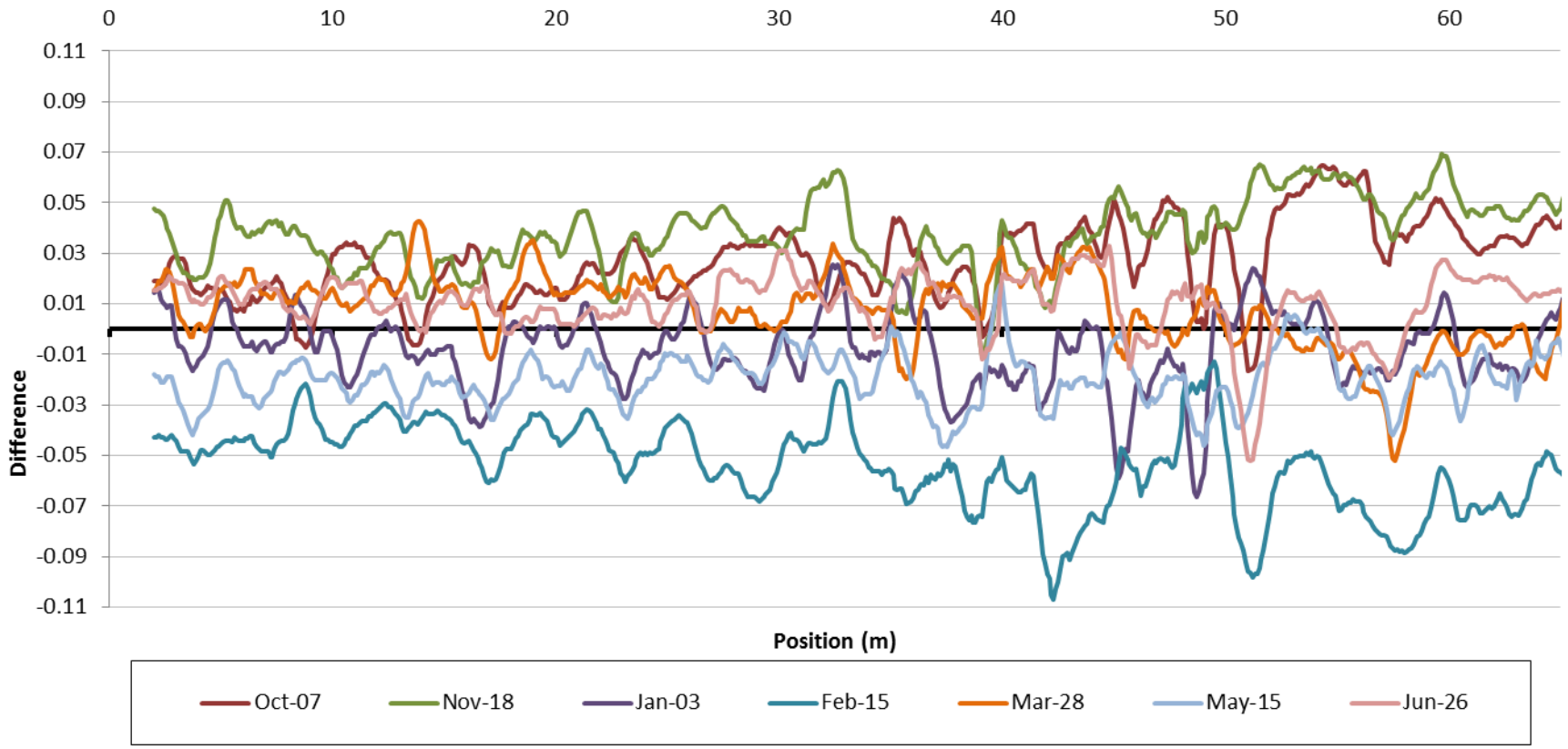

Figure 4.10: The relative difference between each 200 MHz reflection profile survey and the first survey on July 19, 2011 plotted as a function of position. A negative difference represents travel times that are less than those of the reference July 19, 2011 date.

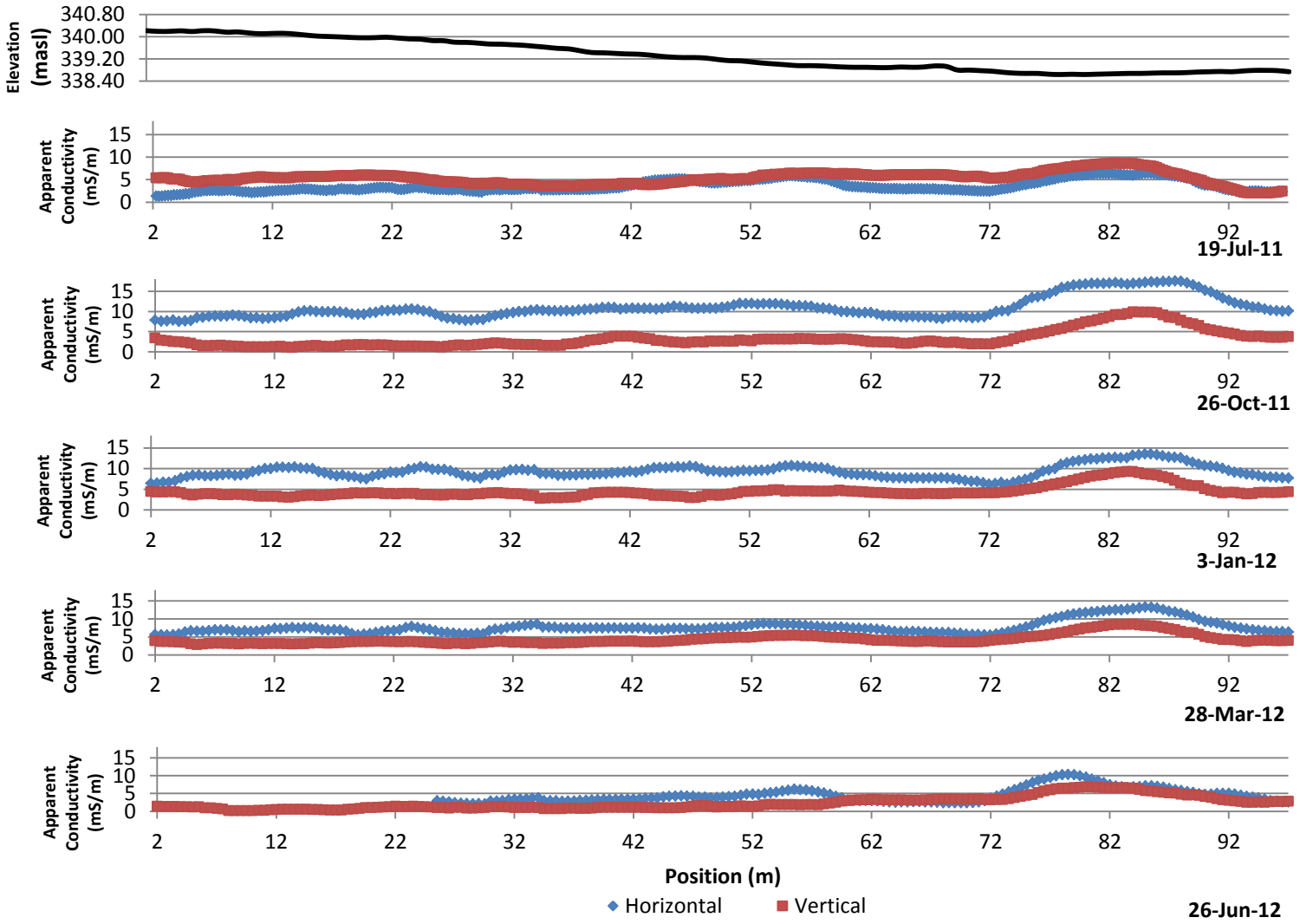

Figure 4.11: EM38 apparent conductivity profiles collected along the survey line for selected dates during the monitoring period to illustrate seasonal variations. The EM38 data collected in the horizontal and vertical dipole orientation are denoted as blue and red, respectively.

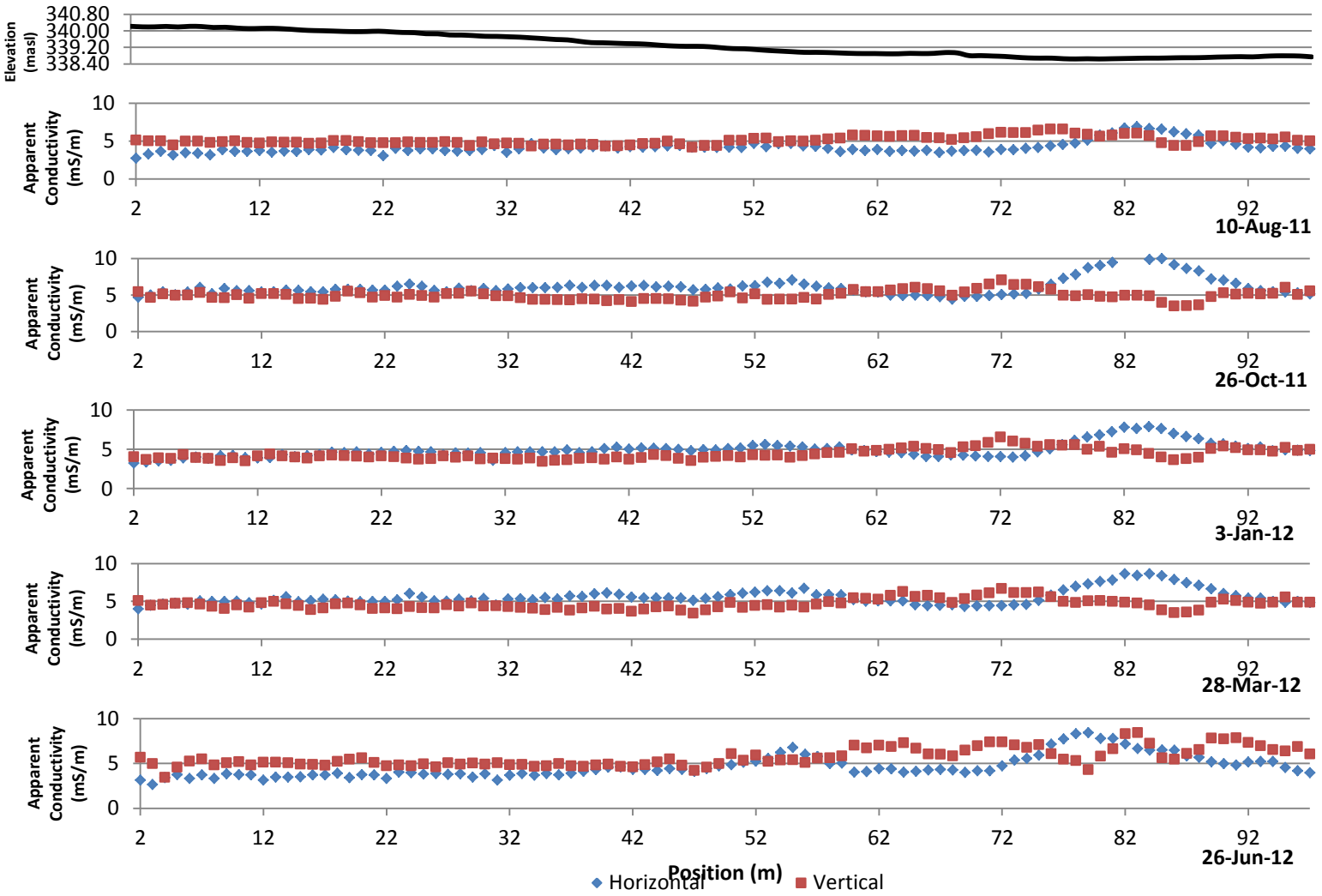

Figure 4.12: EM31 apparent conductivity profiles collected along the survey line for selected dates during the monitoring period to illustrate seasonal variations. The EM31 data collected in the horizontal and vertical dipole orientation are denoted as blue and red, respectively.

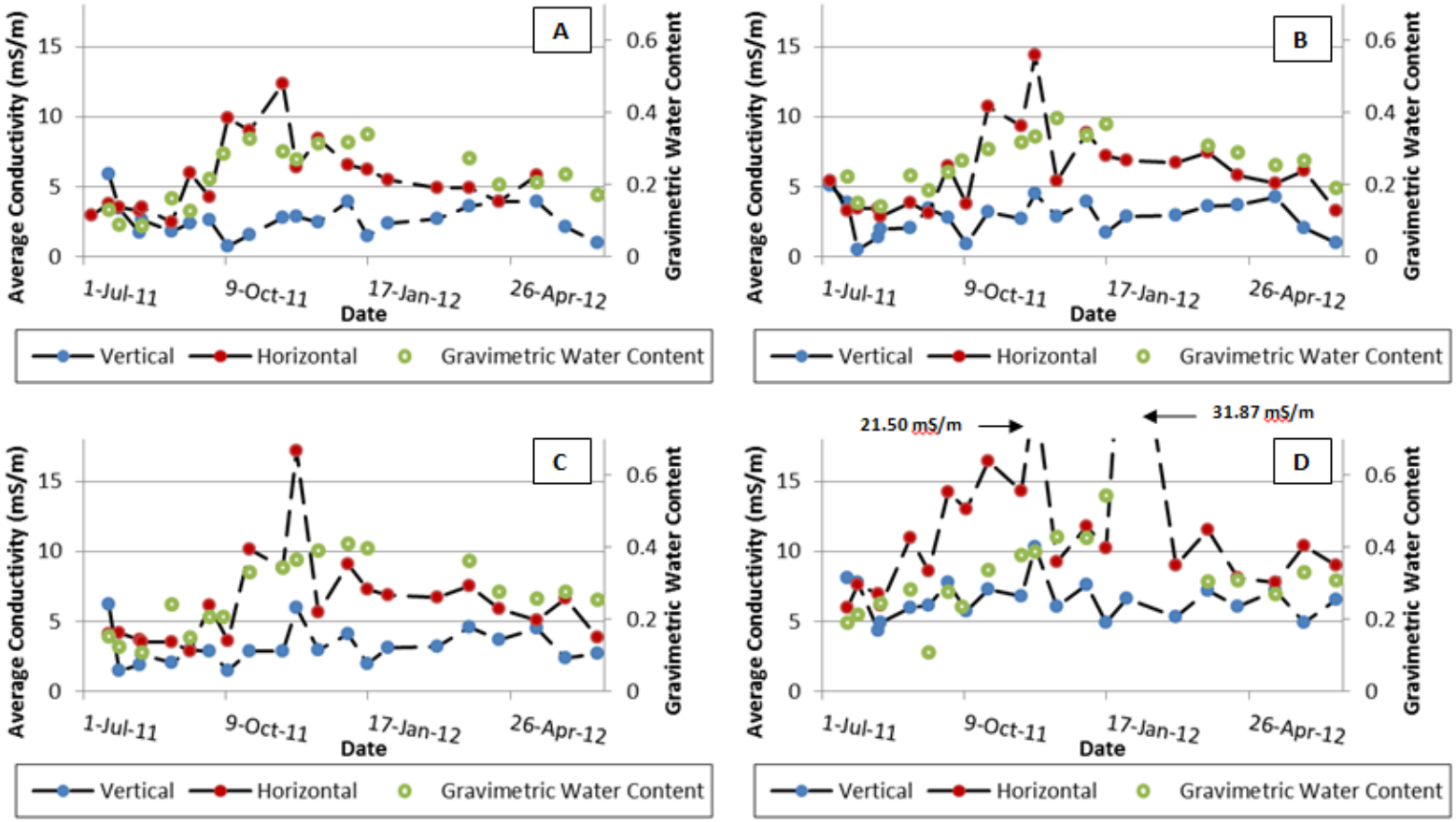

Figure 4.13: Time series of the EM38 apparent conductivities obtained in both the vertical and horizontal dipoles plotted with the corresponding gravimetric water contents derived from the gravimetric samples for stations (a) 20 m. (b) 40 m, (c) 60 m and (d) 80 m.

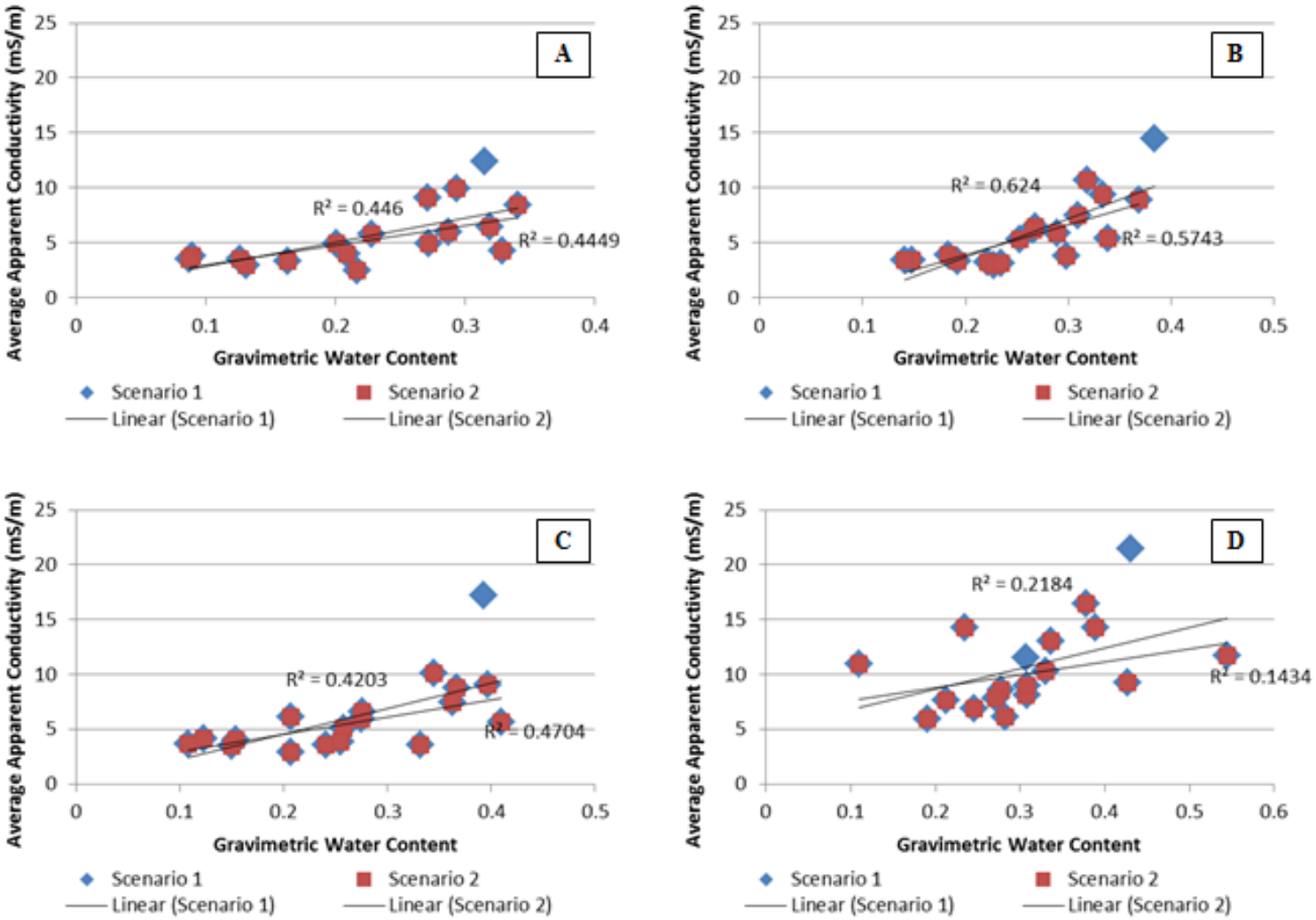

Figure 4.14: Analysis of the relationship between the EM38 apparent conductivities measured in both the vertical and horizontal dipoles and the gravimetric water contents for stations (a) 20 m, (b) 40 m, (c) 60 m and (d) 80 m. Scenario 1 includes all of the survey data and Scenario 2 excludes the November 28, 2011 outlier at all four locations as well as January 31, 2012 at the 80 m location.

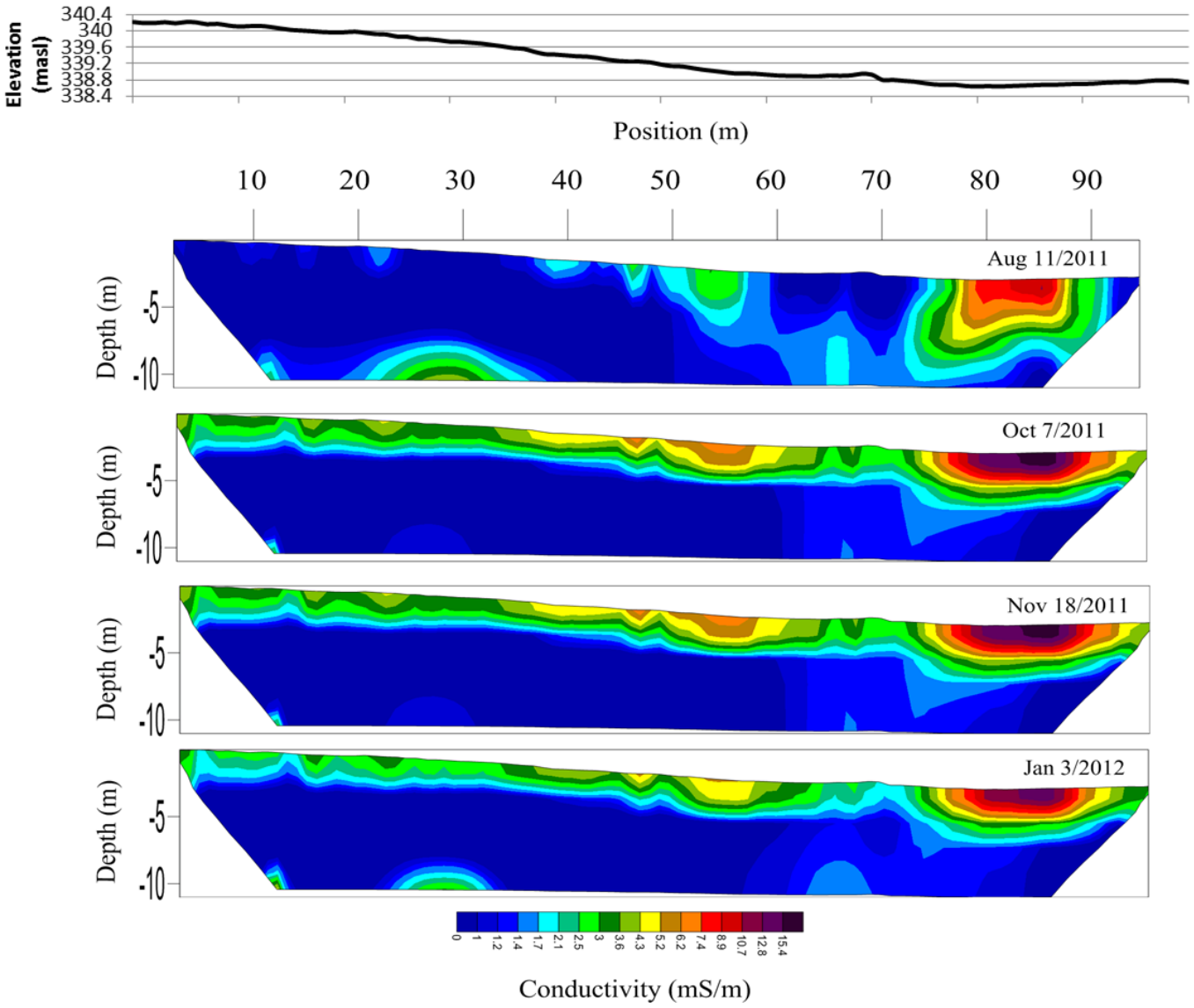

Figure 4.15 *part one*: Tomograms generated from the field scale ERT data covering the monitoring period to illustrate the seasonal variations in subsurface conductivity . The ERT data has been inverted and plotted with respect to conductivity on a log scale.

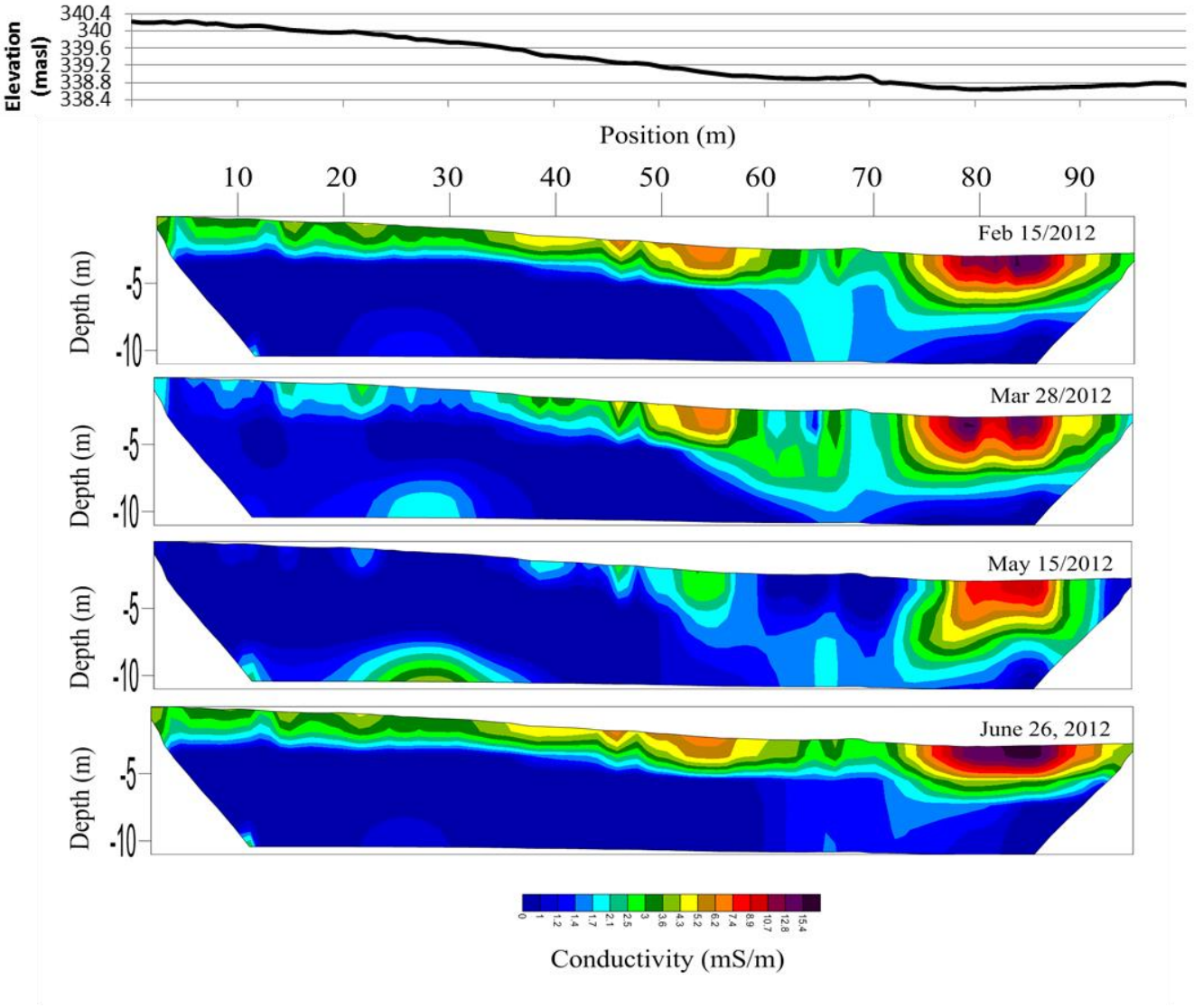

Figure 4.15 *part two*:T omograms generated from the field scale ERT data covering the monitoring period to illustrate the seasonal variations in subsurface conductivity . The ERT data has been inverted and plotted with respect to conductivity on a log scale.

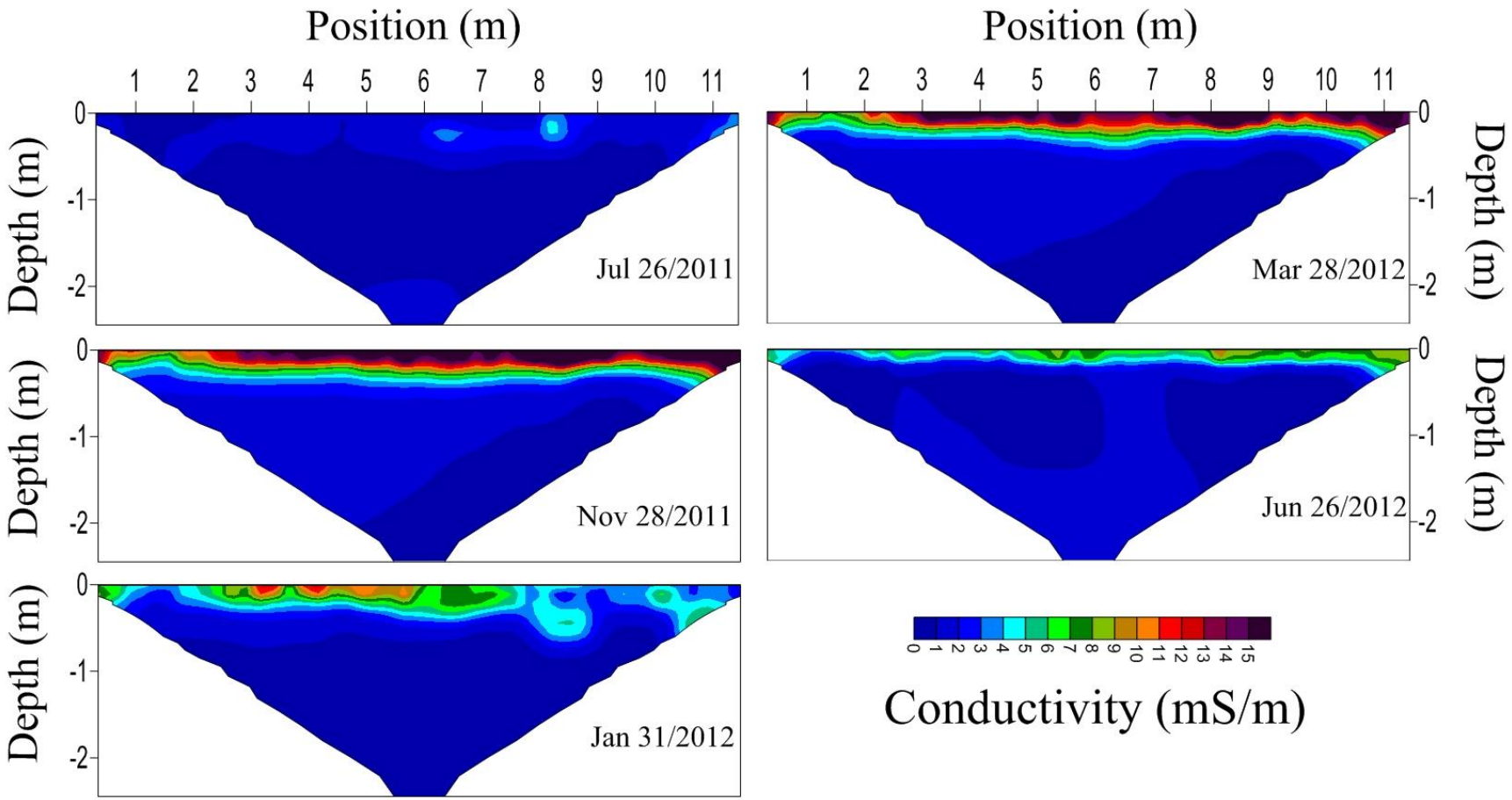

Figure 4.16: Tomograms obtained from the high resolution ERT data acquired at the 10 m station along the profile line for selected dates during the monitoring period. These tomograms are plotted using linear conductivity scale.

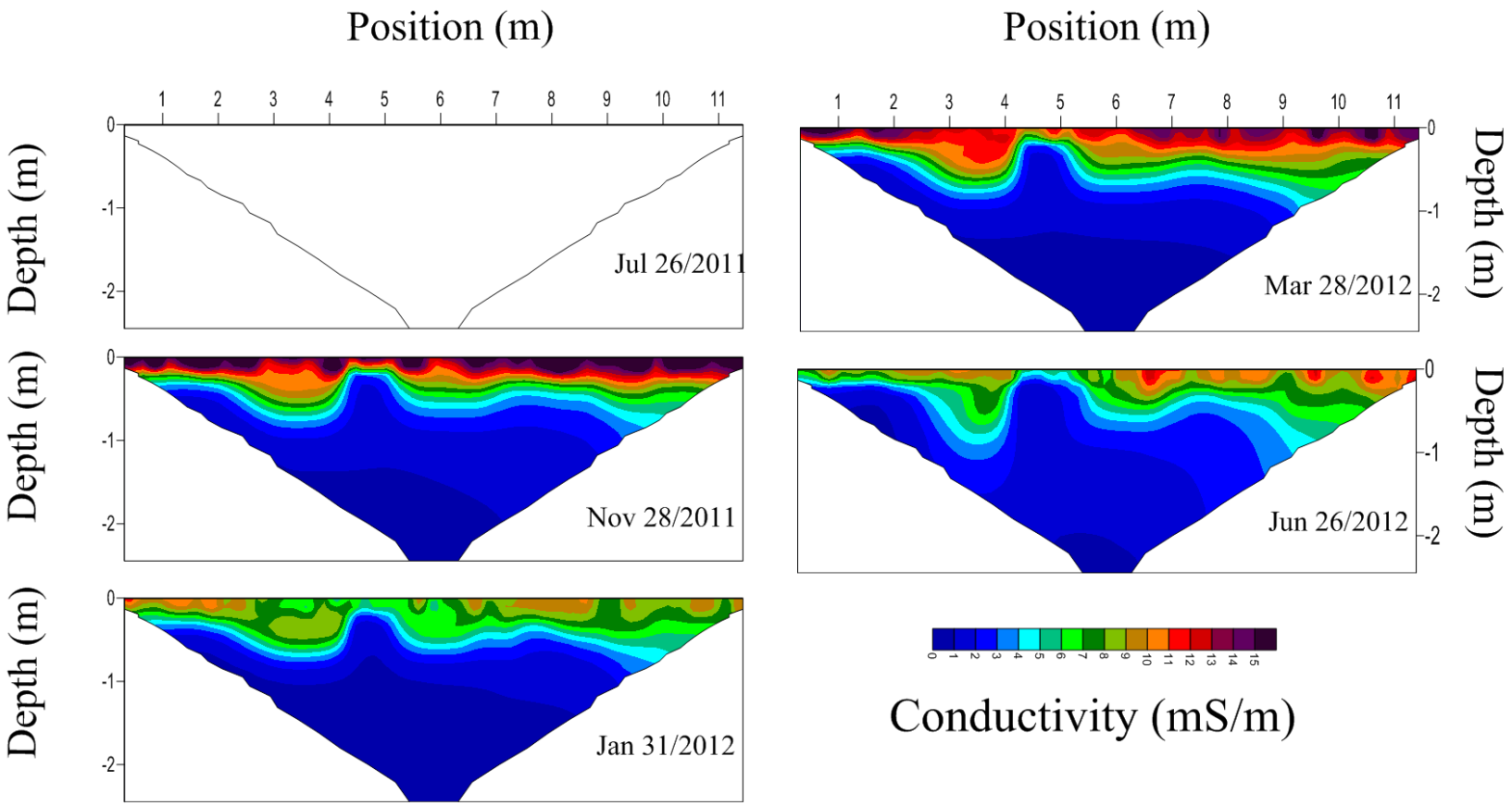

Figure 4.17: Tomograms obtained from the high resolution ERT data acquired at the 50 m station along the profile line for selected dates during the monitoring period. These tomograms are plotted using linear conductivity scale. Data was not acquired at this station on July 26 2011.

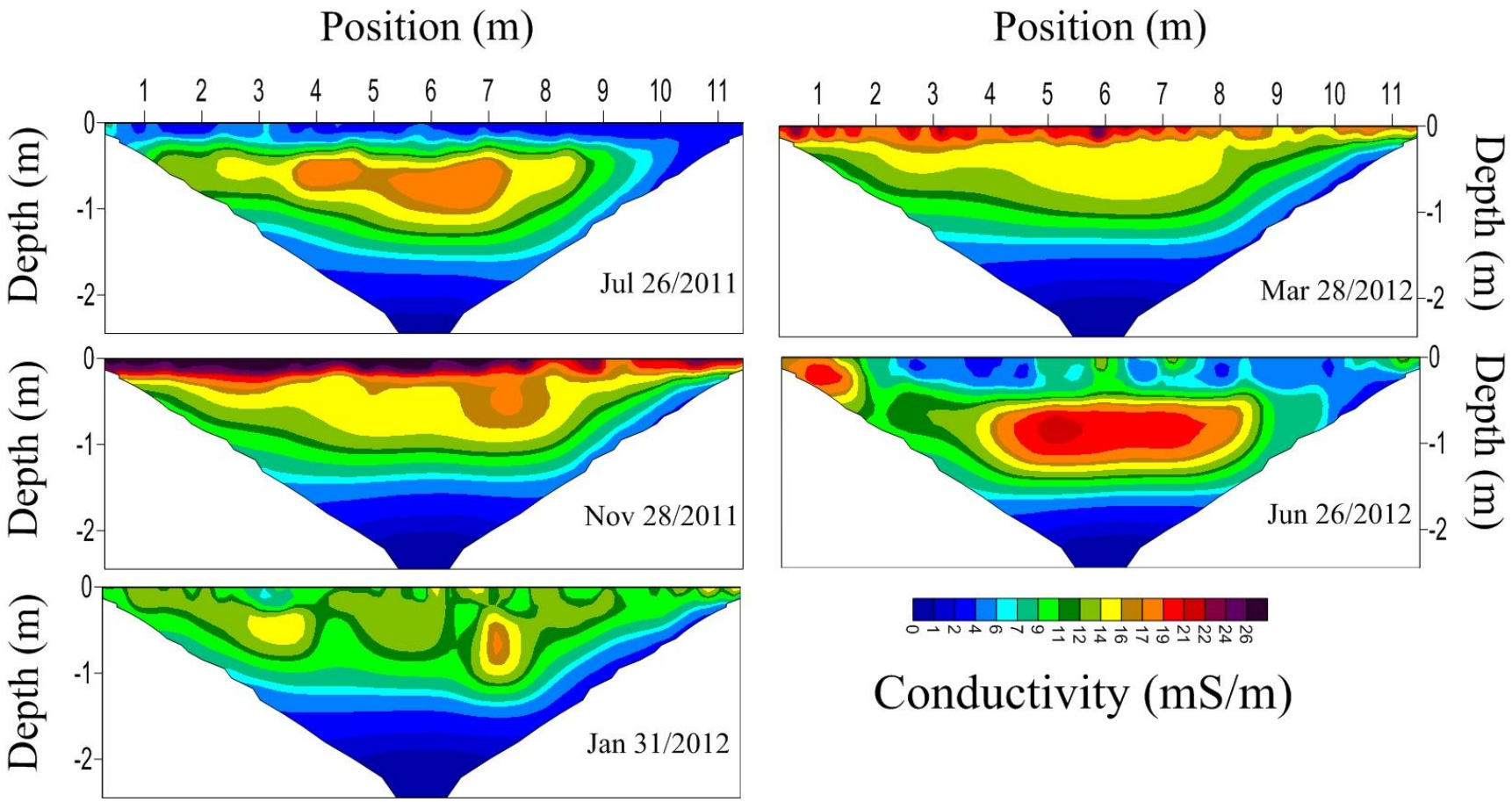

Figure 4.18: Tomograms obtained from the high resolution ERT data acquired at the 85 m station along the profile line for selected dates during the monitoring period. These tomograms are plotted using linear conductivity scale.

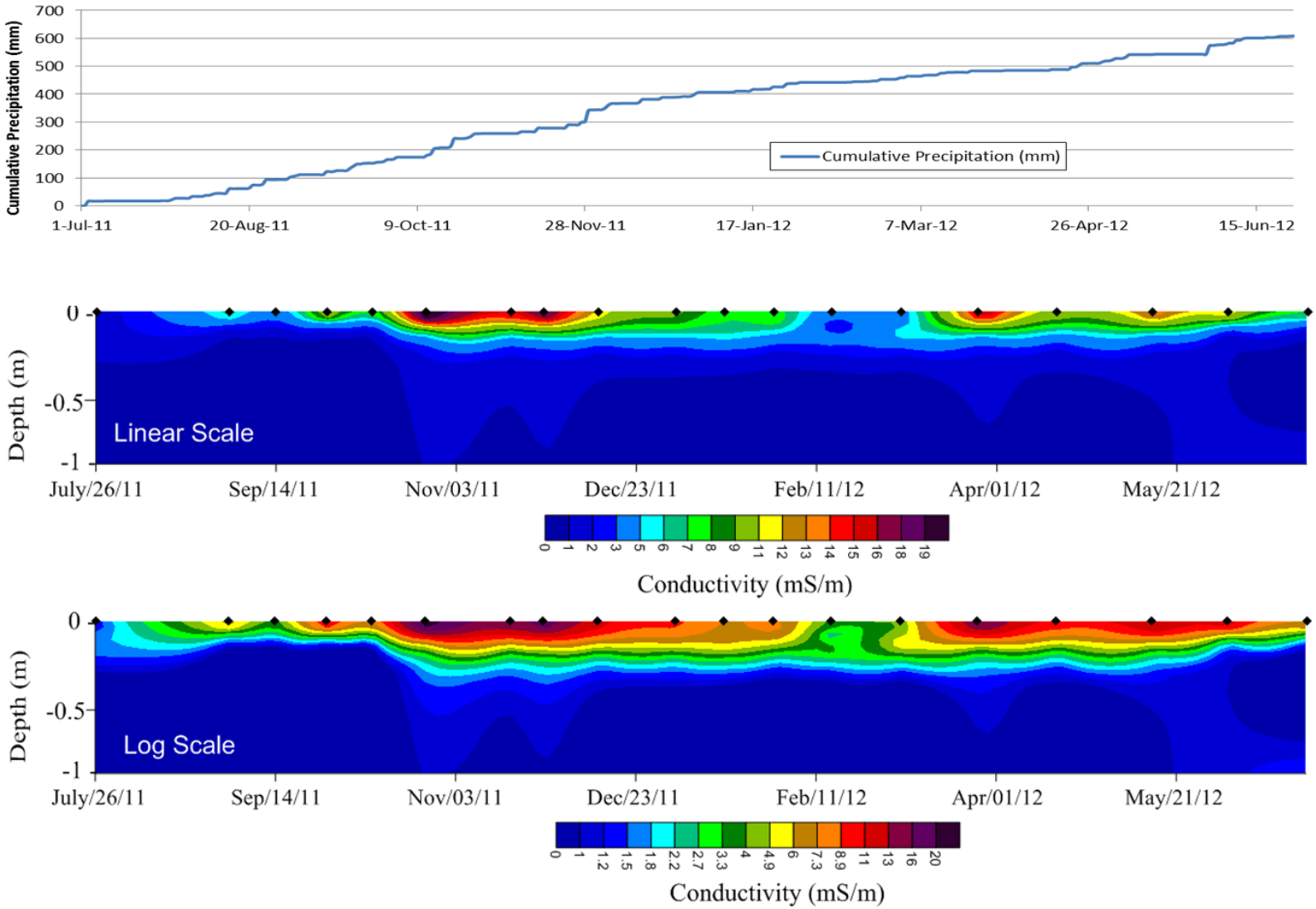

Figure 4.19: Mean conductivity depth profiles (lateral average from 4.00 to 8.00 m positions along the high resolution ERT profile line) presented as a time series for the complete monitoring period for the 10 m station. Results are presented as a linear plot (upper time series) and a log plot (lower time series).

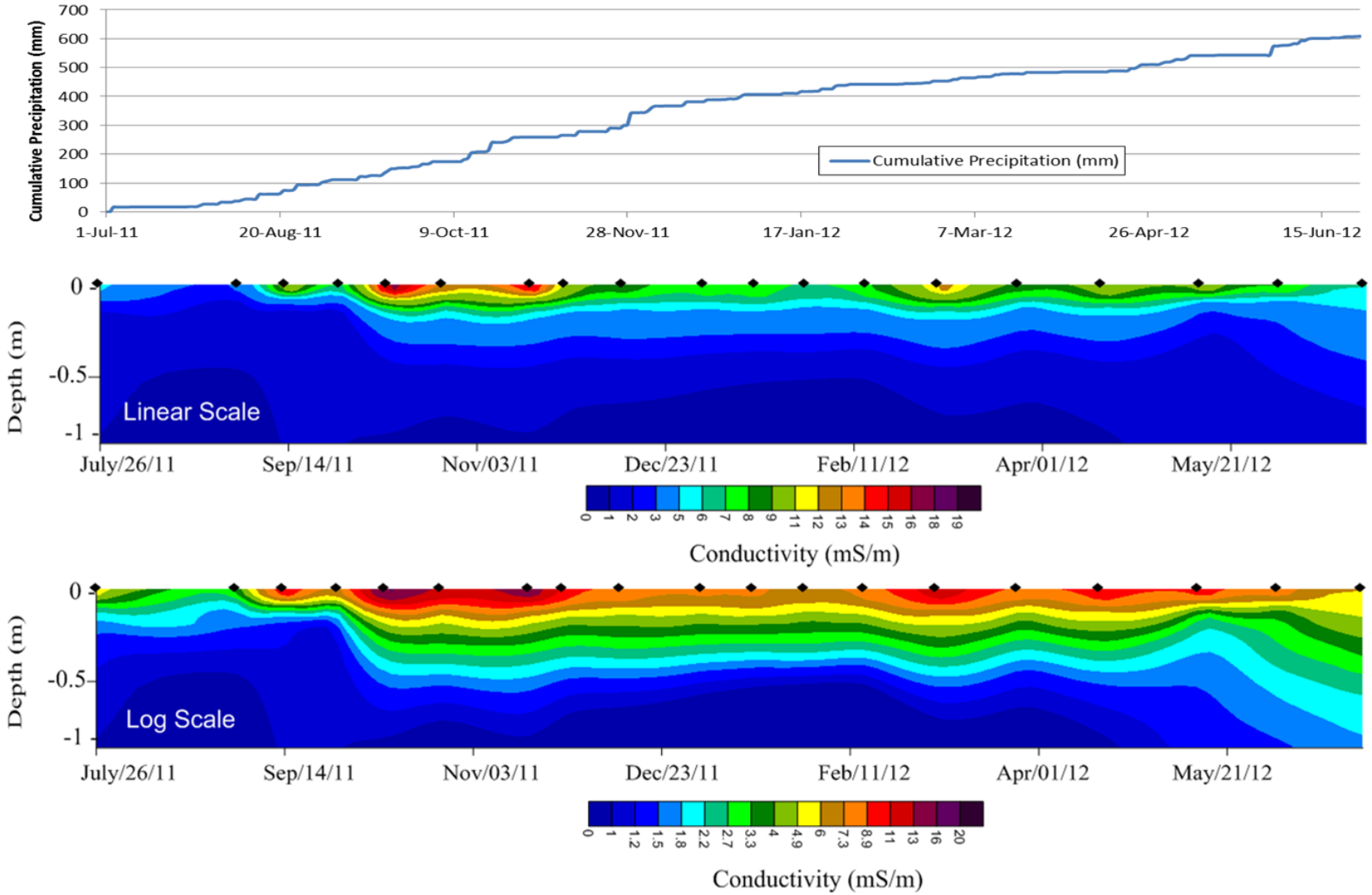

Figure 4.20: Mean conductivity depth profiles (lateral average from 4.00 to 8.00 m positions along the high resolution ERT profile line) presented as a time series for the complete monitoring period for the 50 m station. Results are presented as a linear plot (upper time series) and a log plot (lower time series).

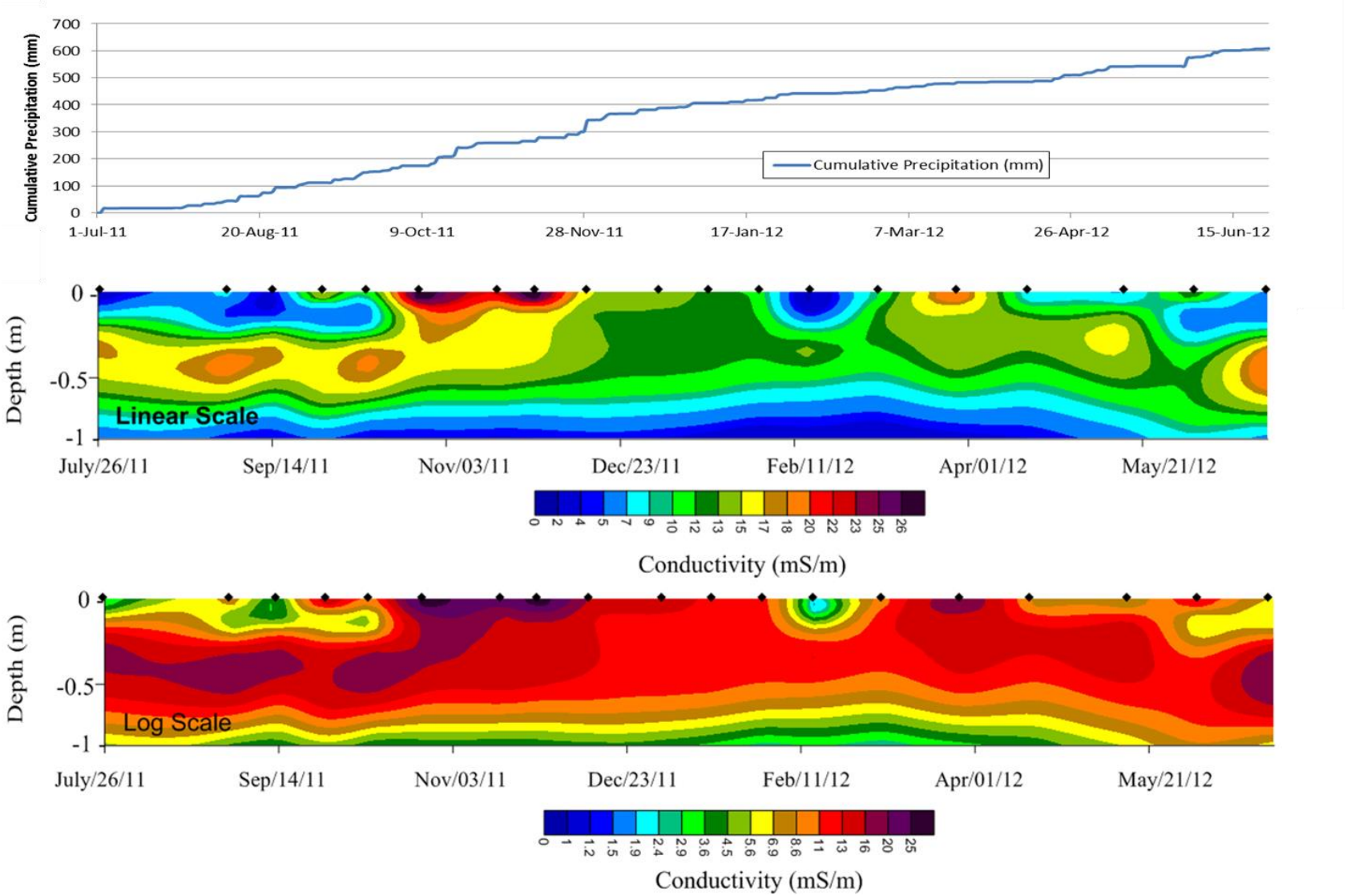

Figure 4.21: Mean conductivity depth profiles (lateral average from 4.00 to 8.00 m positions along the high resolution ERT profile line) presented as a time series for the complete monitoring period for the 85 m station. Results are presented as a linear plot (upper time series) and a log plot (lower time series).

5.0 Conclusions

The objective of this study is to add to our current knowledge and guide research into the potential of GPR, EMI and ERT geophysical methods to provide information about the near surface soil moisture dynamics in a coarse grained soils. The results show that there is potential for the three geophysical methods (GPR, EMI and ERT) to provide insight into the near surface soil moisture dynamics in a coarse stony grained soil. The evidence for this capacity seen at the ARS are as follows:

1) The GPR data was able to show temporal and spatial variations in both the NMO and DGW velocities (Figures 4.2 and 4.5, respectively) as well as the two-way travel times seen in the reflection data (Figure 4.9).

2) The EMI data showed a qualitative relationship between the EM38 apparent conductivities and the gravimetric water contents (Figure 4.13).

3) The both the field scale and high resolution ERT surveys were able to illustrate seasonal and spatial variations in conductivity (Figure 4.15 and Figure 4.19 to 4.21, respectively).

This study is unique in that the geophysical studies were carried out in highly heterogeneous coarse grained soils compared to the sandy soils in which previous studies had been conducted.

Utilizing various configurations and orientations, all three geophysical methods were able to characterize the seasonal trends such as wetting in the spring and fall, drying in the summer and freezing in the winter. The depression seen around 80 m on the survey line was also identified with all three geophysical methods. The geophysical responses followed similar trends as the gravimetric water contents throughout the year and across the survey line. However, when the relationships were evaluated quantitatively the correlation was significantly weaker than expected. The difference in effective sampling volumes between the geophysical methods and

the gravimetric samples could account for the weak correlations. The gravimetric moisture contents represent a very small volume of the material, whereas the geophysical responses encompass a much large volume of the material. With the highly heterogeneous nature of the outwash materials a more representative sampling volume would need to be taken in order to more accurately compare the gravimetric water contents and geophysical responses. This is consistent with Coppola et al. (2013) where it was identified that the presence of stones makes it very difficult to quantify the overall soil moisture content due to the extreme heterogeneity attributed with stony materials.

The various orientations and configurations also allowed for geophysical responses to identify geological boundaries and changes in soil moisture with depth. The three geophysical methods consistently identified that the geophysical responses measured in the very near surface fluctuated significantly more than those measured in the deeper subsurface. With the GPR reflection profile and the ERT profiles geological boundaries were also identified (Figures 4.7 and 4.15, respectively).

The GPR and EMI methods had some data quality issues at this site. With the GPR instrument, the data quality and depth of penetration of the signal decreased down the survey line as a result of increase electrical conductivities in the near surface materials and the EM38 experienced a significant amount of drift throughout the survey which required correction.

The results in this thesis clearly demonstrate the capacity of the three geophysical methods (GPR, EMI and ERT) to characterize the vadose zone in a highly heterogeneous coarse grained soil. However, it is also apparent that further work is required in order to quantitatively compare the geophysical responses with auxiliary measurements such as deeper test pits and/or gravimetric water contents from a more representative sampling volume. Future work in similar

coarse grained soils could improve the understanding of the abilities of these geophysical methods and approaches.

6.0 References

Akbar, M.A., Kenimer, A.L., Searcy, S.W. and Torbert, H.A., 2005. Soil water estimating using electromagnetic induction. Transactions of the American Society of Agricultural Engineers, 48(1), 129-135.

Amidu, S.A. and Dunbar, J.A., 2007. Geoelectric studies of seasonal wetting and drying of a Texas vertisol. Vadose Zone Journal, 6(3), 511-523.

Annan, A.P., 2005. Chapter 11: Ground penetrating radar, *in* Butler D.K. (editor), Near-surface geophysics. Society of Exploration Geophysicists, Tulsa, OK., 357 – 438.

Celano, G., Palese, A.M., Ciucci, A., Martorella, E., Vignozzi, N. and Xiloyannis, C., 2011. Evaluation of soil water content in tilled and crop-covered olive orchards by the geoelectrical technique. Geoderma, 163, 163-170.

Cole, J., Coniglio, M. and Gautrey, S., 2009. The role of buried bedrock valleys on the development of karstic aquifers in flat-lying carbonate bedrock: insights from Guelph, Ontario, Canada. Hydrogeology Journal, 17, 1411-1425.

Coppola, A., Dragonetti, G., Comegna, A., Lamaddalena, N., Caushi, B., Haikal, M.A. and Basile, A., 2013. Measuring and modeling water content in stony soils. Soil and Tillage Research, 128, 9-22.

Fitterman, D.V. and Labson, V.F., 2005. Chapter 10: Electromagnetic Induction Methods for Environmental Problems, *in* Butler D.K. (editor), Near-surface geophysics. Society of Exploration Geophysicists, Tulsa, OK., 301 – 356.

Frohlich, R.K. and Parke, C.D., 1989. The electrical resistivity of the vadose zone: Field survey. Groundwater 27, 524-530.

Geonics Limited EM38 Operating Manual. http://www.olemiss.edu/research/anthropology/haley/class2010/library/EM38B%20Manual%20(Nov03).PDF. Geonics Limited, #8, 1745 Meyerside Dr., Mississauga, ON., L5T 1C6.

Johnson, M.D. and Gillam, ML., 1995. Composition and construction of late Pleistocene end moraines, Durango, Colorado. Geological Society of America Bulletin, 107(10), 1241-1253.

Kunert, M. and Coniglio, M., 2002. Origin of vertical shafts in bedrock along the Eramosa river valley near Guelph, southern Ontario. Canadian Journal of Earth Science, 39, 43-52.

Luck, E., Ruehlmann, J. and Kirchmann, H., 2011. Properties of soils from the Swedish long-term fertility experiments: VI. Mapping soil electrical conductivity with different geophysical methods. Acta Agricultural Scandinavia Section B- Soil and Plant Science, 61, 438-447.

McNeil, J.D., 1980. Electromagnetic terrain conductivity measurement at low induction

numbers. Technical Note TN-6. Geonics Ltd, Mississauga, Ontario.

Pellicer, X.M., Zarroca, M. and Gibson, P., 2012. Time-lapse resistivity analysis of Quaternary sediments in the Midlands of Ireland. Journal of Applied Geophysics, 82, 4-58.

Reedy, R.C. and Scanlon, B.R., 2003. Soil Water Content Monitoring using Electromagnetic induction. Journal of Geotechnical and Geoenvironmental Engineering, 129(11), 1028-1039.

Sadura, S., Martini, I.P., Endres, A.L. and Wolf, K., 2006. Morphology and GPR stratigraphy of a frontal part of an end moraine of the Laurentide ice sheet: Paris moraine near Guelph, ON, Canada. Geomorphology, 75, 212-225.

Sheets, K.R. and Hendrickx, J.M.H., 1995. Noninvasive soil water content measurement using electromagnetic induction. Water Resources Research, 31(10), 2401-2409.

Steelman, C.M. and Endres, A.L., 2010. An examination of direct ground wave soil moisture monitoring over an annual cycle of soil conditions. Water Resources Research, 46, W11533, doi: 10.1029/2009WR008815.

Steelman, C.M. and Endres, A.L., 2011. Comparison of petrophysical relationships for soil moisture estimation using GPR ground waves. Vadose Zone Journal, 10, 270-285.

Steelman, C.M. and Endres, A.L., 2012. Assessing vertical soil moisture dynamics using multi-frequency GPR common-midpoint soundings. Journal of Hydrology, 436-347.

Topp, G.C., Davis, J.L. and Annan, A.P., 1980. Electromagnetic determination of soil water content: Measurements in coaxial transmission lines. Water Resource Reseach, 16, 574-582.

Zhou, Q.Y., Shimada, J. and Sato, A., 2001. Three-dimensional spatial and temporal monitoring of soil water content using electrical resistivity tomography. Water Resource Research, 37, 273-285.

Appendix A

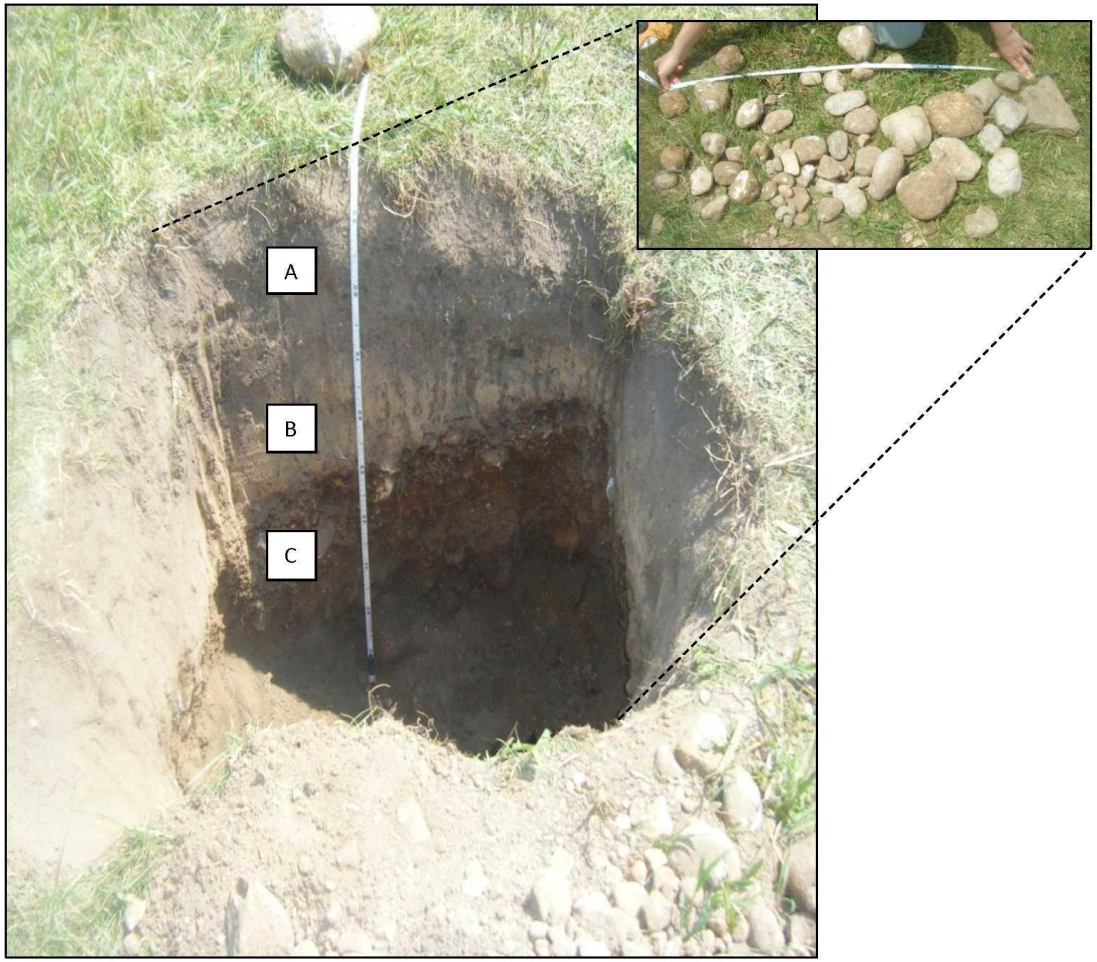

Figure A-1: Picture of the trench dug at the 10m location; A, B and C represent the three different soil horizons that were sampled.

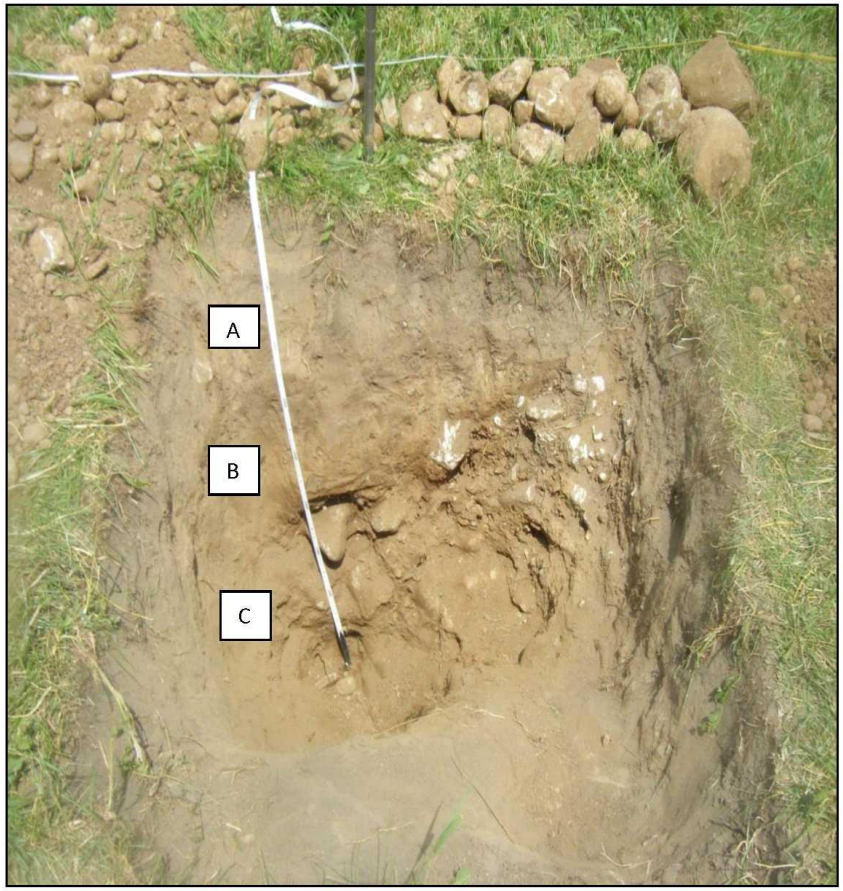

Figure A-2: Picture of the trench dug at the 50 m location; A, B and C represent the three different soil horizons that were sampled.

Figure A-3: Picture of the trench dug at the 85 m location; A, B and C represent the three different soil horizons that were sampled.

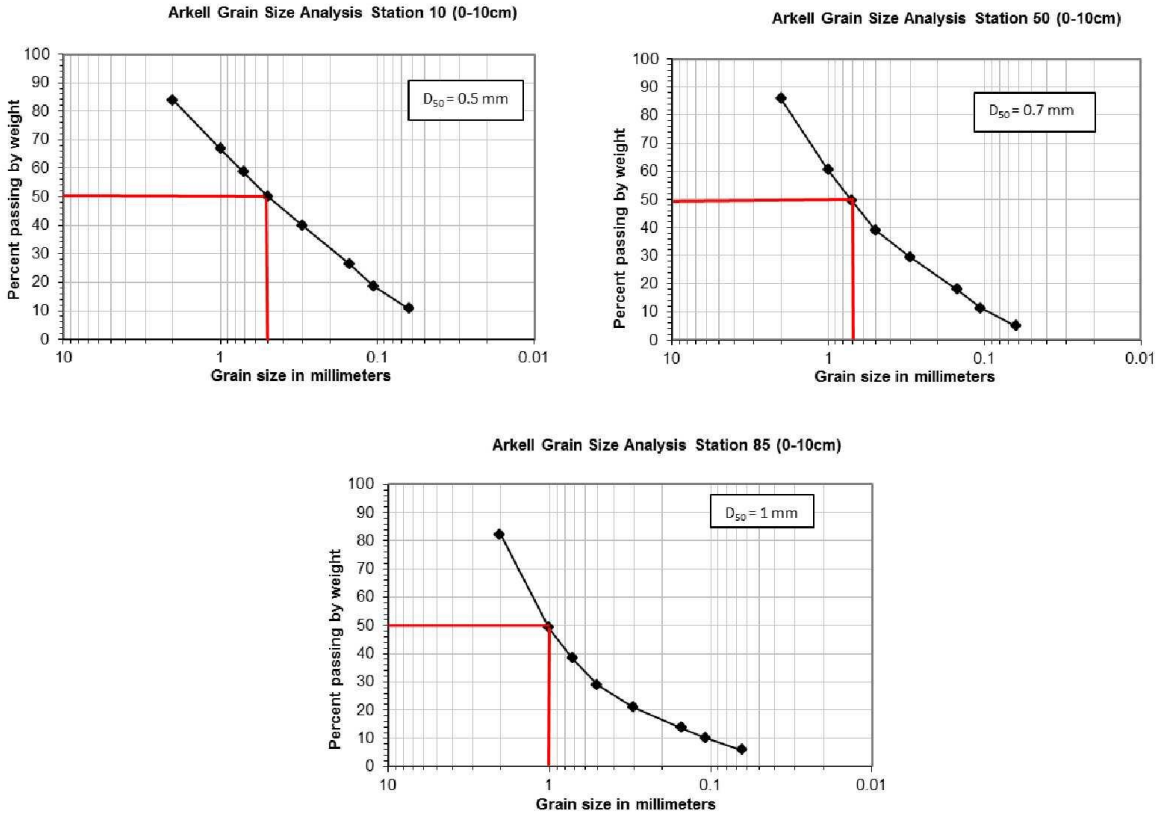

Figure A-4a: Grain size distribution curves (GSD) for the depth interval 0-10 cm at gravimetric locations 10, 50 and 85 m. The red line indicates the mass-median particle size (D_{50}).

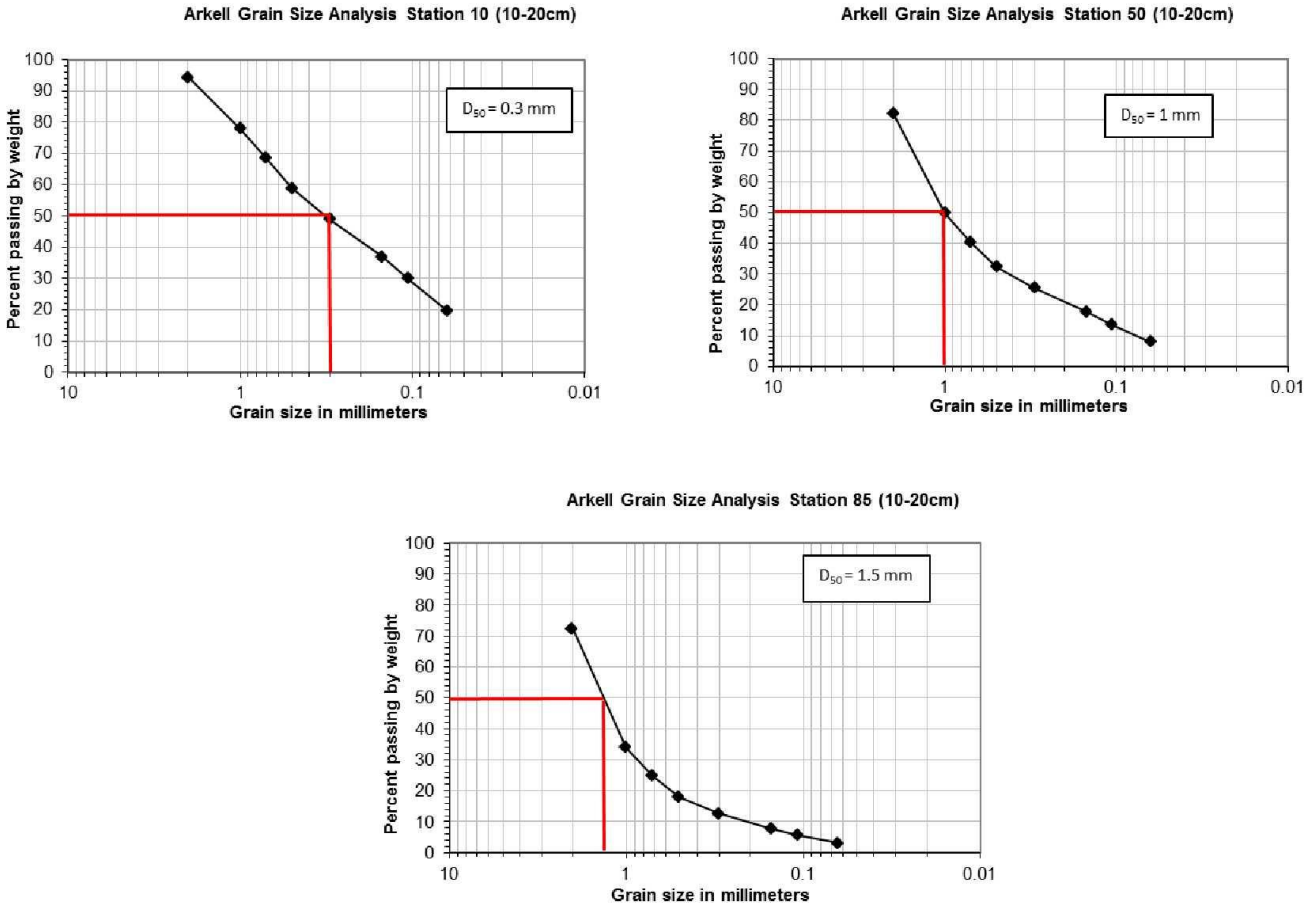

Figure A-4b: Grain size distribution curves (GSD) for the depth interval 10-20 cm at gravimetric locations 10, 50 and 85 m. The red line indicates the mass-median particle size (D_{50}).

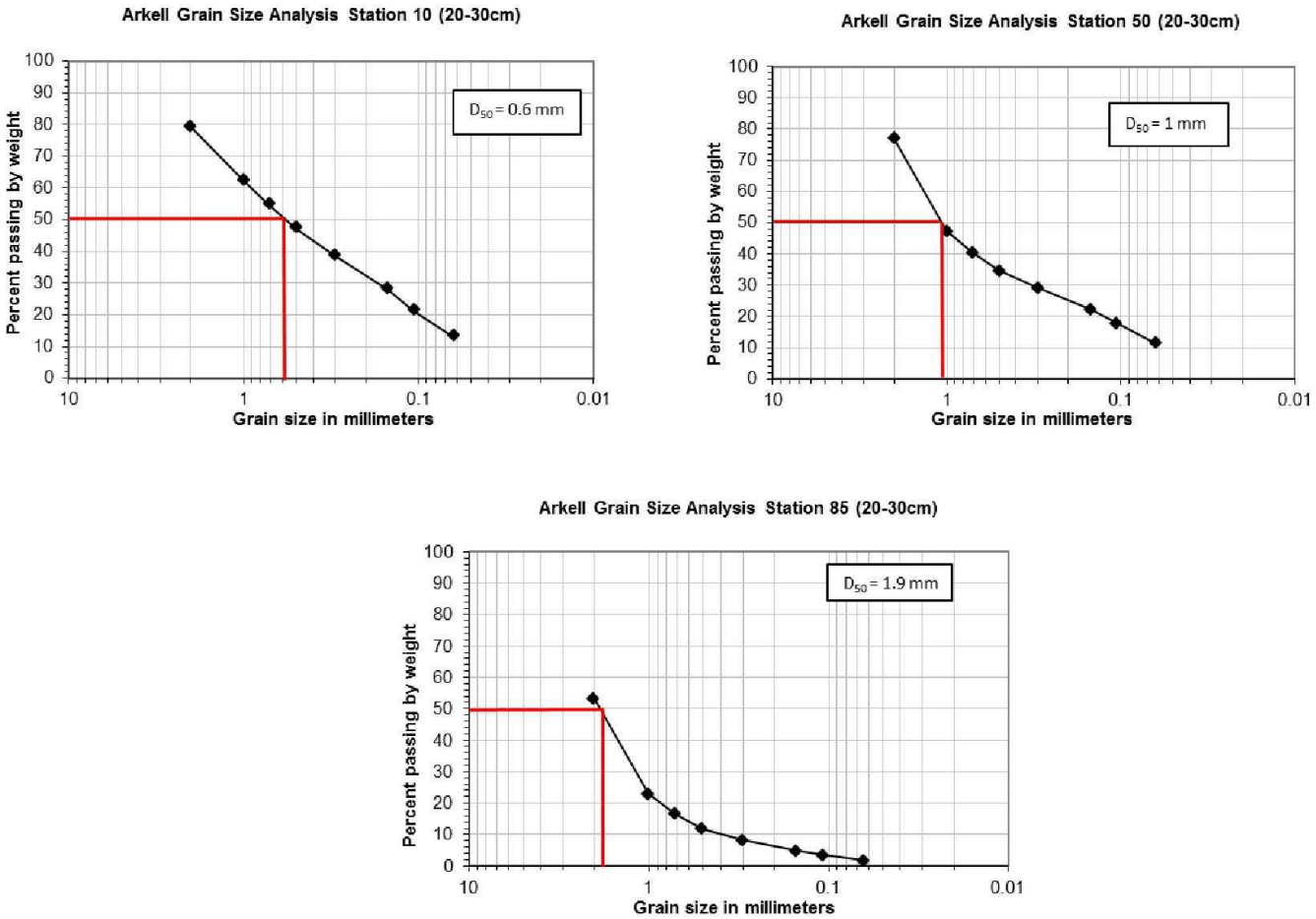

Figure A-4c: Grain size distribution curves (GSD) for the depth interval 20-30 cm at gravimetric locations 10, 50 and 85 m. The red line indicates the mass-median particle size (D_{50}).

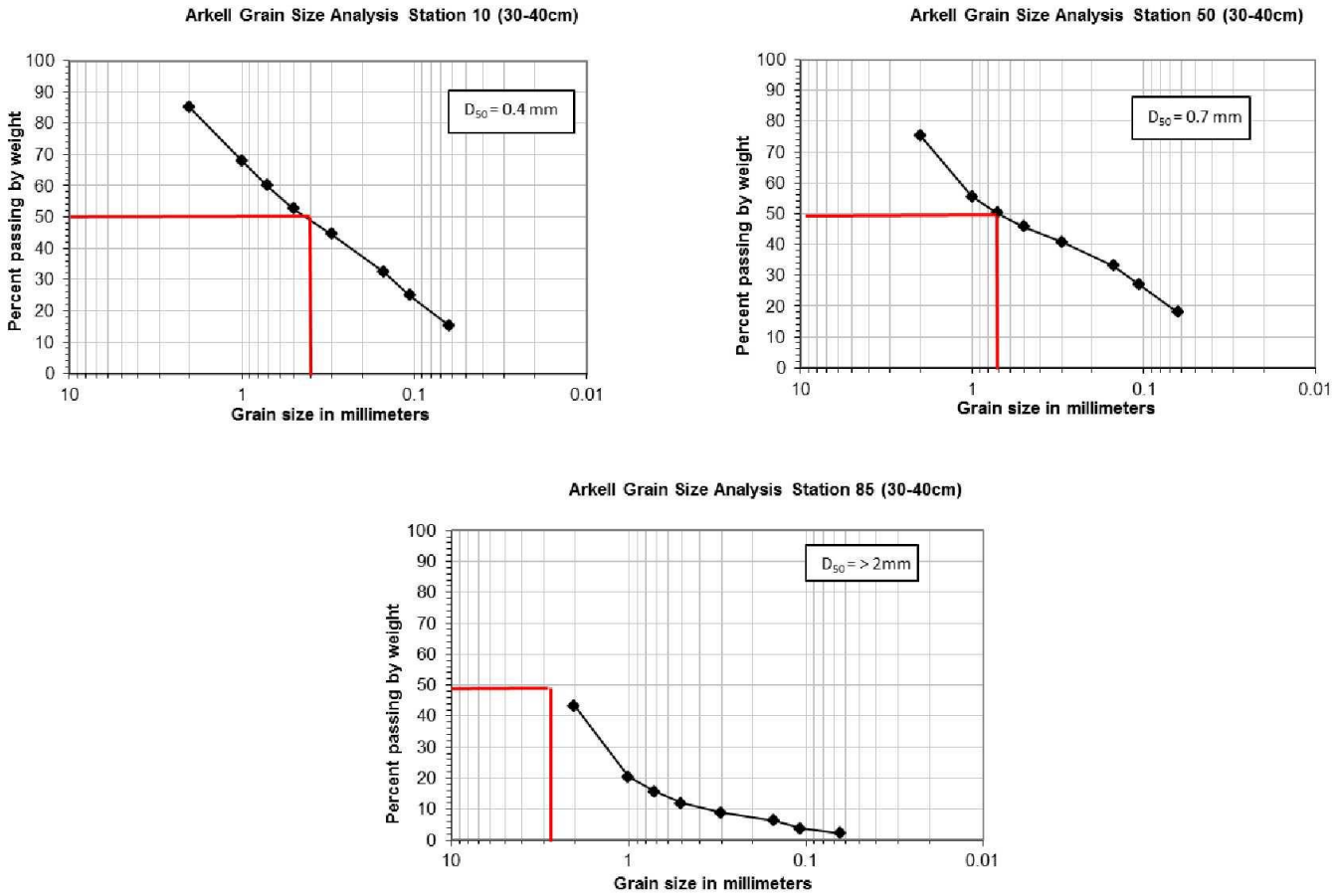

Figure A-4d: Grain size distribution curves (GSD) for the depth interval 30-40 cm at gravimetric locations 10, 50 and 85 m. The red line indicates the mass-median particle size (D_{50}).

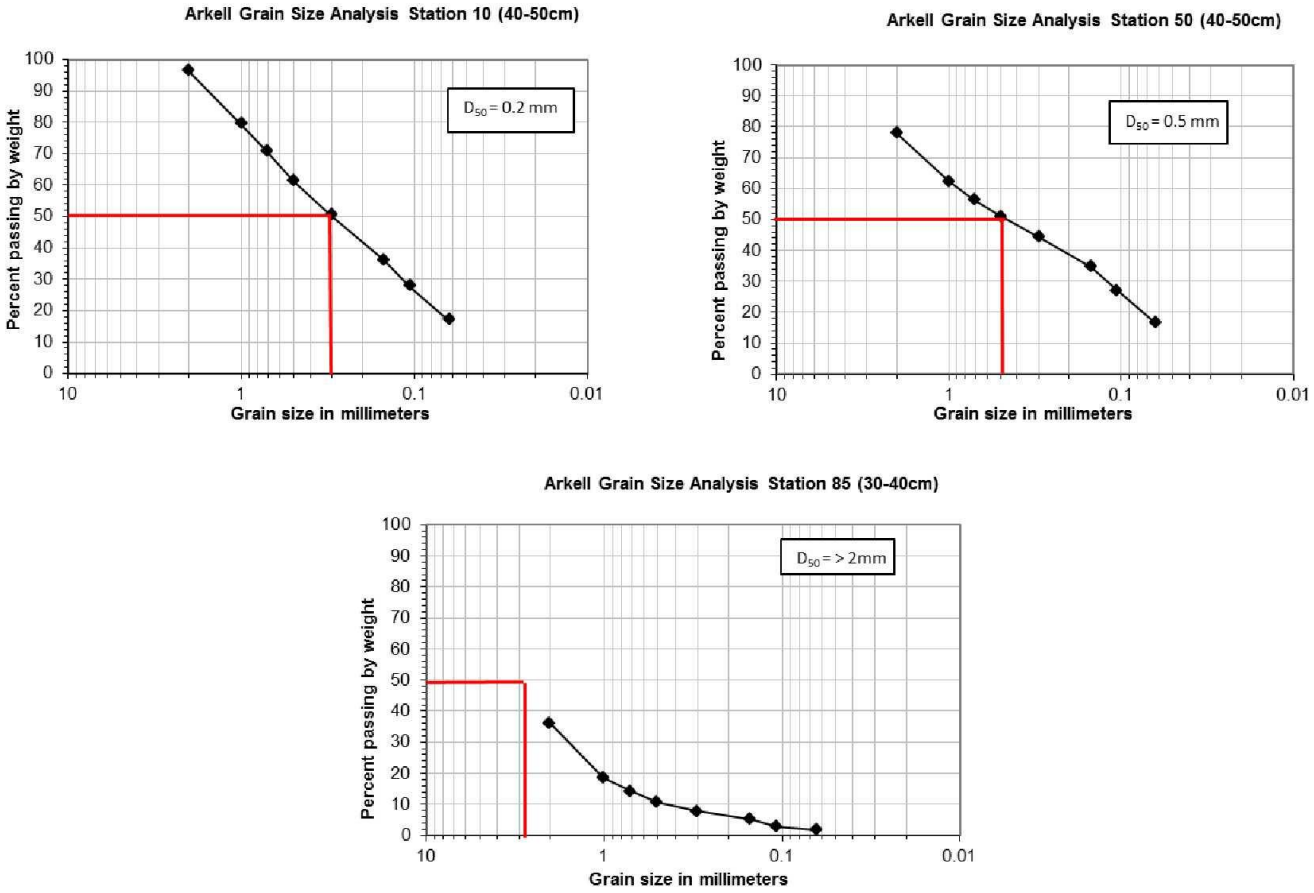

Figure A-4e: Grain size distribution curves (GSD) for the depth interval 40-50 cm at gravimetric locations 10, 50 and 85 m. The red line indicates the mass-median particle size (D_{50}).

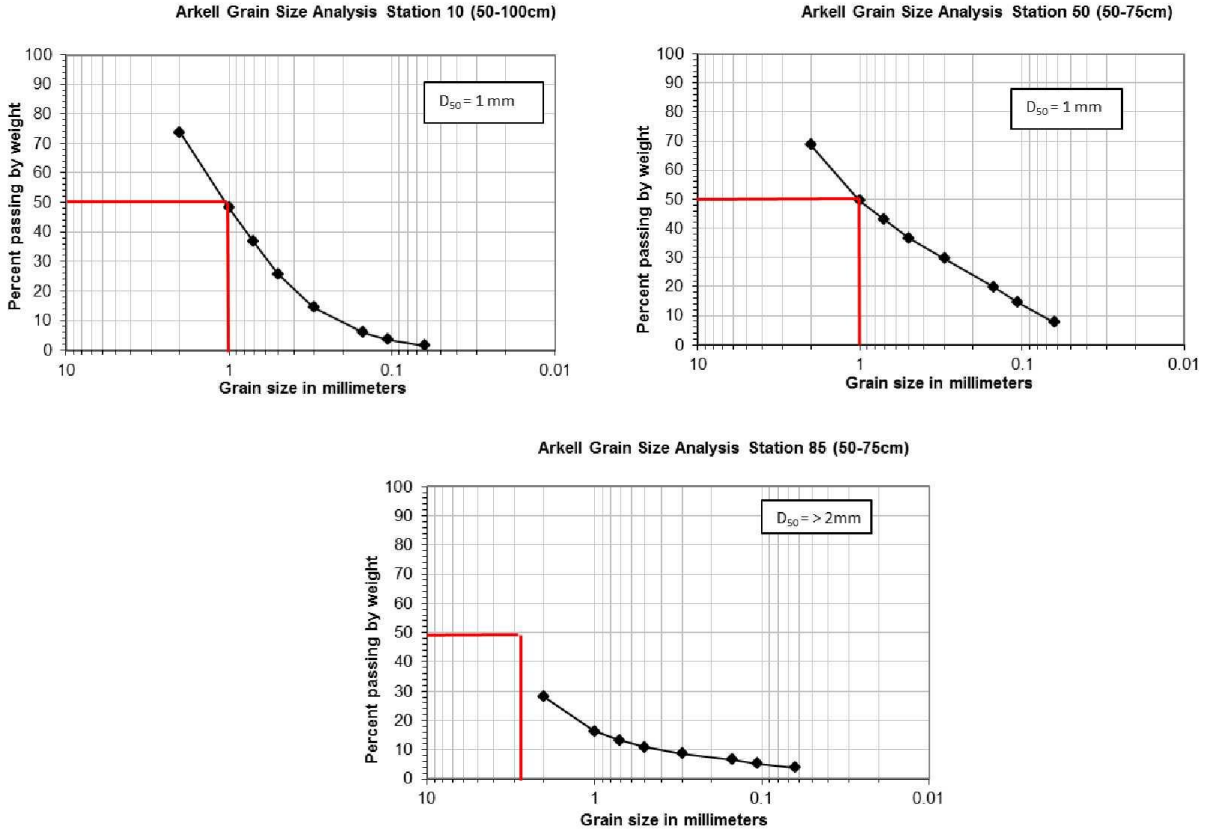

Figure A-4e: Grain size distribution curves (GSD) for the depth interval 50-100 cm and 50-75 cm at gravimetric locations 10 and, 50 and 85 m, respectively. The red line indicates the mass-median particle size (D_{50}).

Appendix B

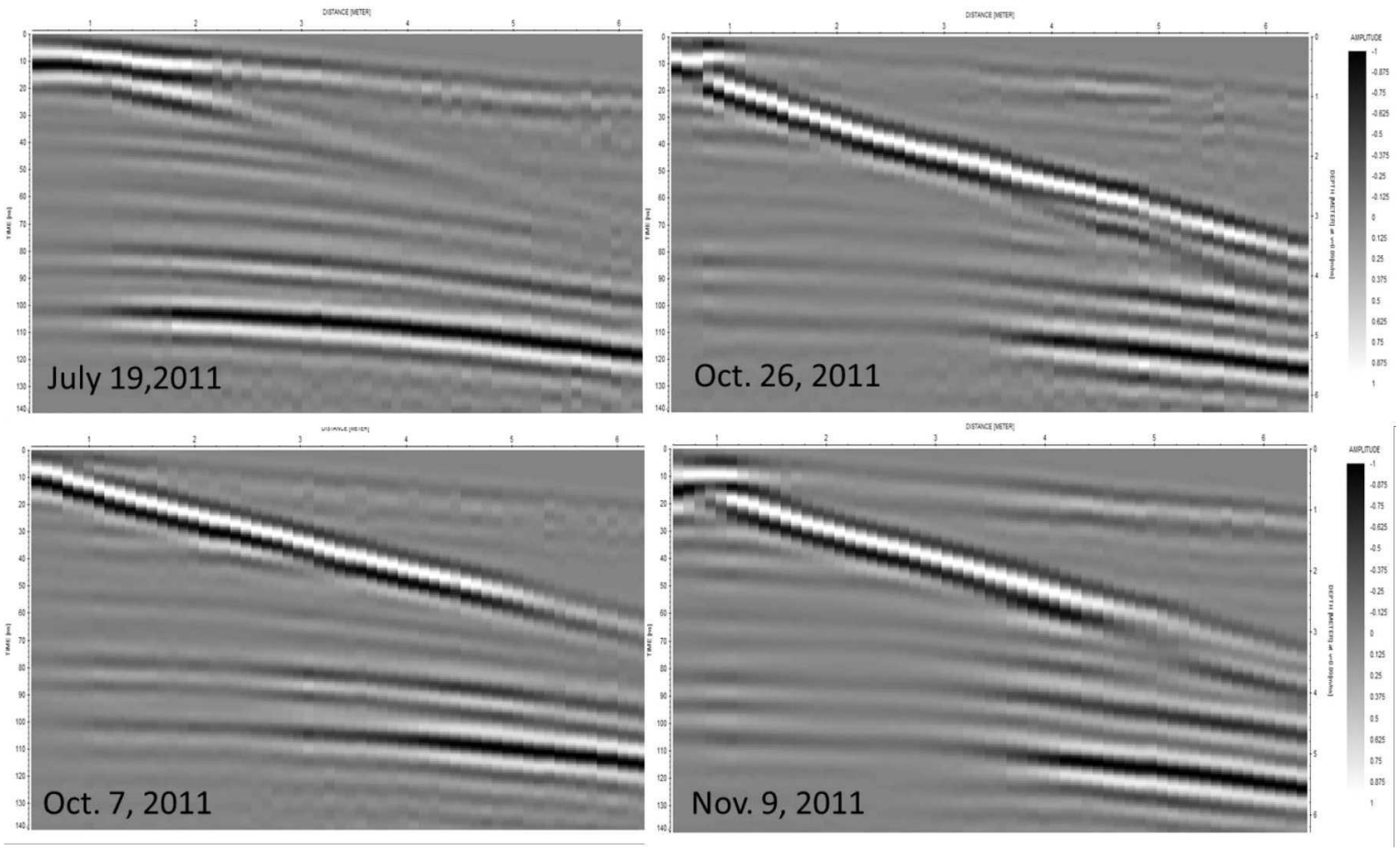

Figure B-1a: 200 MHz CMP survey collected at the 20 m survey location.

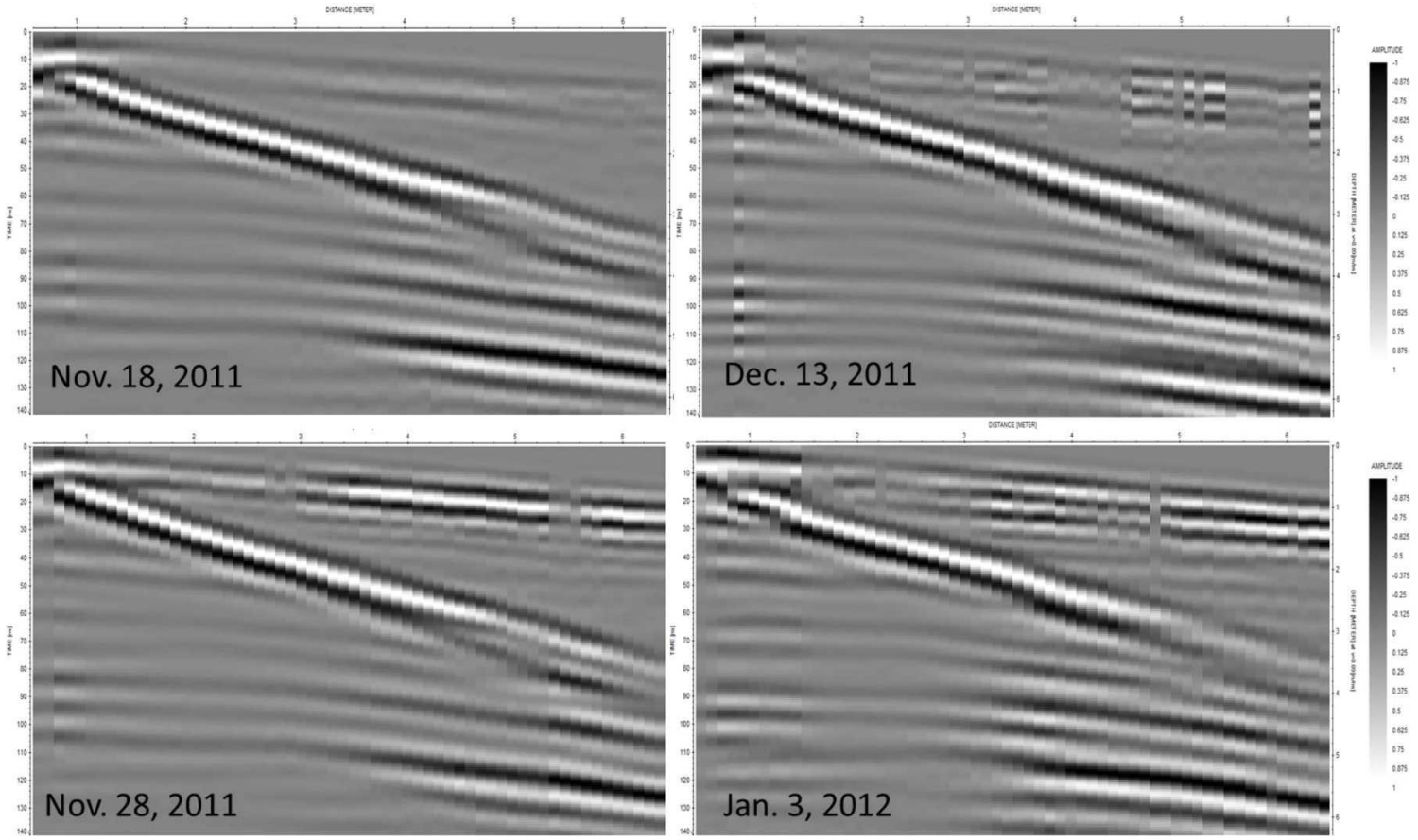

Figure B-1b: 200 MHz CMP survey collected at the 20 m survey location.

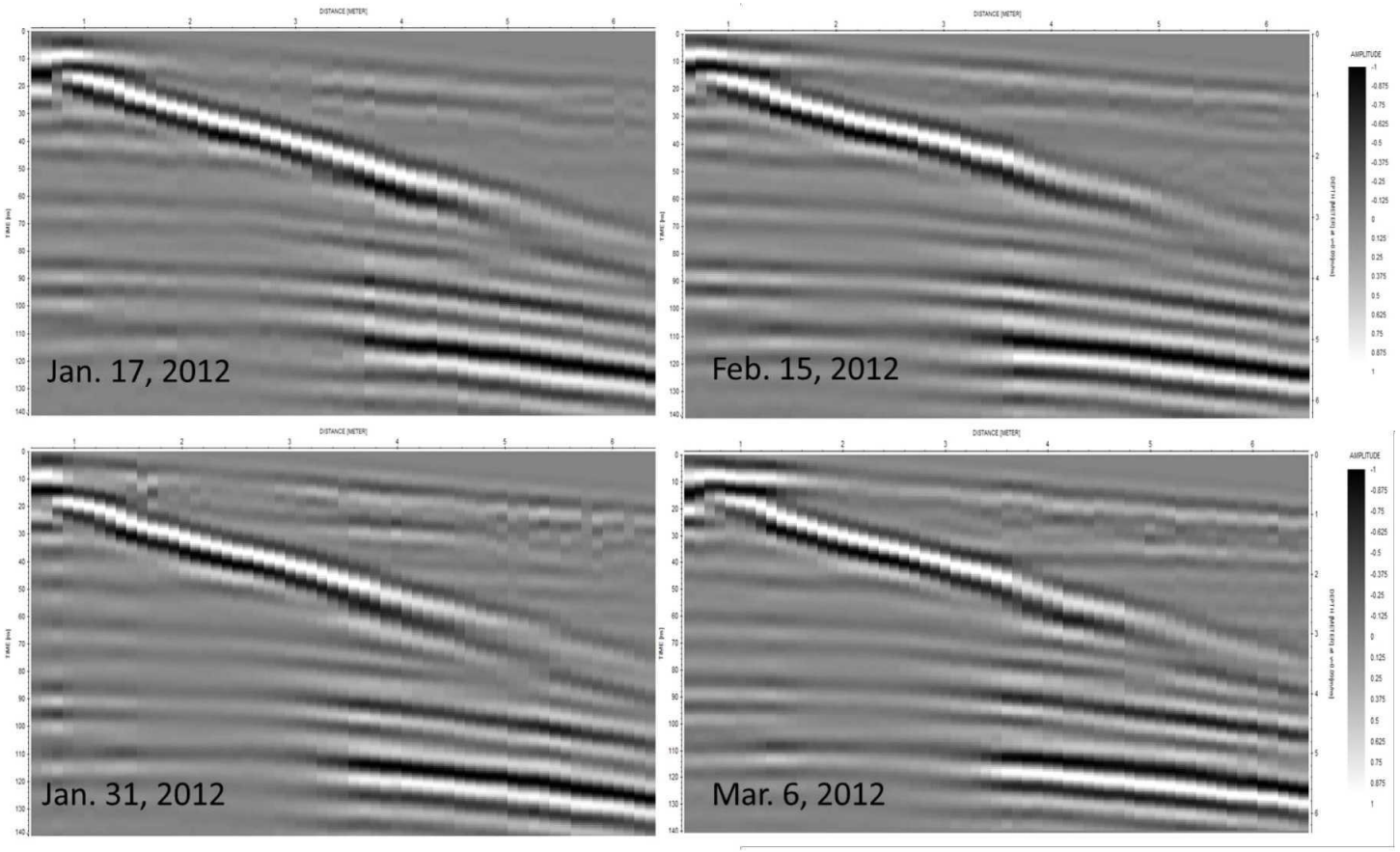

Figure B-1c: 200 MHz CMP survey collected at the 20 m survey location.

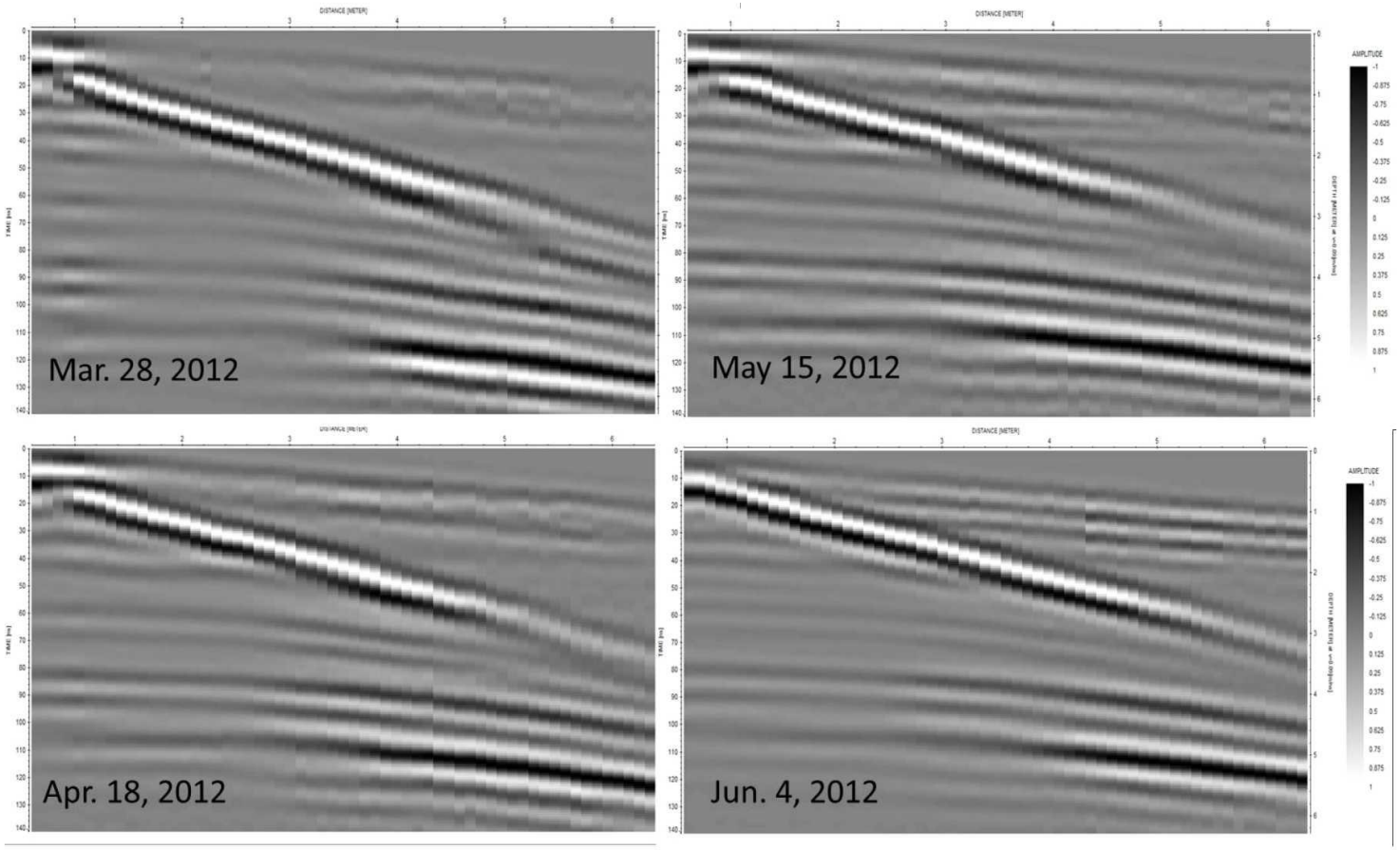

Figure B-1d: 200 MHz CMP survey collected at the 20 m survey location.

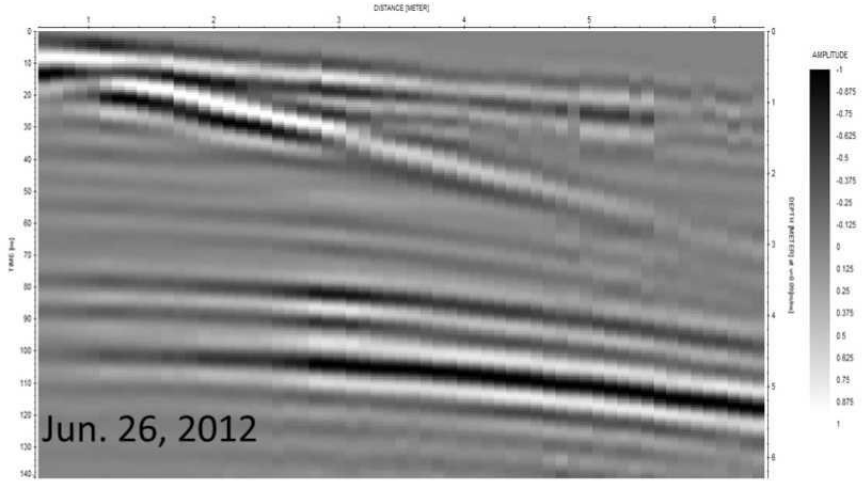

Figure B-1e: 200 MHz CMP survey collected at the 20 m survey location.

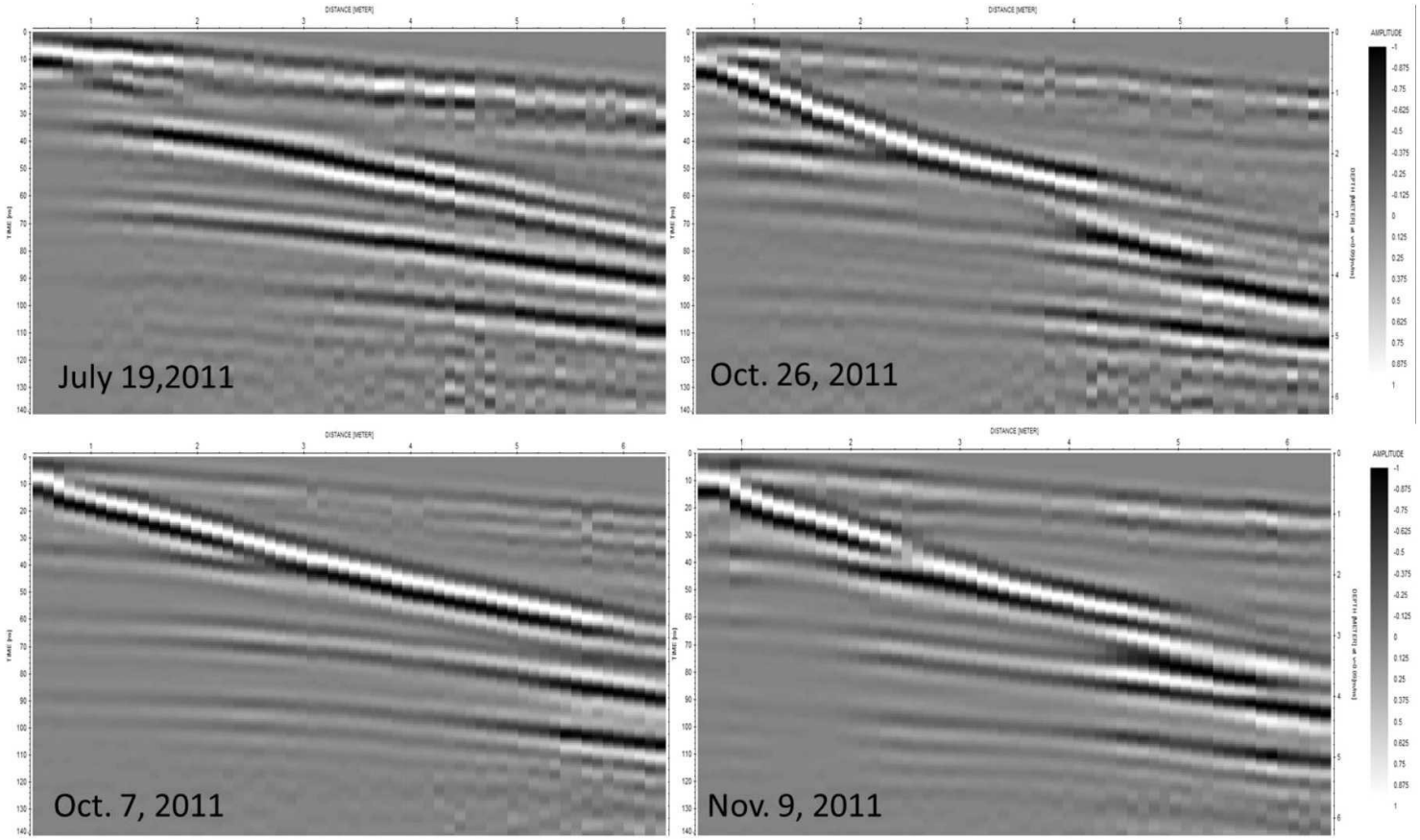

Figure B-2a: 200 MHz CMP survey collected at the 40 m survey location.

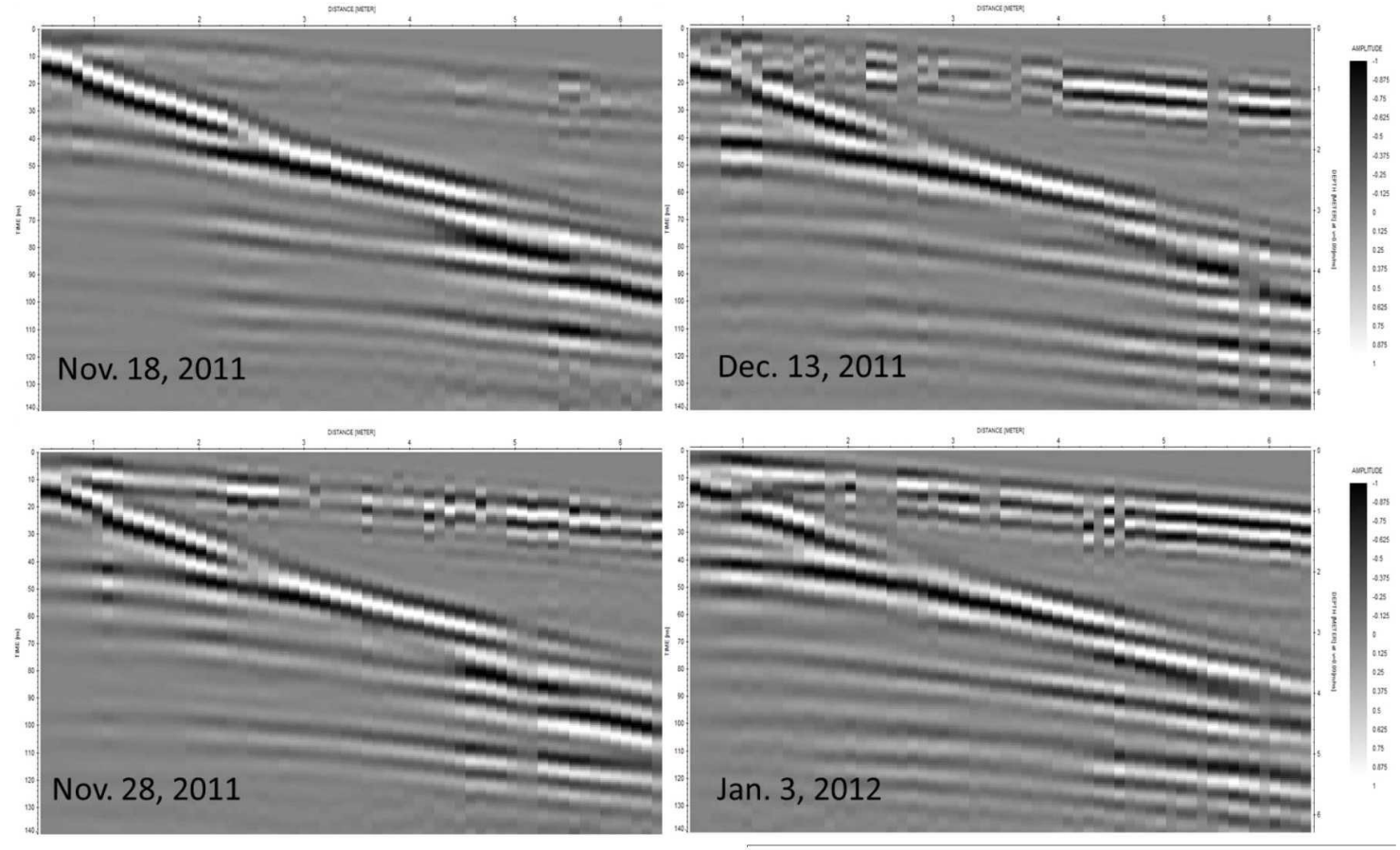

Figure B-2b: 200 MHz CMP survey collected at the 40 m survey location.

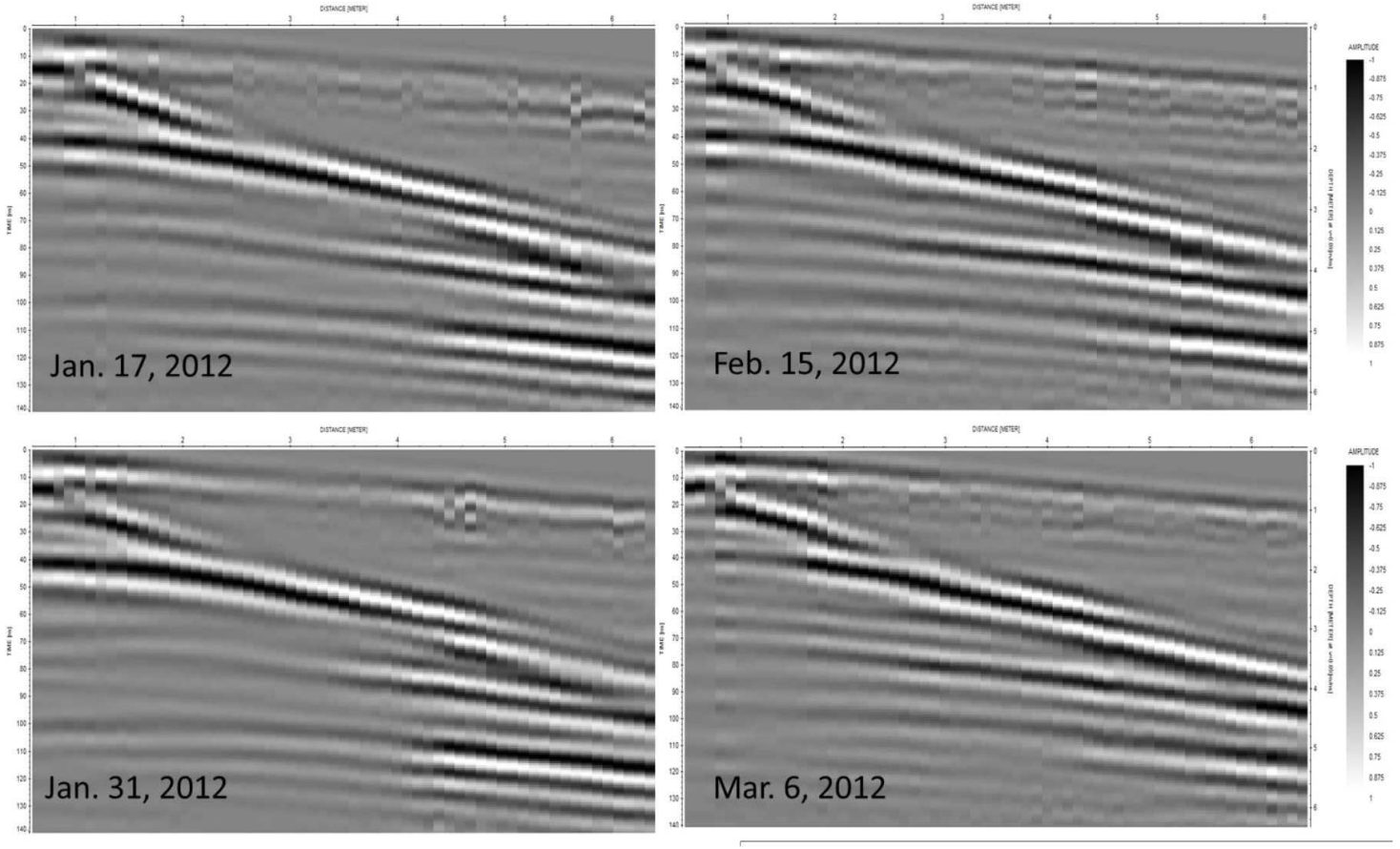

Figure B-2c: 200 MHz CMP survey collected at the 40 m survey location.

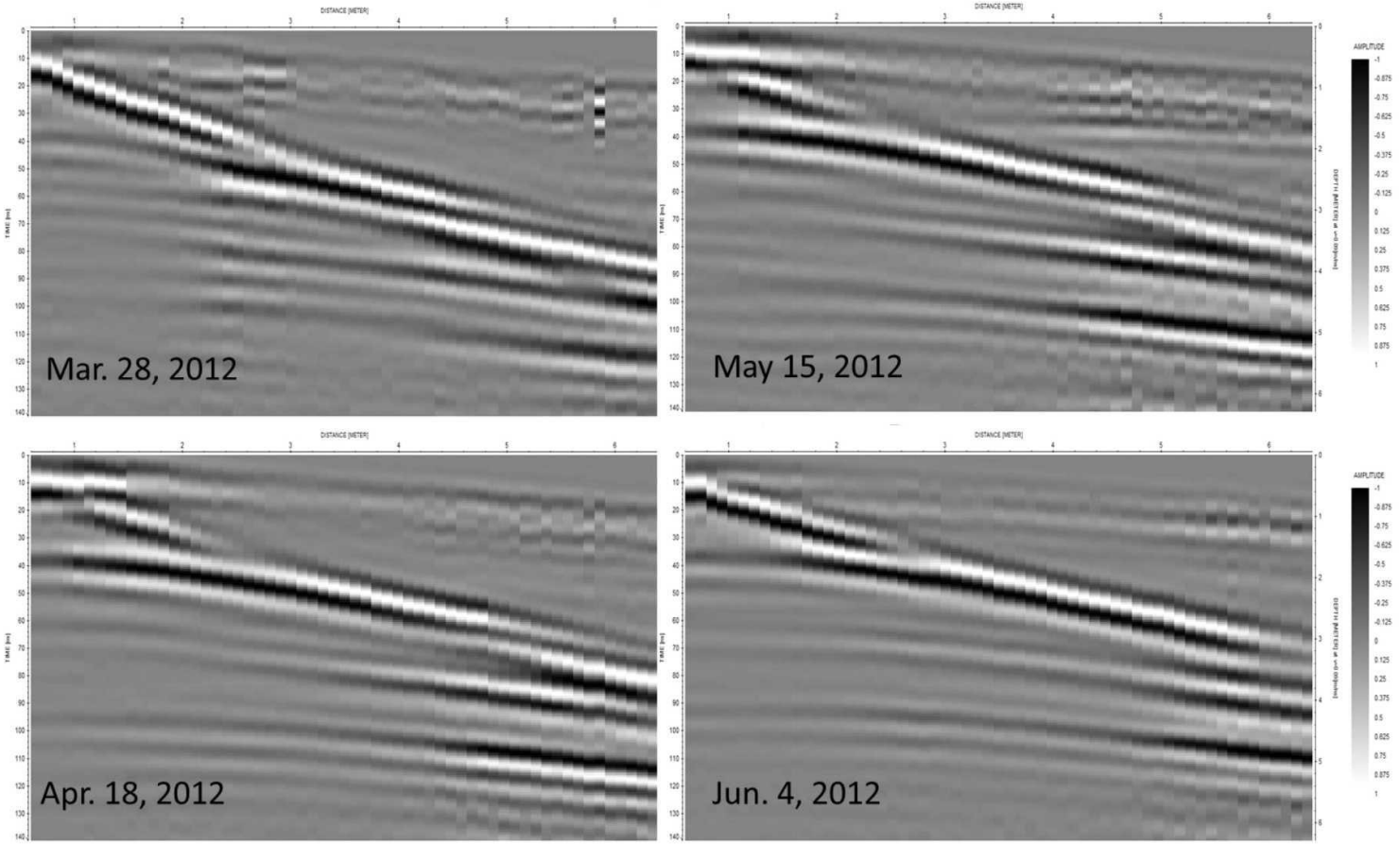

Figure B-2d: 200 MHz CMP survey collected at the 40 m survey location.

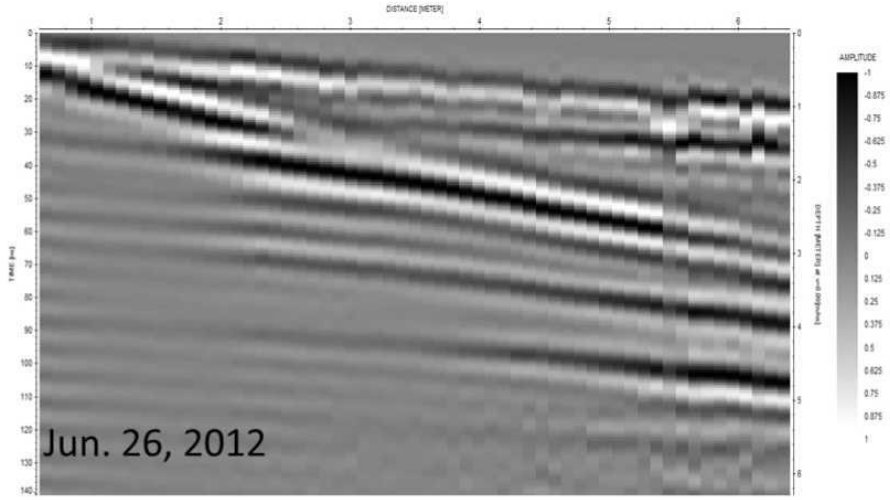

Figure B-2e: 200 MHz CMP survey collected at the 40 m survey location.

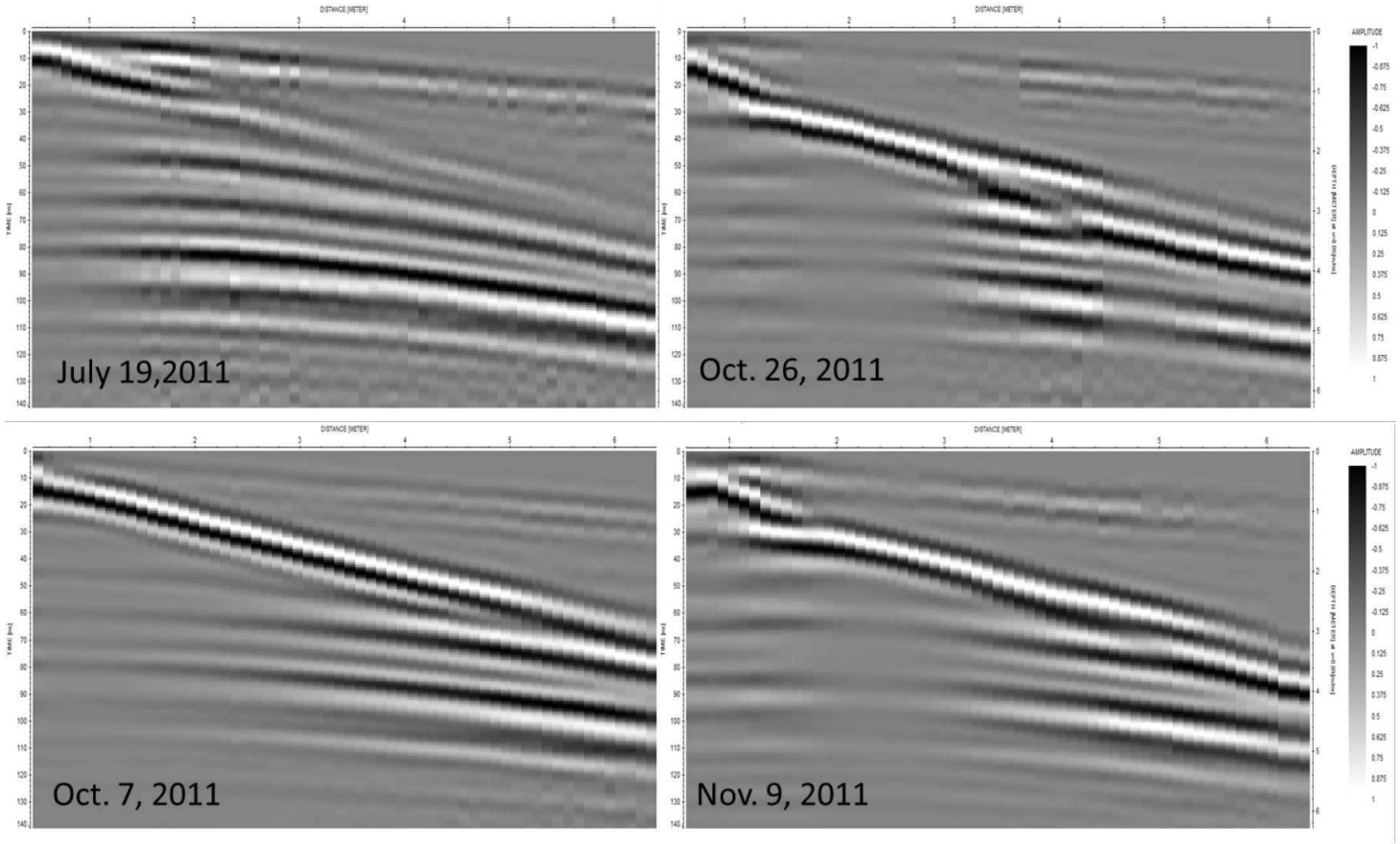

Figure B-3a: 200 MHz CMP survey collected at the 60 m survey location.

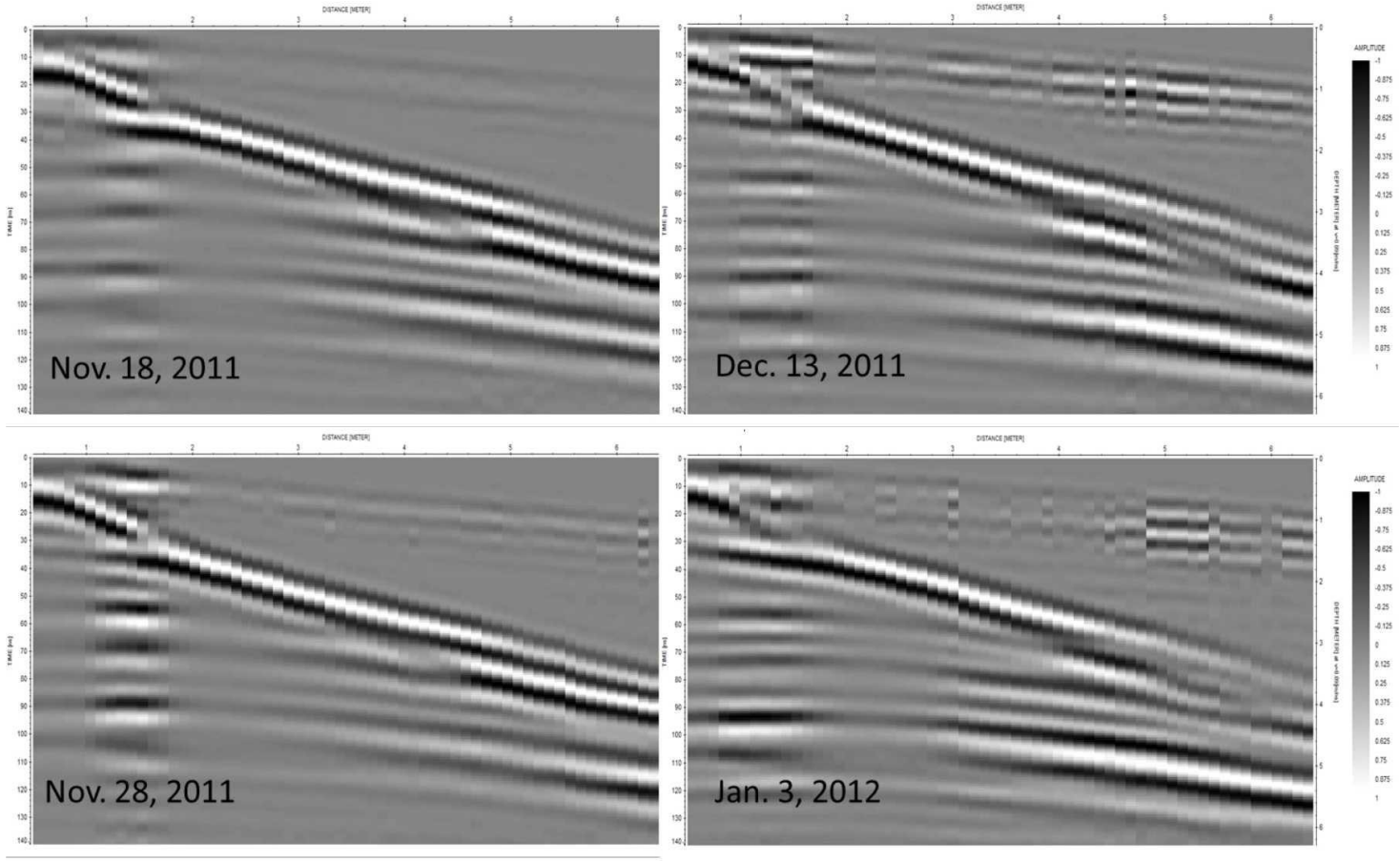

Figure B-3b: 200 MHz CMP survey collected at the 60 m survey location.

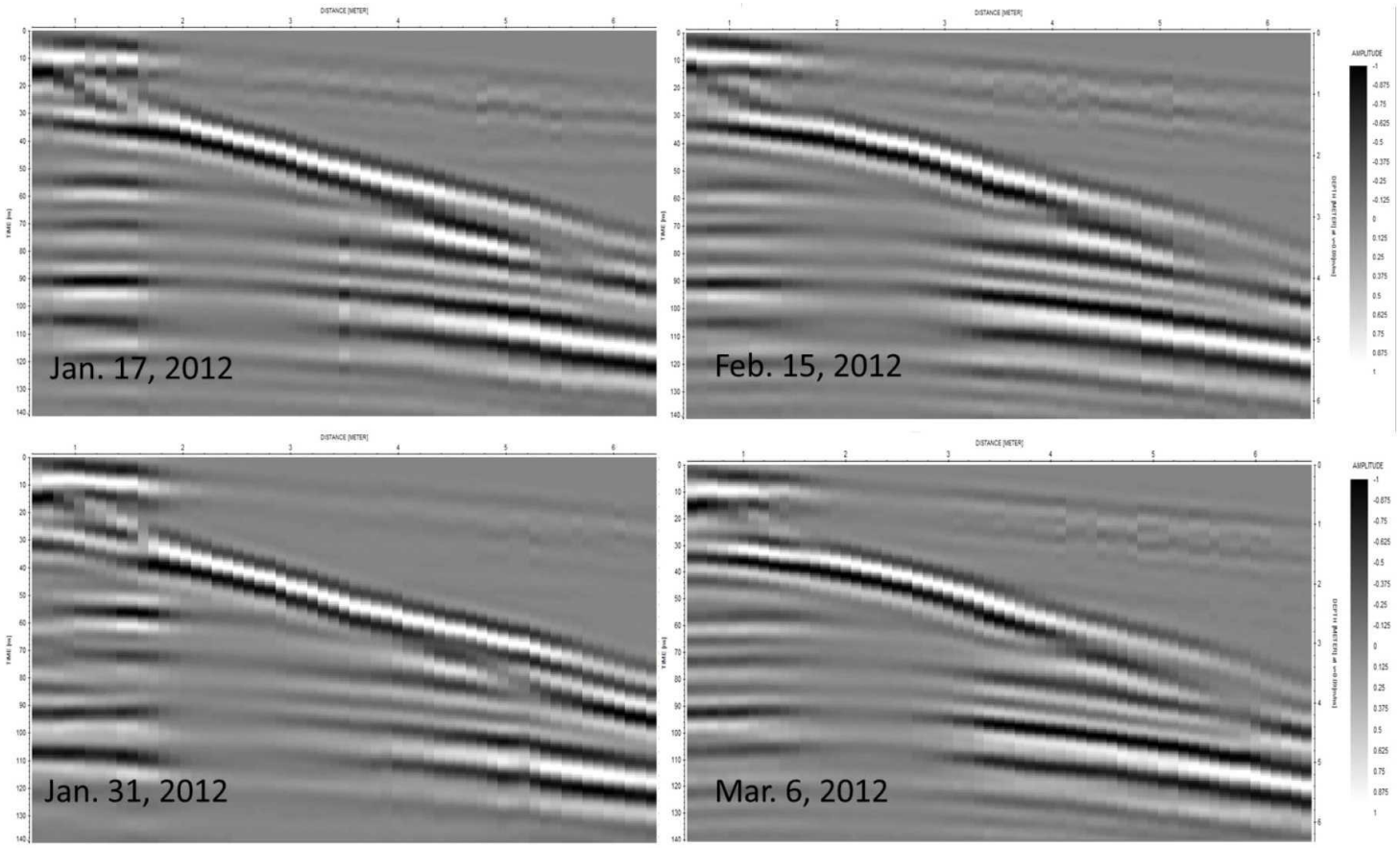

Figure B-3c: 200 MHz CMP survey collected at the 60 m survey location.

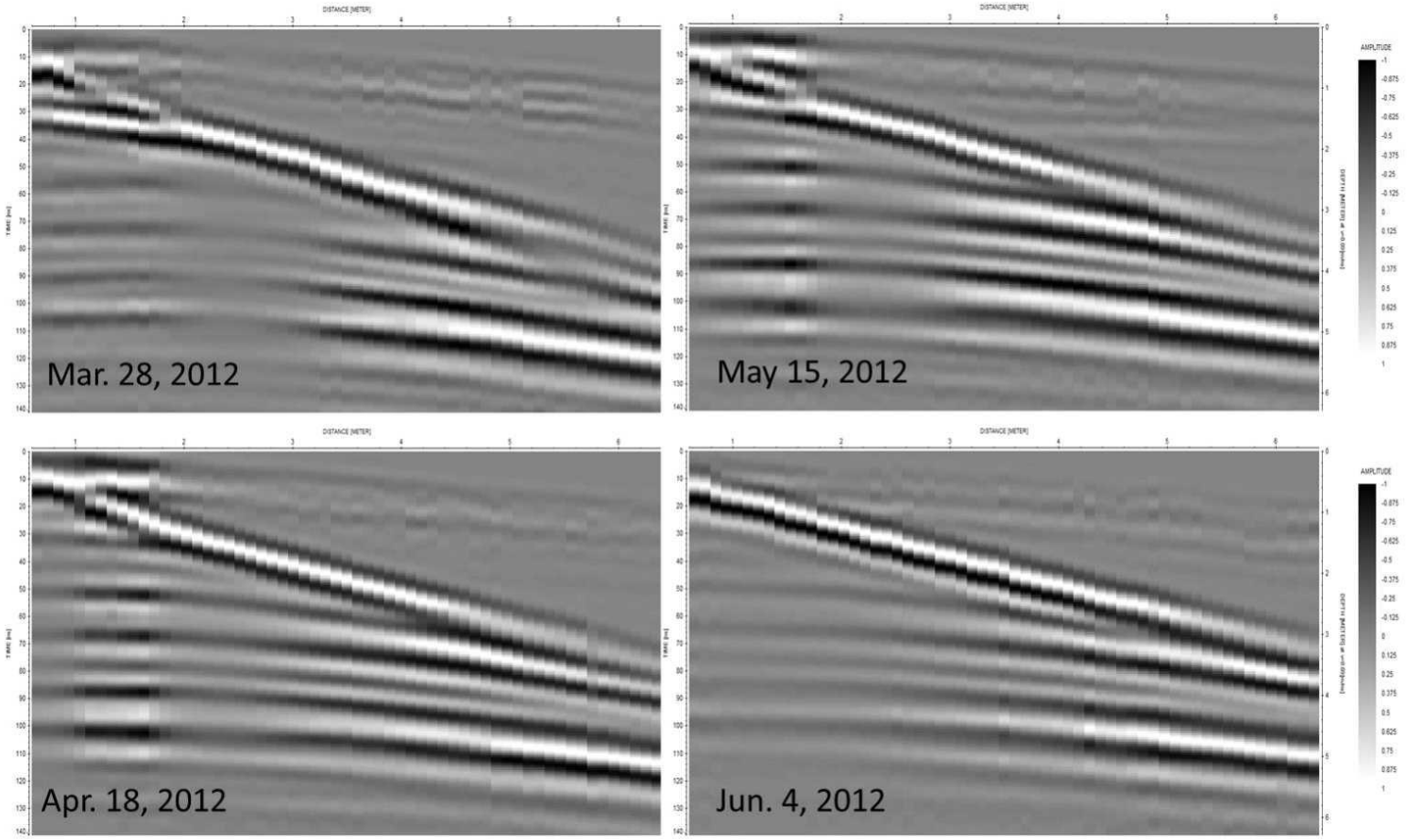

Figure B-3d: 200 MHz CMP survey collected at the 60 m survey location.

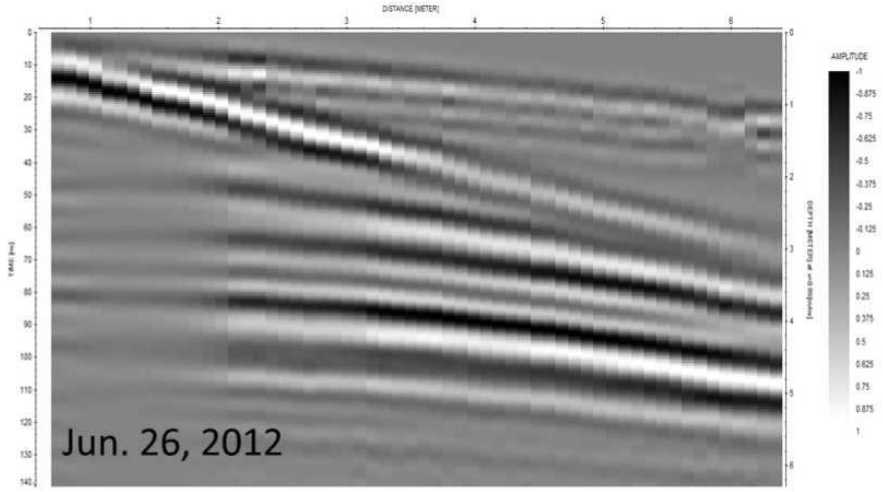

Figure B-3e: 200 MHz CMP survey collected at the 60 m survey location.

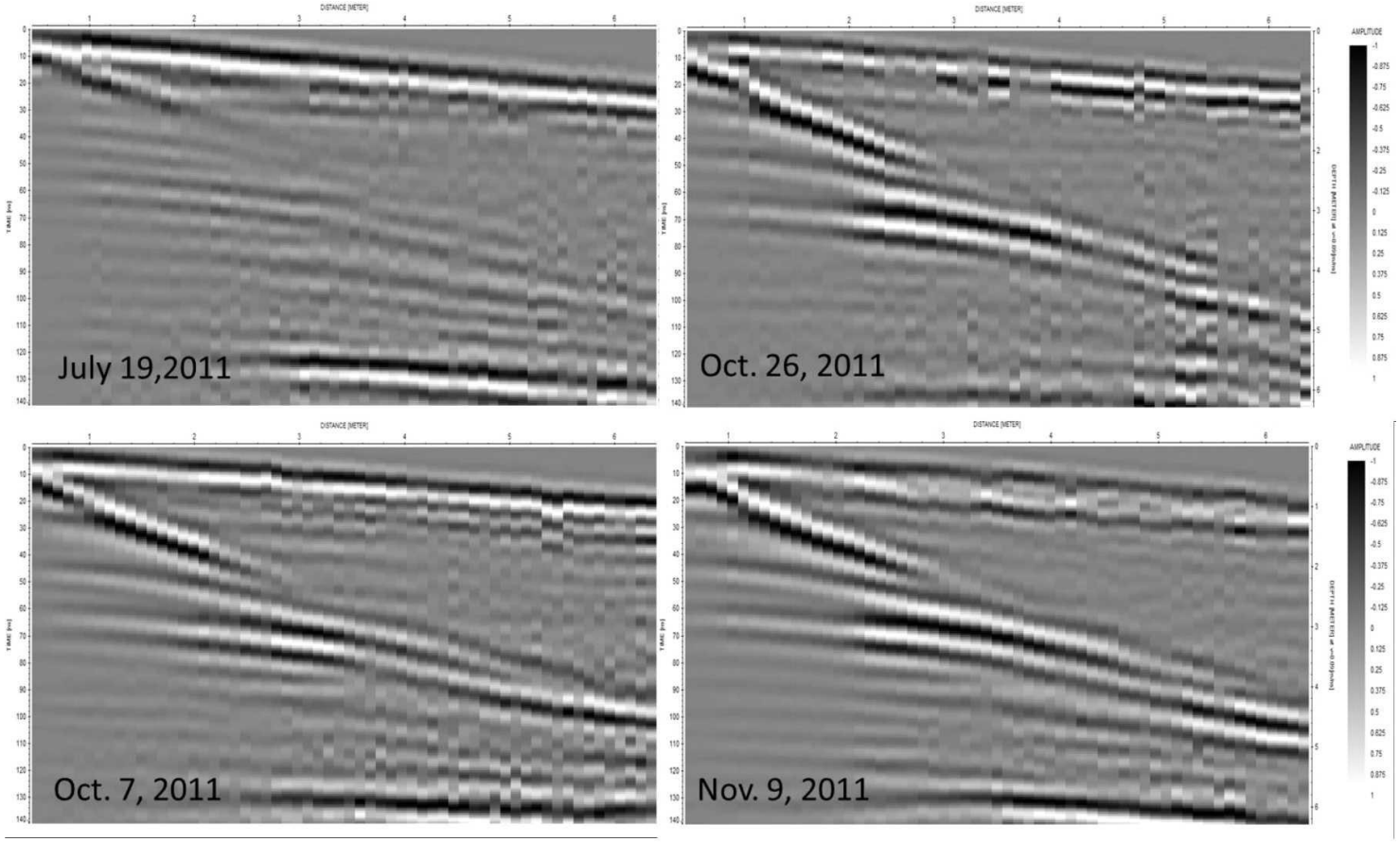

Figure B-4a: 200 MHz CMP survey collected at the 80 m survey location.

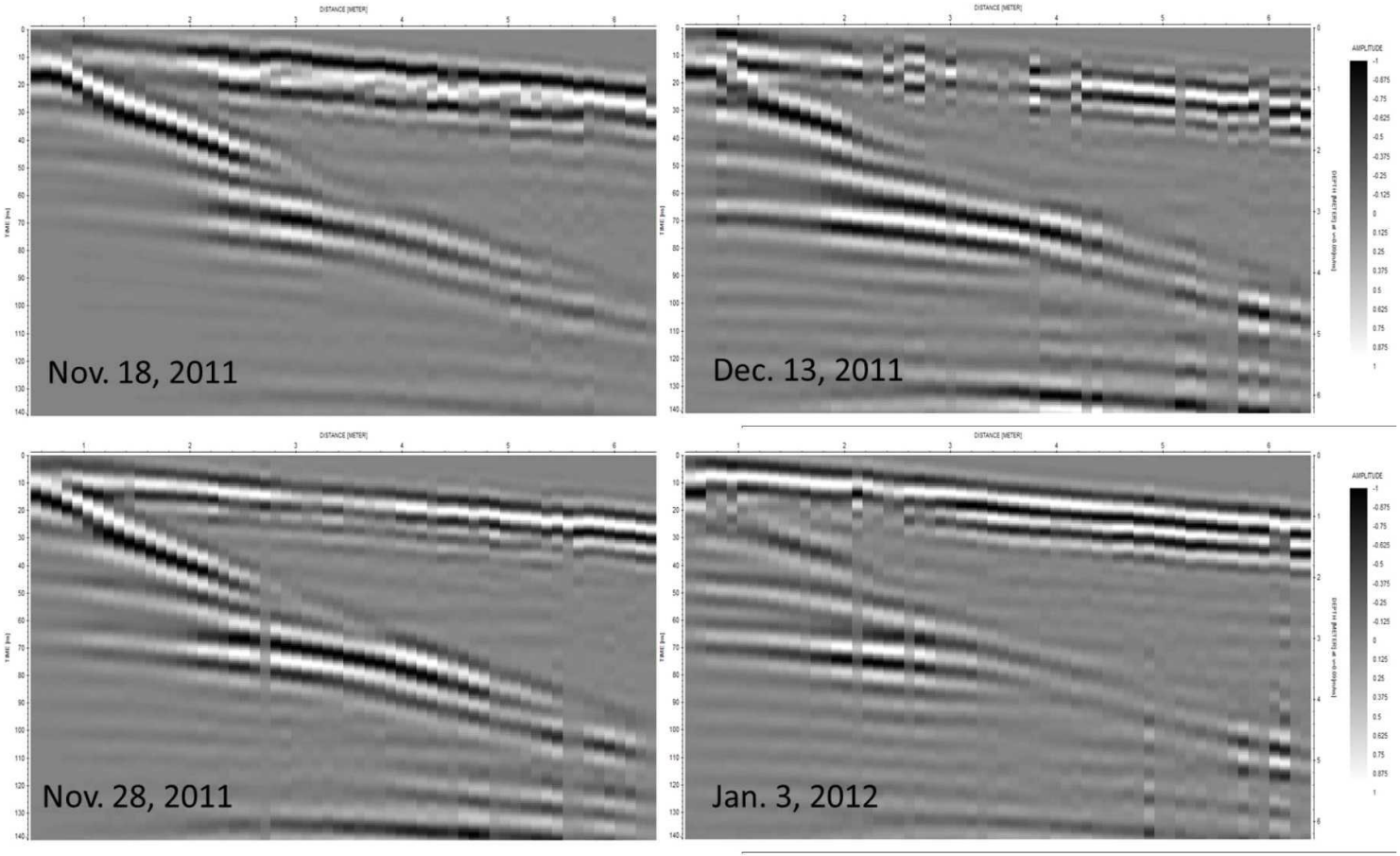

Figure B-4b: 200 MHz CMP survey collected at the 80 m survey location.

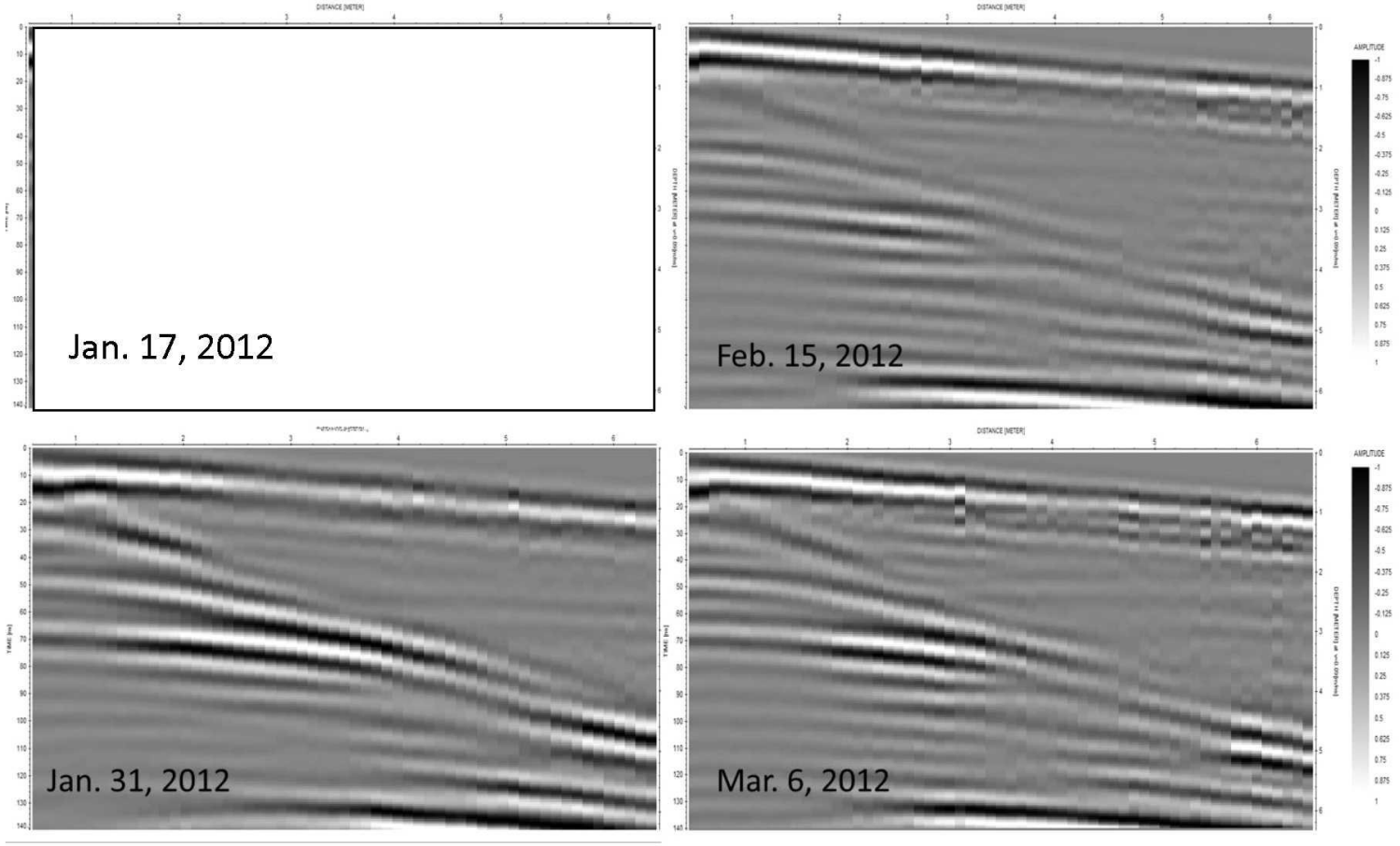

Figure B-4c: 200 MHz CMP survey collected at the 80 m survey location. No data was collected on January 17. 2012.

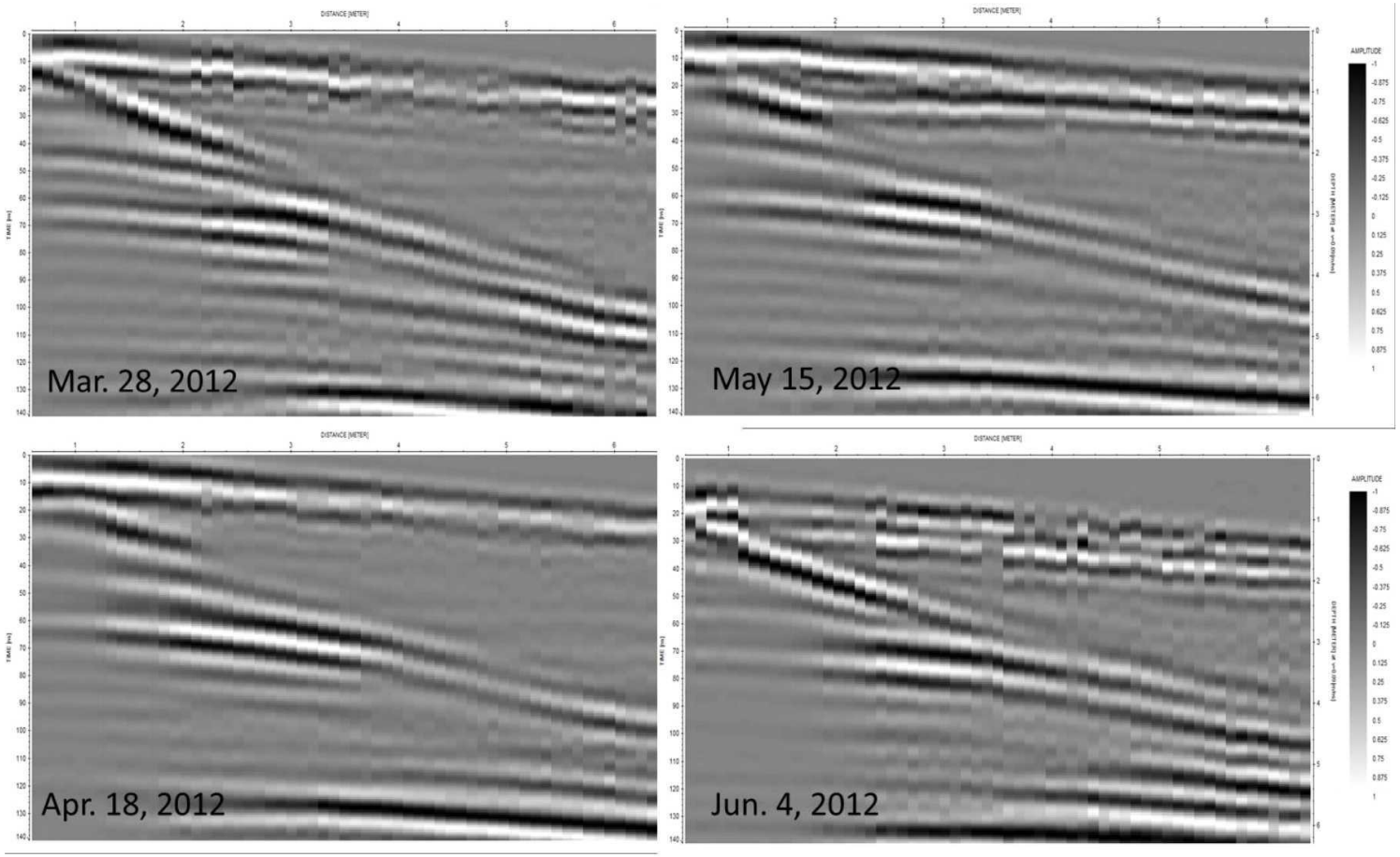

Figure B-4d: 200 MHz CMP survey collected at the 80 m survey location.

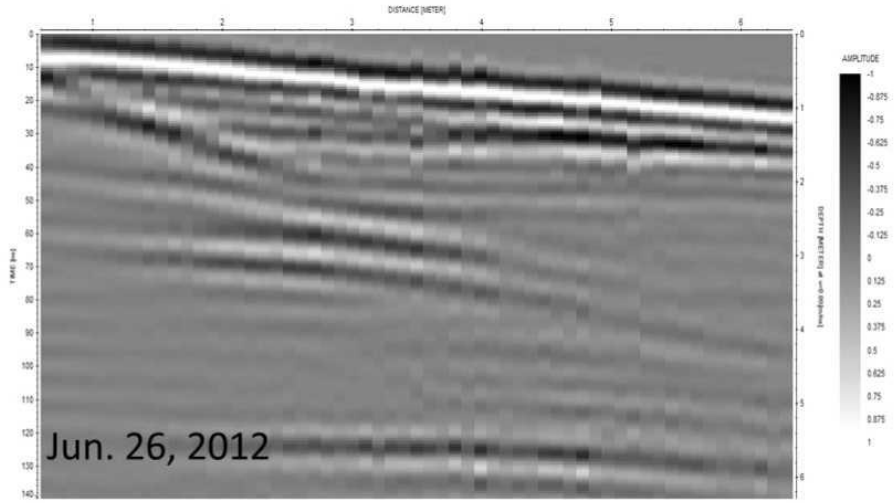

Figure B-4e: 200 MHz CMP survey collected at the 80 m survey location.

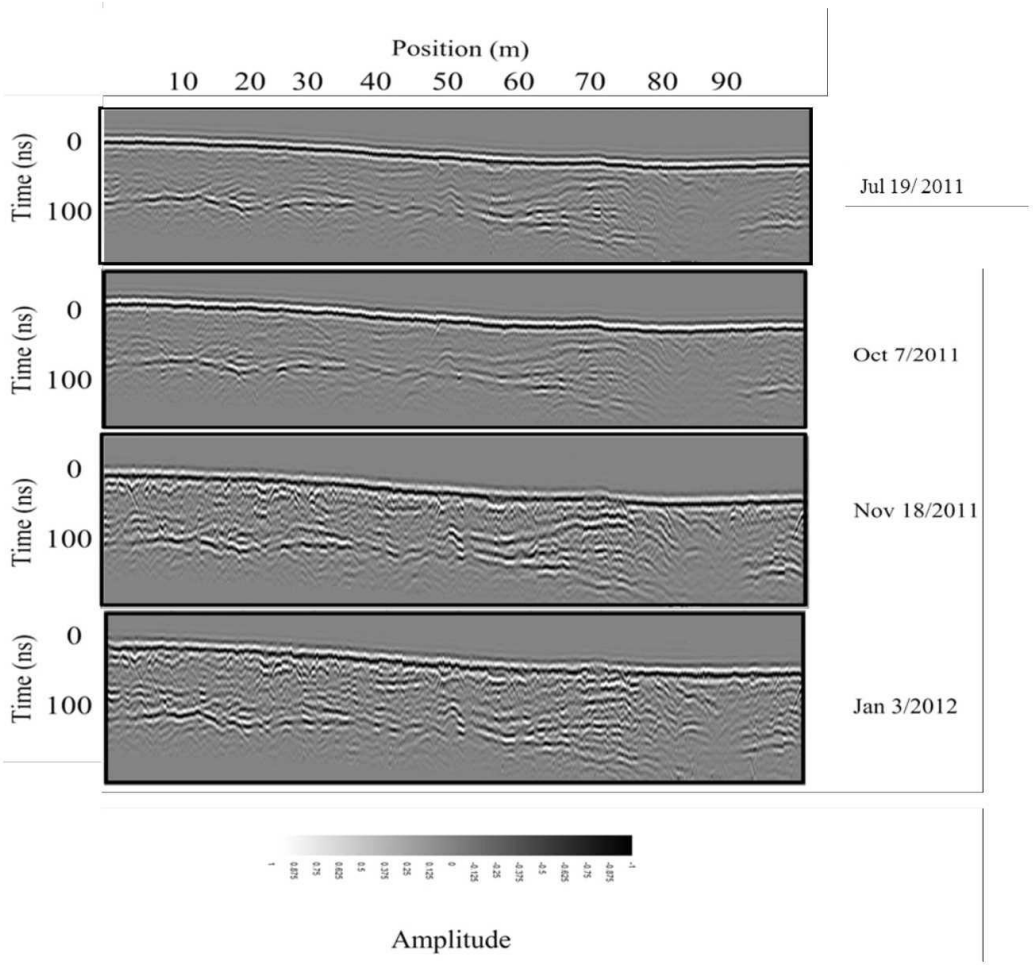

Figure B-5a: 200 MHz Reflection survey collected 0 m to 100 m along the survey line.

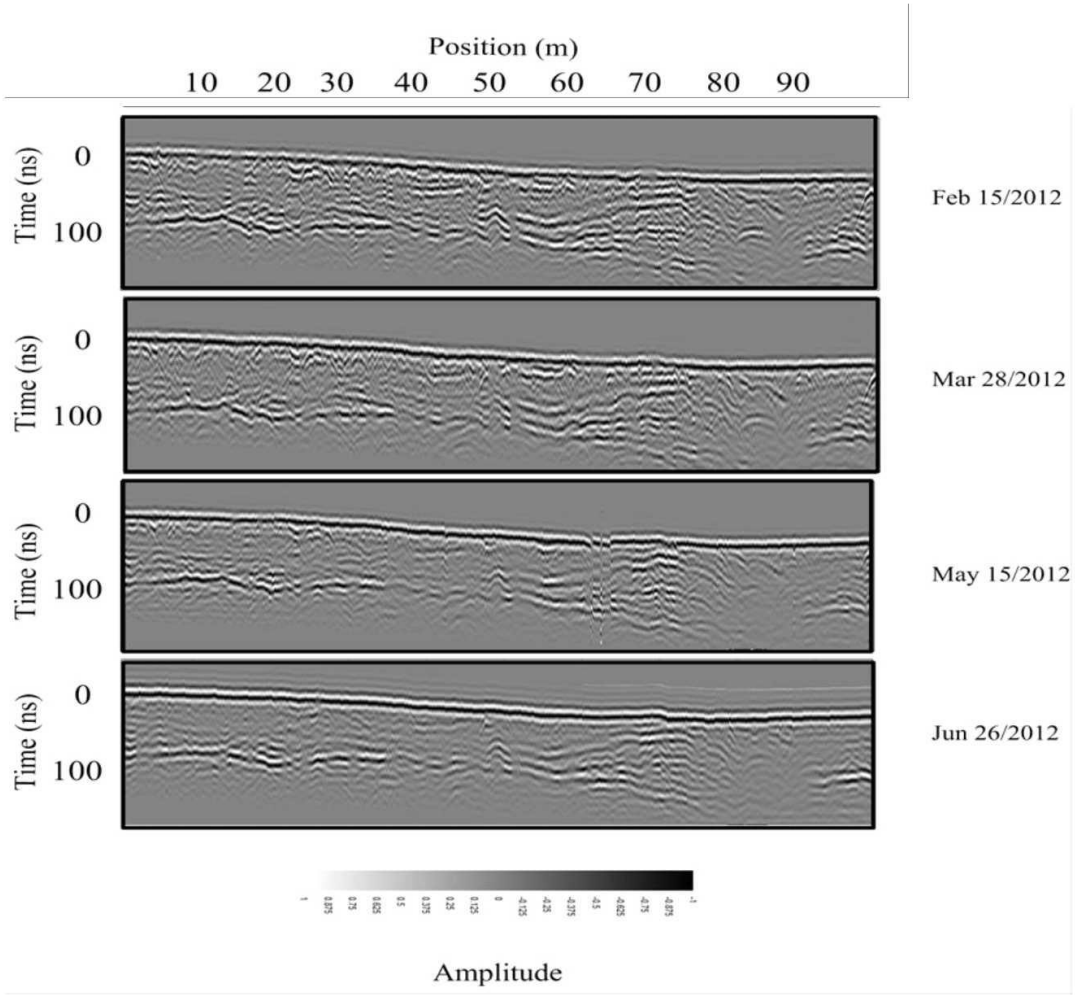

Figure B-5b: 200 MHz Reflection survey collected 0 m to 100 m along the survey line.

Appendix C

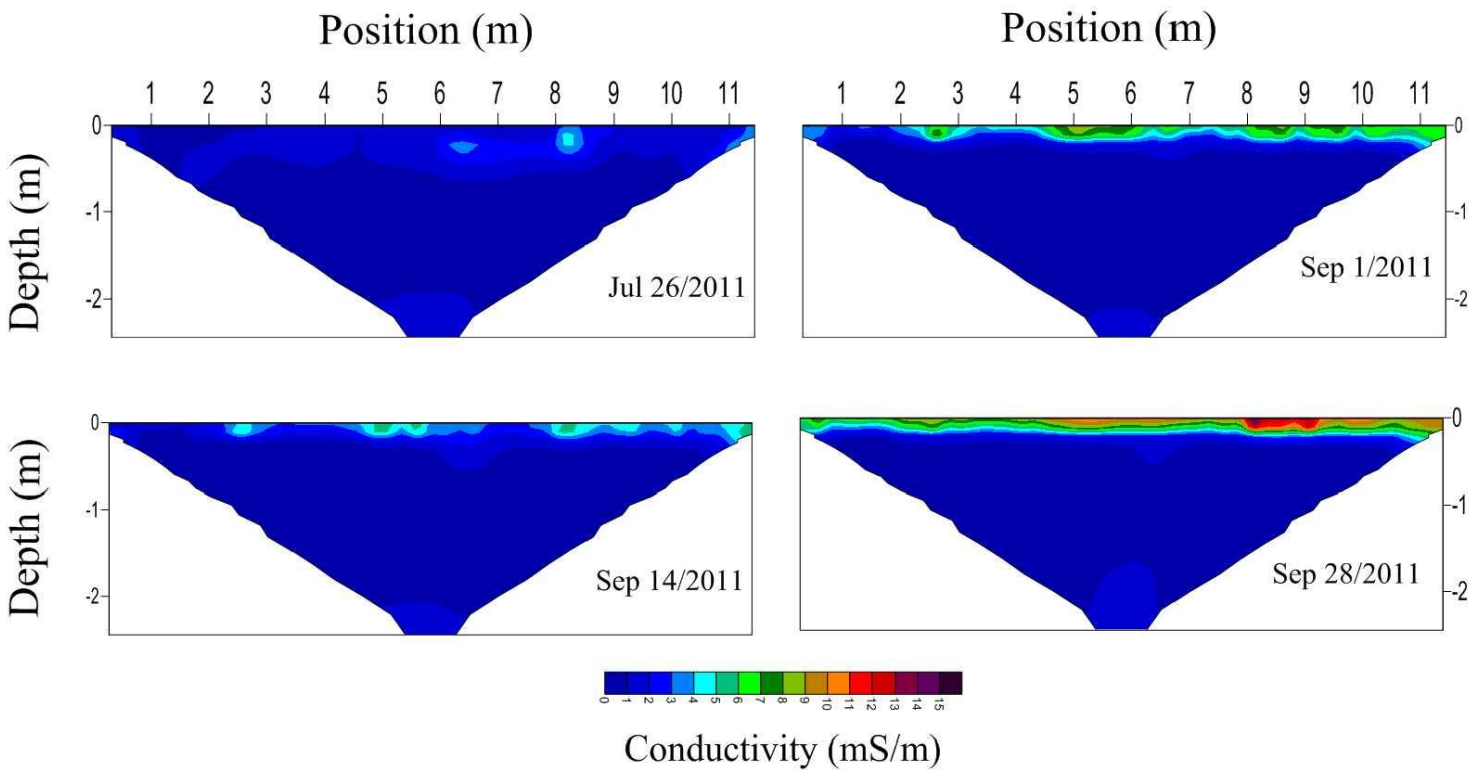

Figure C-1a: High resolution ERT results for the 10 m station plotted with respect to conductivity on a linear scale.

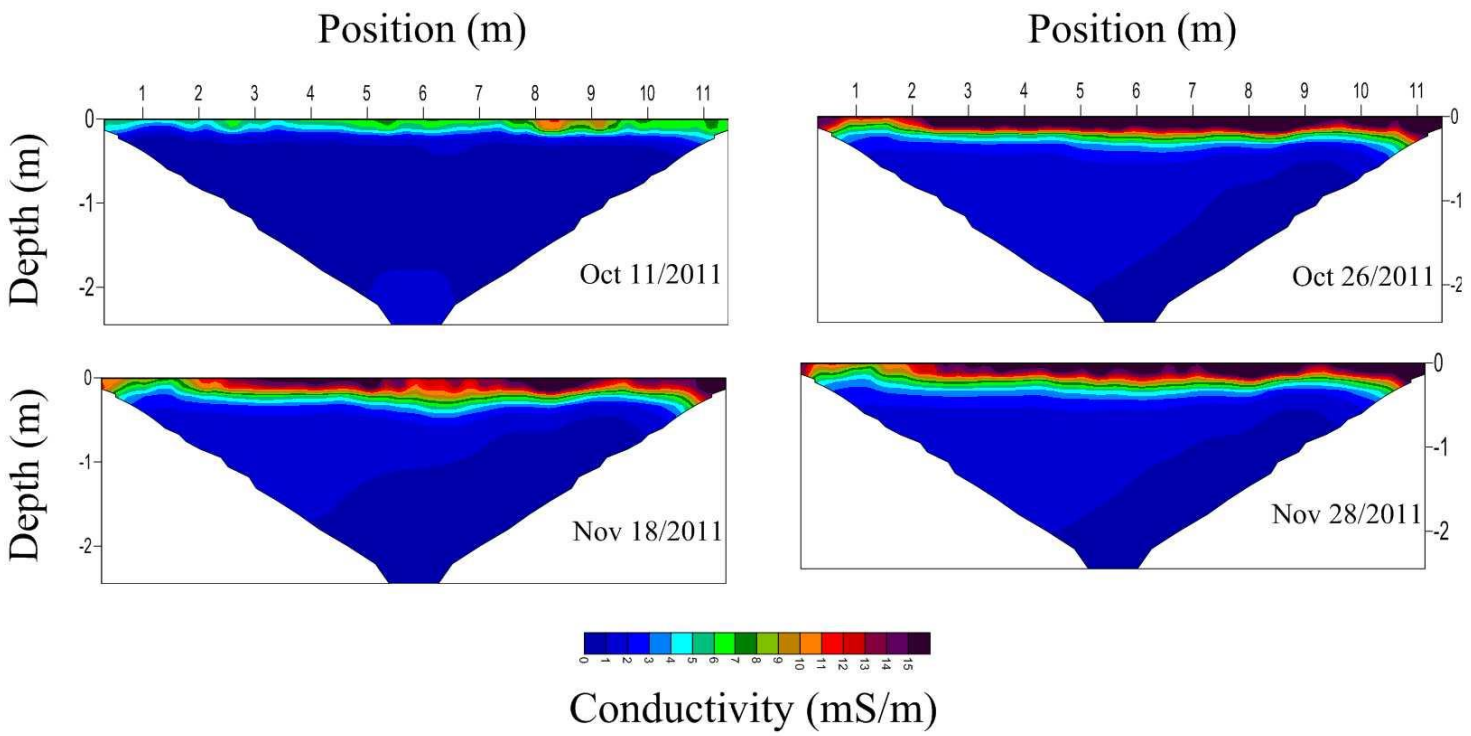

Figure C-1b: High resolution ERT results for the 10 m station plotted with respect to conductivity on a linear scale.

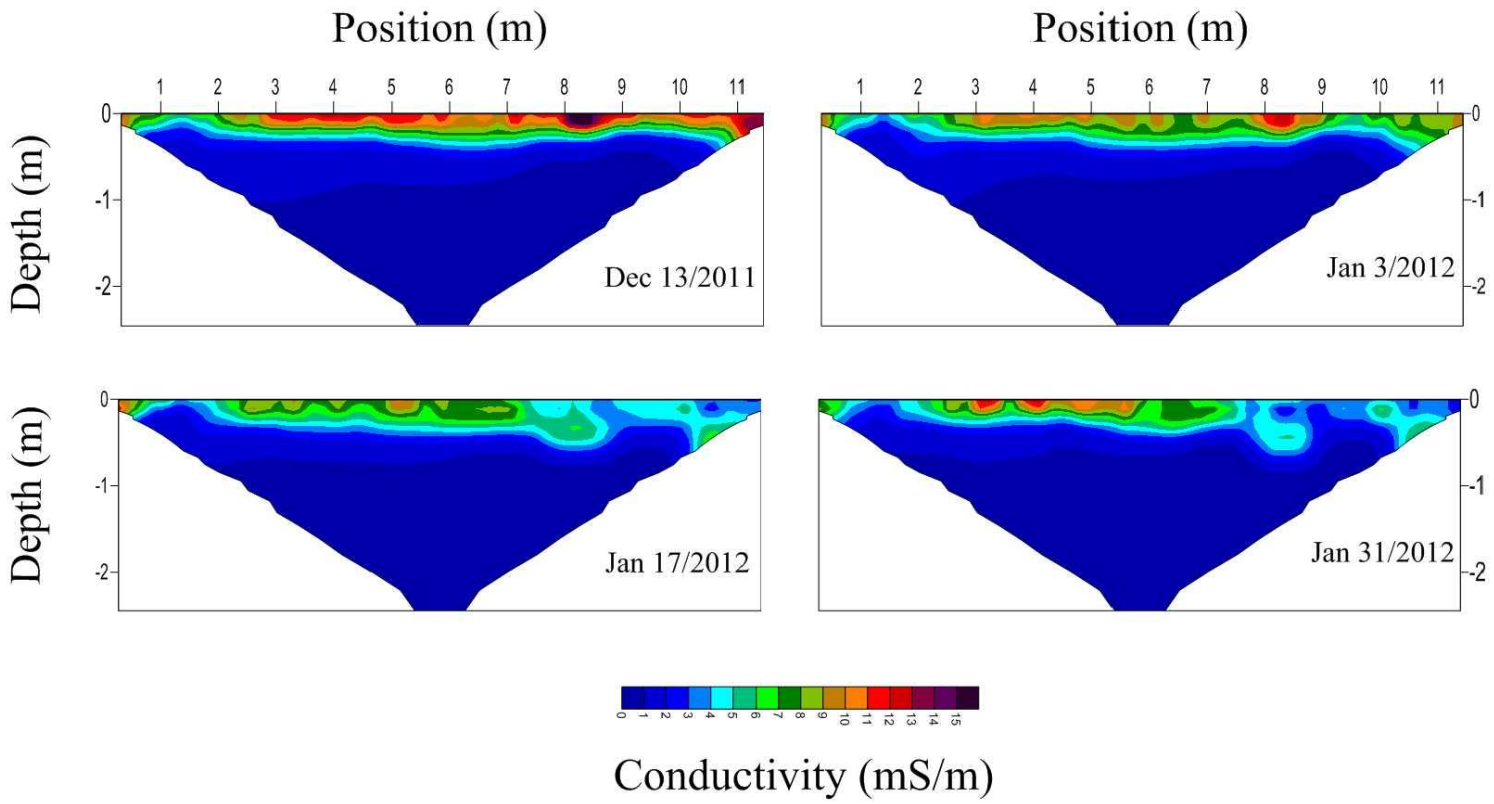

Figure C-1c: High resolution ERT results for the 10 m station plotted with respect to conductivity on a linear scale.

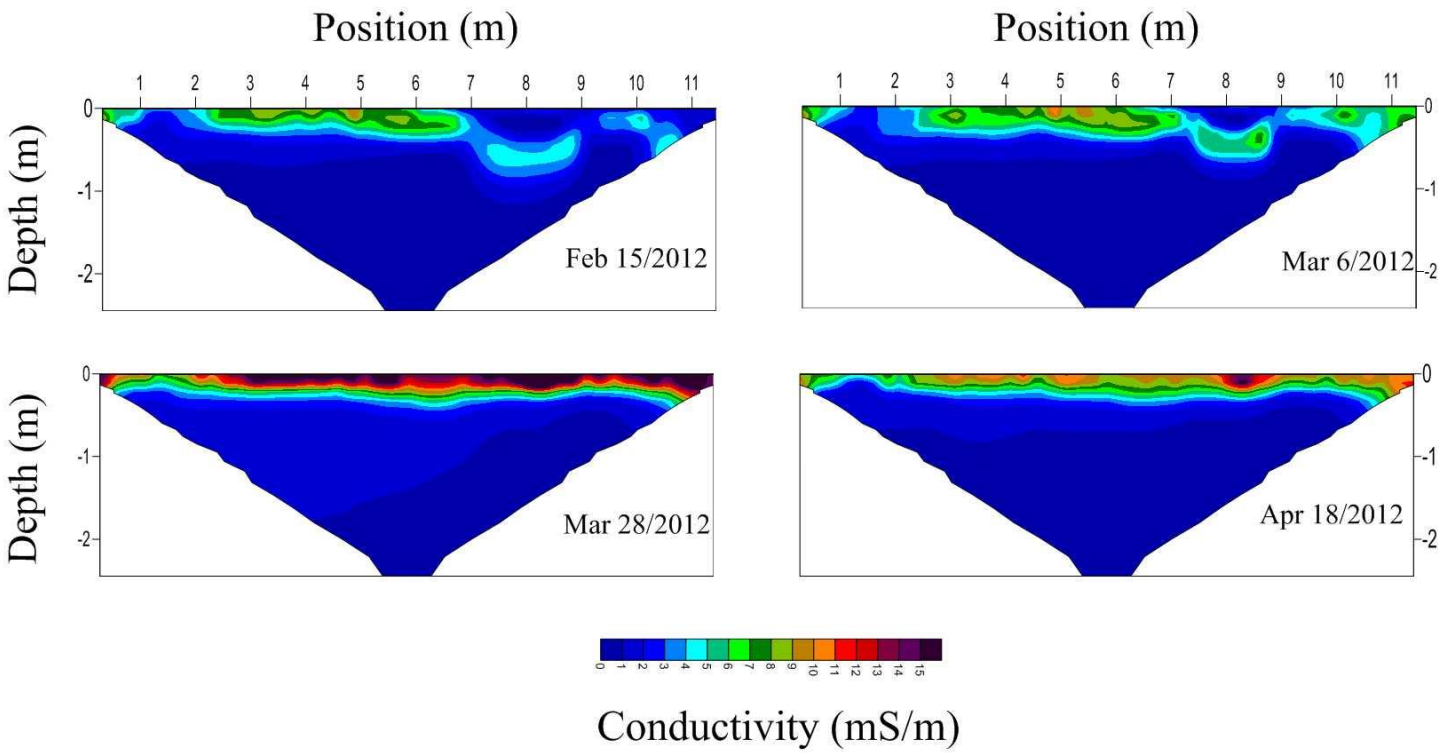

Figure C-1d: High resolution ERT results for the 10 m station plotted with respect to conductivity on a linear scale.

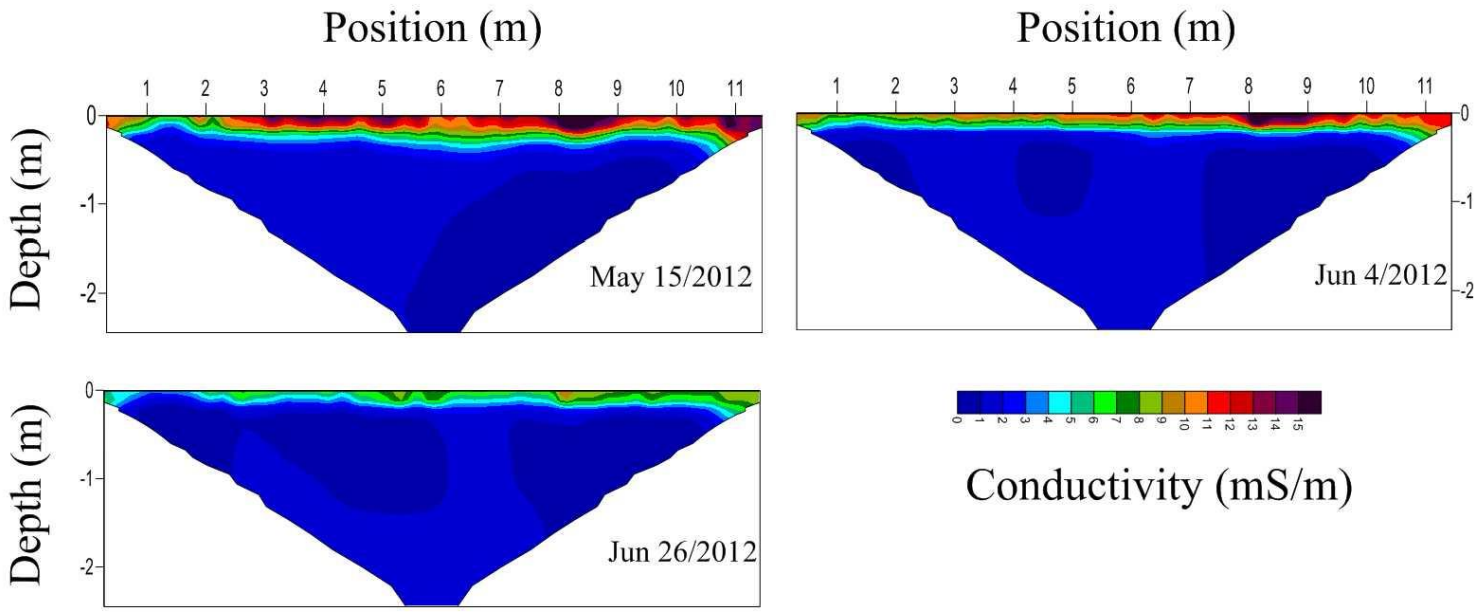

Figure C-1e: High resolution ERT results for the 10 m station plotted with respect to conductivity on a linear scale.

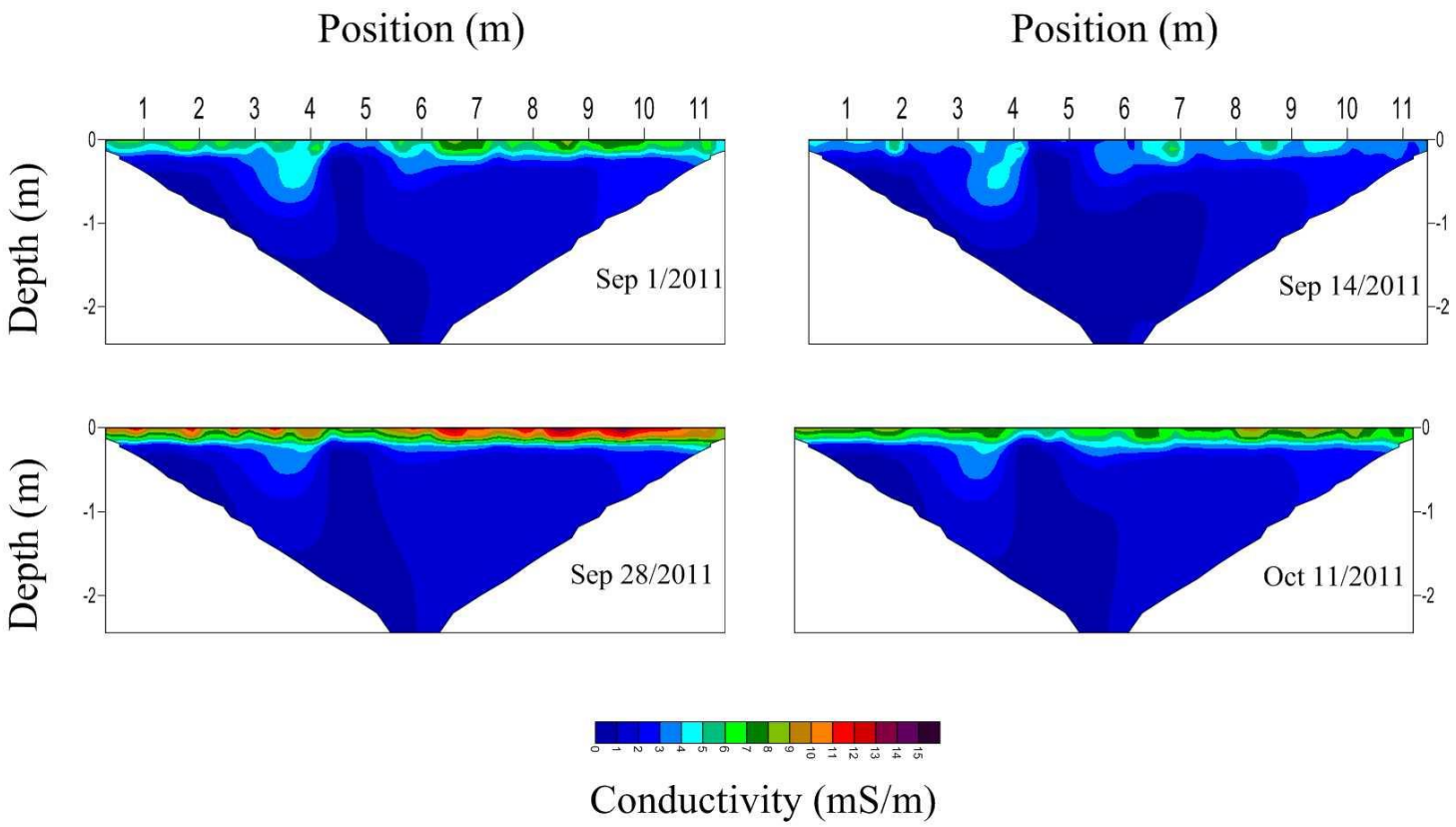

Figure C-2a: High resolution ERT results for the 50 m station plotted with respect to conductivity on a linear scale.

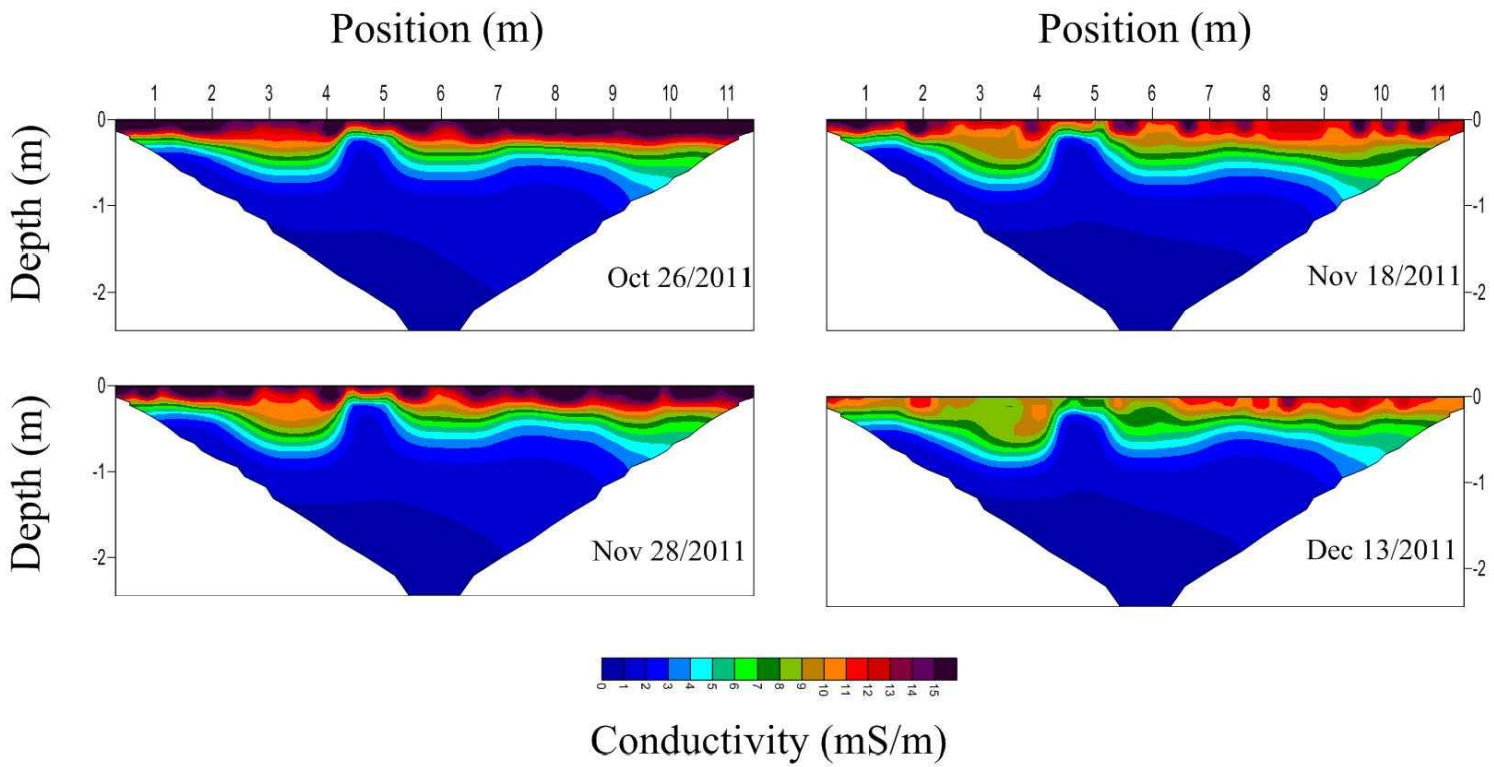

Figure C-2b: High resolution ERT results for the 50 m station plotted with respect to conductivity on a linear scale.

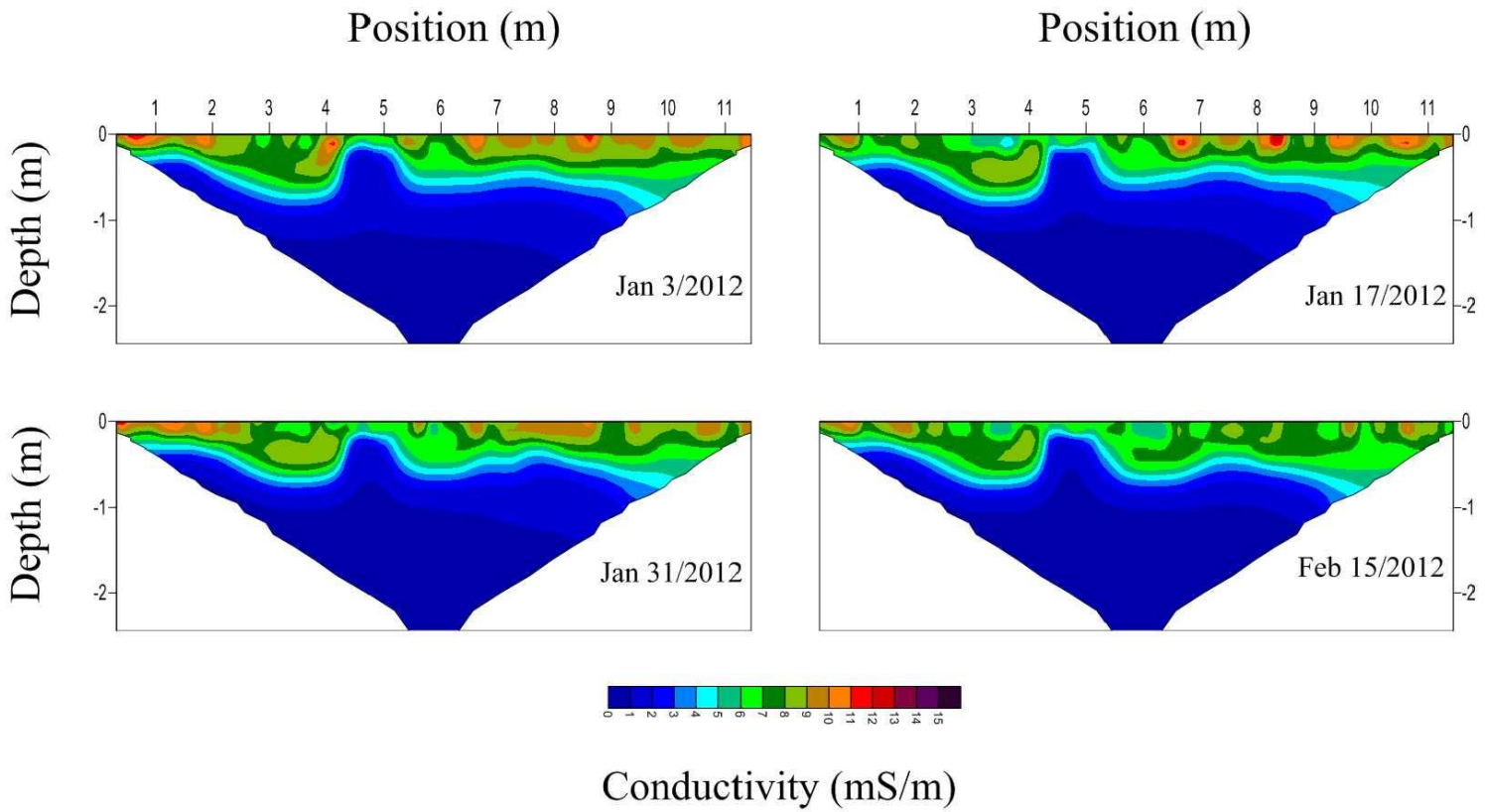

Figure C-2c: High resolution ERT results for the 50 m station plotted with respect to conductivity on a linear scale.

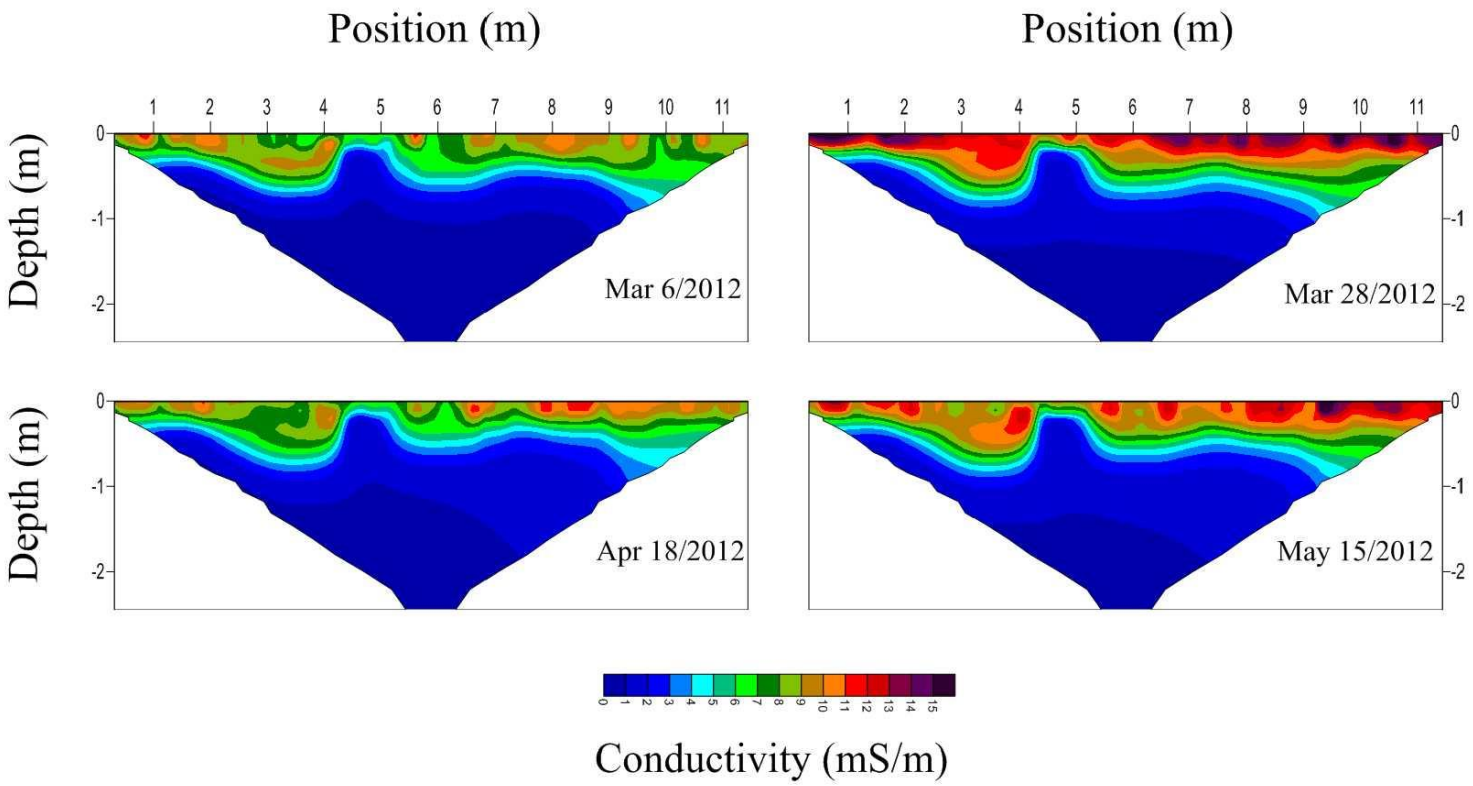

Figure C-2d: High resolution ERT results for the 50 m station plotted with respect to conductivity on a linear scale.

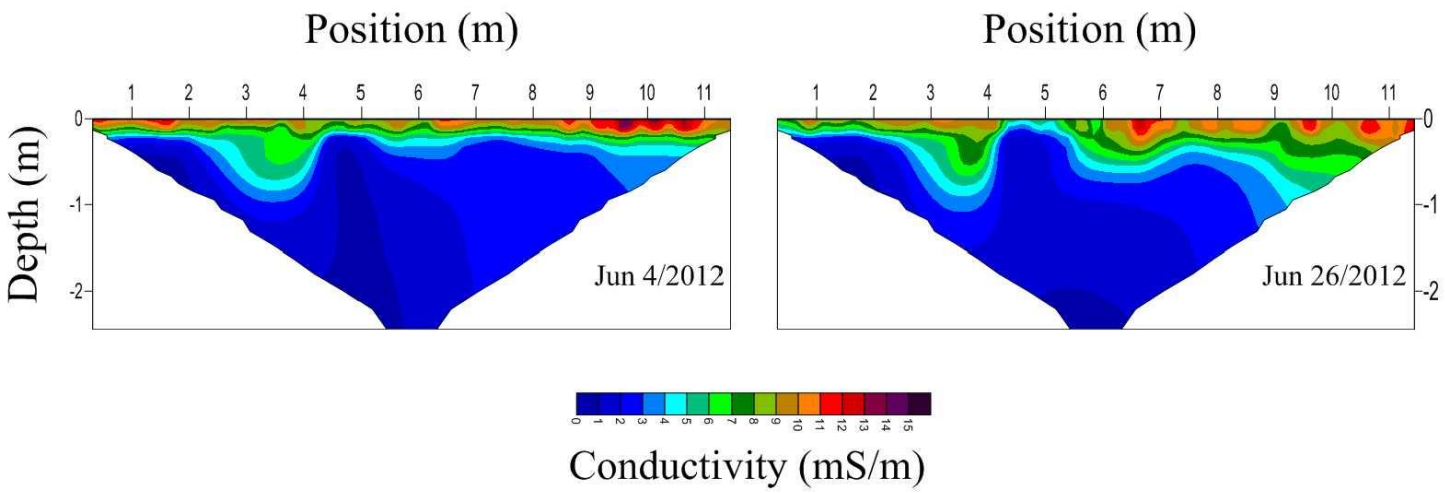

Figure C-2e: High resolution ERT results for the 50 m station plotted with respect to conductivity on a linear scale.

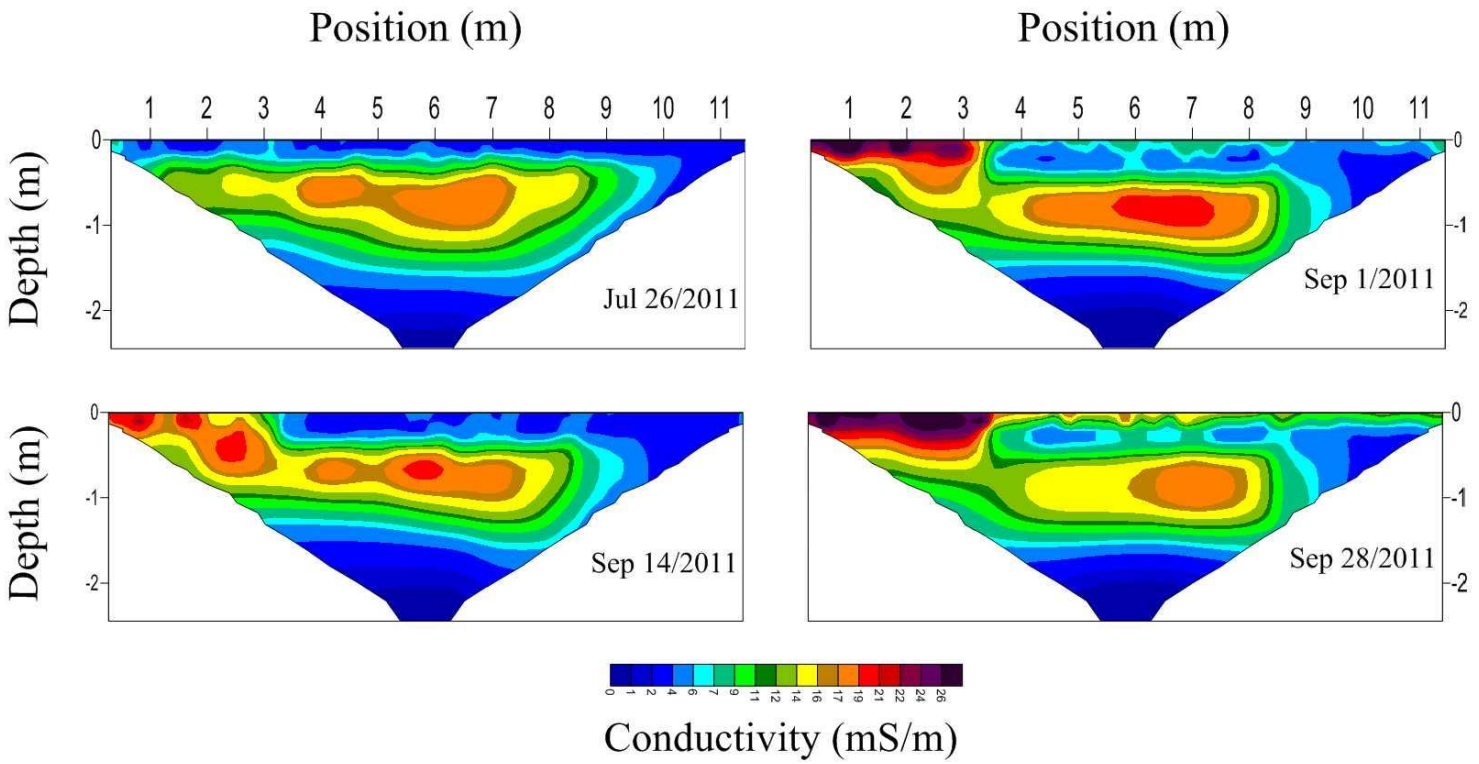

Figure C-3a: High resolution ERT results for the 85 m station plotted with respect to conductivity on a linear scale.

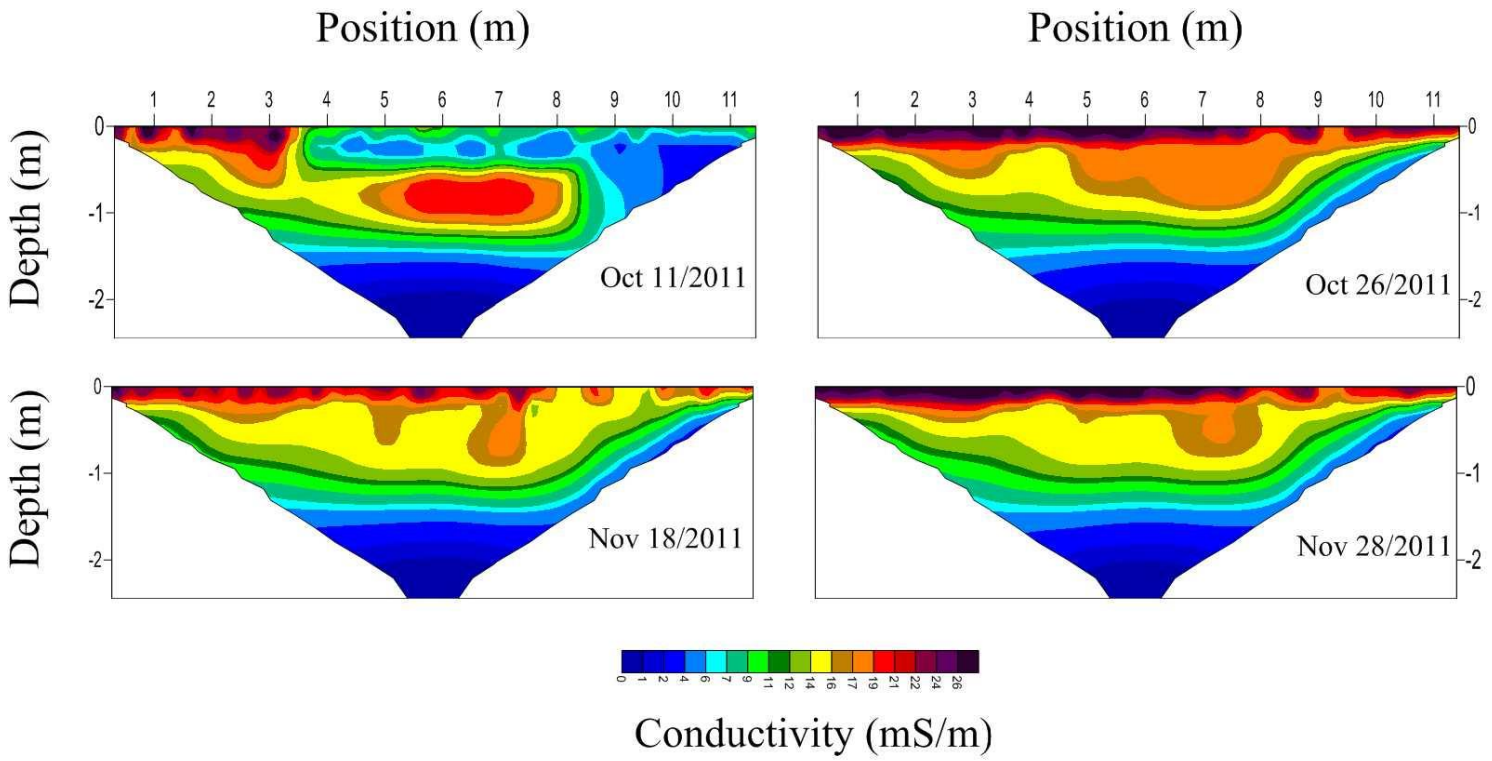

Figure C-3b: High resolution ERT results for the 85 m station plotted with respect to conductivity on a linear scale.

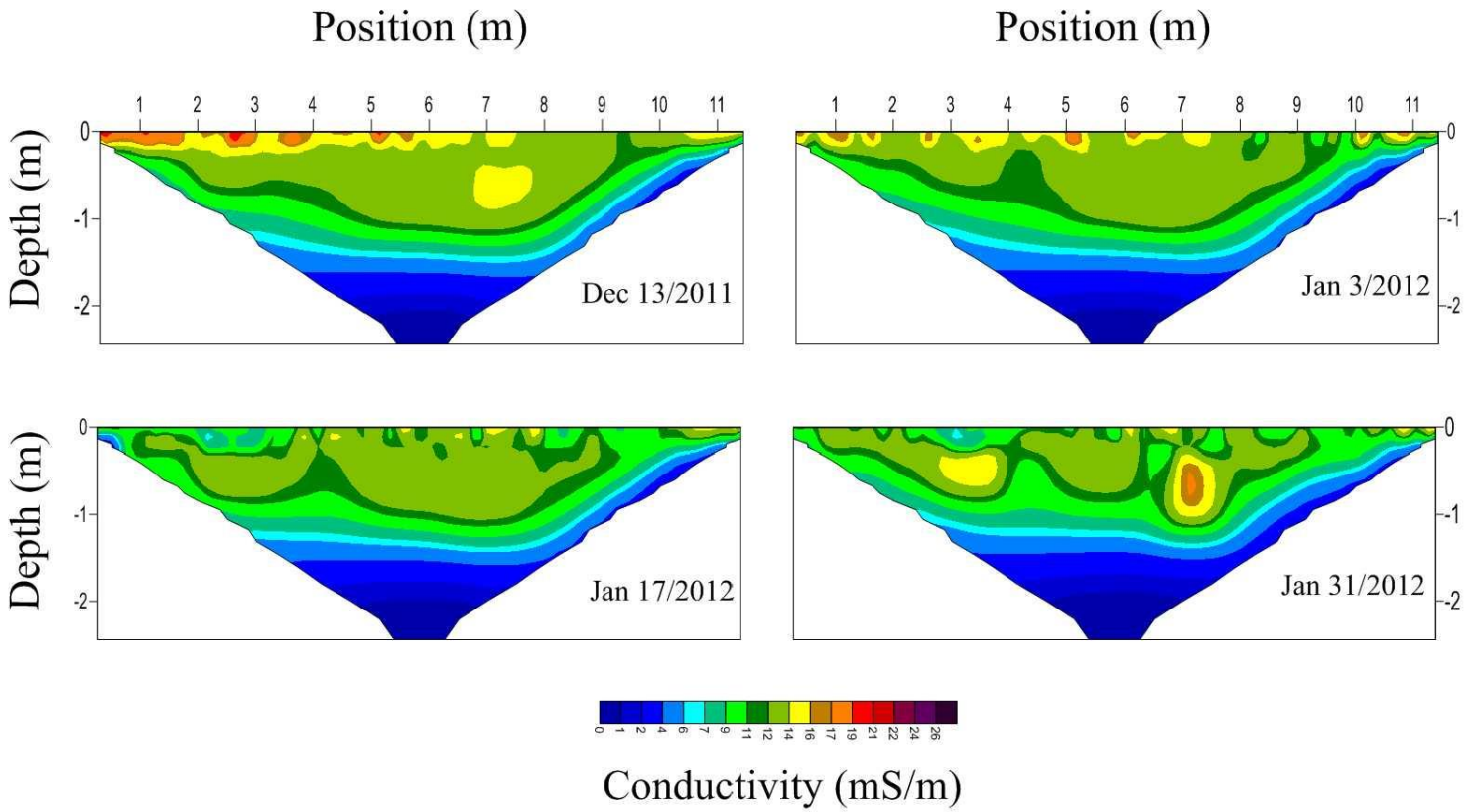

Figure C-3c: High resolution ERT results for the 85 m station plotted with respect to conductivity on a linear scale.

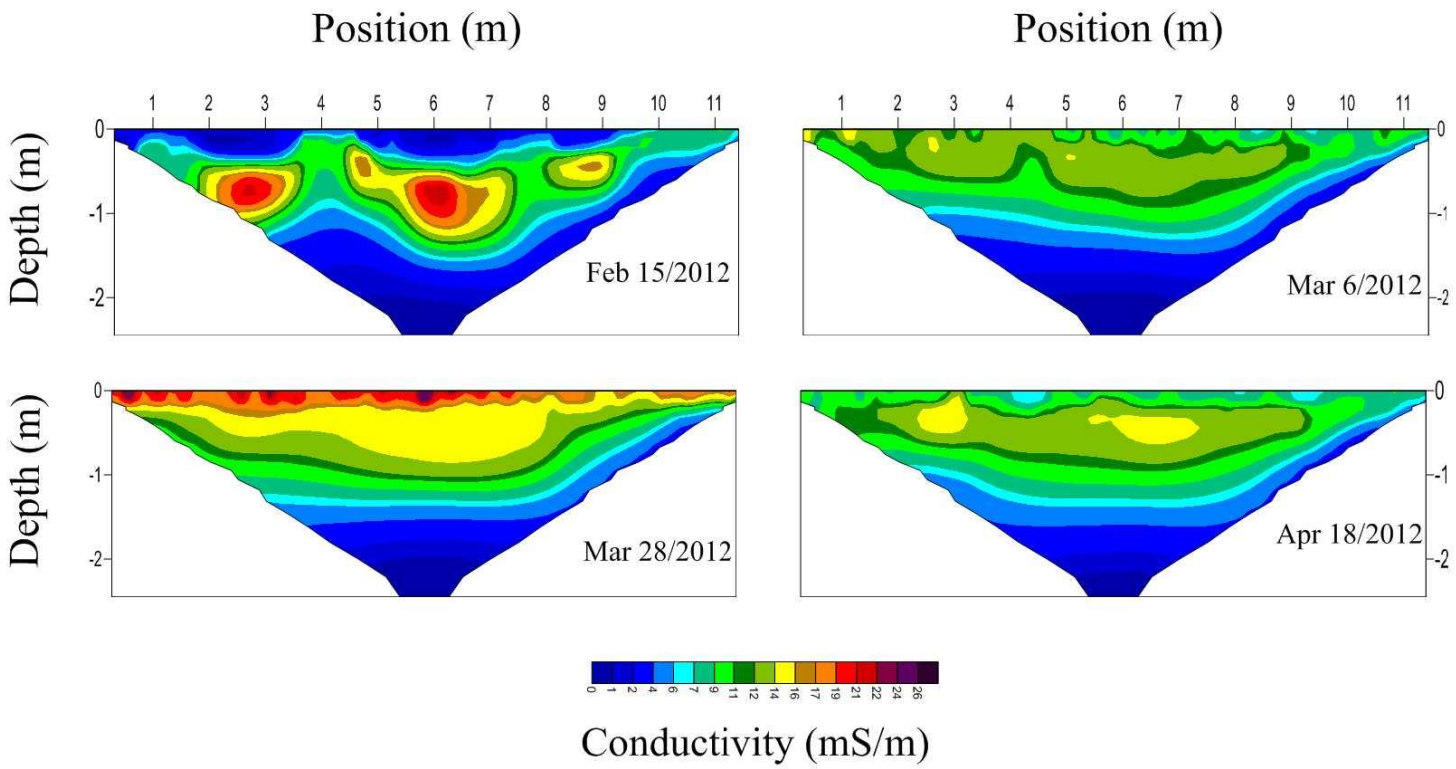

Figure C-3d: High resolution ERT results for the 85 m station plotted with respect to conductivity on a linear scale.

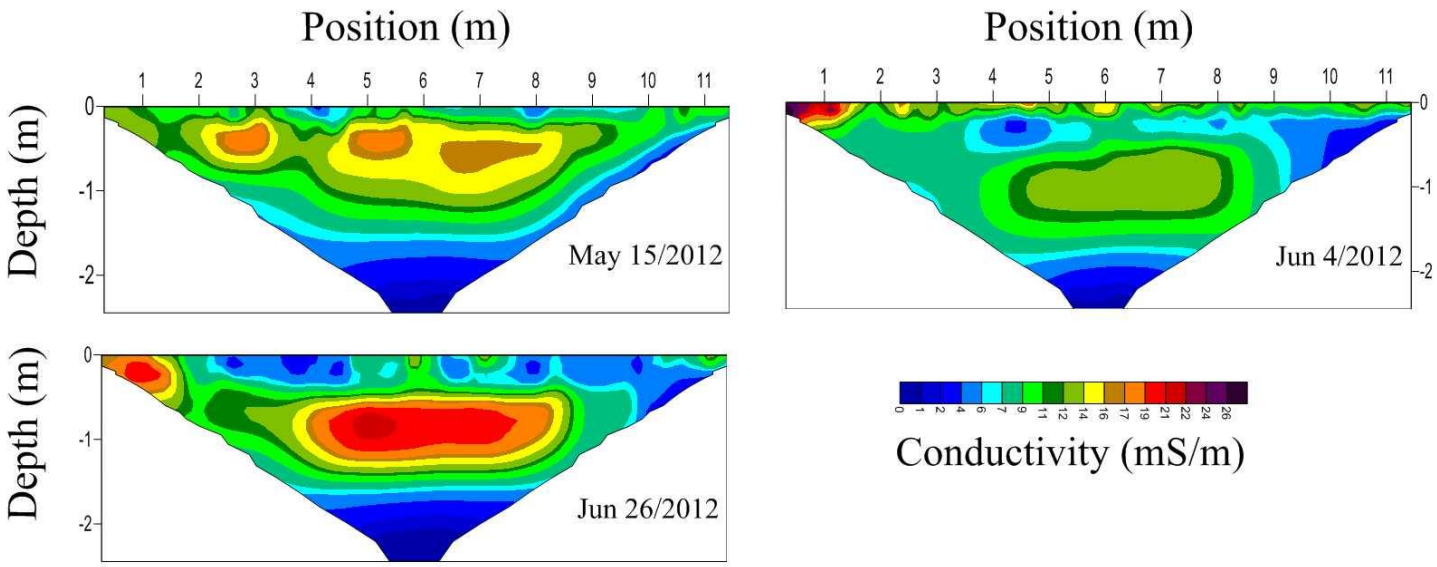

Figure C-3e: High resolution ERT results for the 85 m station plotted with respect to conductivity on a linear scale.

Appendix D

Attached CD (Available upon request)